The Dissertation Committee for Erik John Brugamyer
certifies that this is the approved version of the following dissertation:

Chemical Abundances of Giant-Planet-Host Stars

Committee:

Christopher Sneden, Co-Supervisor

Sarah E. Dodson-Robinson, Co-Supervisor

William D. Cochran

Edward L. Robinson

Jason T. Wright

Chemical Abundances of Giant-Planet-Host Stars

by

Erik John Brugamyer, B.S.Phy.; B.A.; M.P.A.; M.A.

DISSERTATION
Presented to the Faculty of the Graduate School of
The University of Texas at Austin
in Partial Fulfillment
of the Requirements
for the Degree of

DOCTOR OF PHILOSOPHY

THE UNIVERSITY OF TEXAS AT AUSTIN
December 2014

Dedicated to Kim and Lauren

Acknowledgments

I would like to thank my committee, especially Sally Dodson-Robinson, Bill Cochran, and Chris Sneden. I have always considered myself as having three (wonderful) supervisors and mentors. Sally, Chris and Bill have been much more than mere supervisors. They've listened to accounts of my personal problems, invited me into their homes, and otherwise served as excellent mentors and role models. Thank you!

Sally's patience, insight, suggestions and financial support have all been most welcome. She helped take a rough idea and shape it into a focused project.

Bill trained me on the 2.7m telescope and the data reduction process. I have always found his door open for many questions and tips on handling high resolution stellar spectroscopic data.

Chris has been my long-time unofficial mentor. I have used Chris' MOOG software for the spectroscopic analysis – an invaluable tool without which the present research would not have been possible. More importantly, Chris has long served as a role model and caring mentor.

Chemical Abundances of Giant-Planet-Host Stars

Erik John Brugamyer, Ph.D.
The University of Texas at Austin, 2014

Supervisors: Christopher Sneden
Sarah E. Dodson-Robinson

The positive correlation between planet detection rate and host star iron abundance lends strong support to the core accretion theory of planet formation. However, iron is not the most significant mass contributor to the cores of giant planets. Since giant planet cores are thought to grow from silicate grains with icy mantles, the likelihood of gas giant formation should depend heavily on the oxygen and silicon abundance of the planet formation environment. Here we compare the silicon and oxygen abundances of a set of 76 planet hosts and a control sample of 80 metal-rich stars without any known giant planets. Our new, independent analysis was conducted using high resolution, high signal-to-noise data obtained at McDonald Observatory. Because we do not wish to simply reproduce the known planet-metallicity correlation, we have devised a statistical method for matching the underlying [Fe/H] distributions of our two sets of stars. We find a 99%

probability that planet detection rate depends on the silicon abundance of the host star, over and above the observed planet-metallicity correlation. We do not detect any such correlation for oxygen. Our results would thus seem to suggest that grain nucleation, rather than subsequent icy mantle growth, is the important limiting factor in forming giant planets via core accretion. Based on our results and interpretation, we predict that planet detection should correlate with host star abundance for refractory elements responsible for grain nucleation and that no such trends should exist for the most abundant volatile elements responsible for icy mantle growth.

Table of Contents

List of Tables

List of Figures

Chapter 1

Introduction

The last 20 years have been something of a golden age in the field of extrasolar planets. In that time, the list of known planets outside our own solar system has grown from zero into the thousands. We've gone from supposition about the presence of planets to statistical measures of their frequency. We've gone from theoretical speculation about their composition to direct detections of their atmospheres. We now even have a handful of direct images of extrasolar planets. It's been an exciting time to be a graduate student studying these systems!

1.1 The Questions

Due to observational bias, the first several hundred of these discovered planets were overwhelmingly very massive planets in orbits very close to their stars – planetary systems nothing like our own. Thanks in large part to the *Kepler* space telescope, we now know of a virtual managerie of system types. Most importantly, we now have our first, tentative answers to two important questions: "how common are solar system analogs"; and "how common are Earth-like planets". It would seem that the answer to the second question is: “very!”. An answer to the first question, however, remains a bit elusive at this point.

A more basic question also remains to be fully answered: “how do planets form”. It is surprising to me that we still don’t know the answer with certainty. This Earth that we walk on certainly did form, but the exact steps leading to its formation remain clouded in a bit of mystery. The two leading theories of planet formation – core collapse and core accretion – offer but broad brushstrokes outlining the process. Many details remain to be explored and/or explained.

The primary aim of this work is to explore one of these details. Namely, of the elements comprising a typyical planetary core, are there certain ones that play an outsize role in the process of core accretion? A secondary aim of this work is to contribute a small part to the answer to the uniqueness question: how common are planetary systems like our own?

1.2 The Planet-Metallicity Correlation and Core Accretion

Gonzalez (1997, 1998, 1999) was the first to analyze the metallicities of stars with planets, and to conclude that these stars tend to be more metal-rich when compared to those without planets. Numerous subsequent studies have supported this conclusion (e.g. Reid 2002, Heiter & Luck 2003, Santos et al. 2005, Fischer & Valenti 2005, Grether & Lineweaver 2007, Neves et al. 2009)(among others). The Fischer & Valenti study was notable for its large sample of 1040 stars from the Keck, Lick and Anglo-Australian Telescope planet search surveys, and for its uniform analysis. Their study included 105 planetary systems and a carefully selected control sample. They found a clear trend of planet detection with overall stellar metallicity. Over 25% of the most metal-rich stars ($\backsim$3 times solar metallicity) in their sample were found to harbor planets, with a marked decrease for more metal-poor stars – less than 5% for solar-metallicity and below.

The first attempts at explaining the planet-metallicity correlation focused on the possibility of self-pollution via planetesimal accretion. Gonzalez (1997) suggested that planet-host stars only appear more metal-rich because their atmospheres are preferentially enhanced through accretion of heavy material during the planet formation stage. If this hypothesis is correct, we would expect the most metal-rich planet-hosts to have the most shallow convection zones. Fischer & Valenti (2005) argued, however, that there is no relation between convection zone depth and metallicity for stars in their sample, and subsequent studies have provided additional evidence of this. The self-pollution scenario also leads to the expectation that planet-hosts would exhibit decrements in volatile elements, since these would not be abundant in the accreting planetesimals. Takeda & Honda (2005) found no such difference, arguing that the [C/Fe], [N/Fe] and [O/Fe] distributions of planet-host stars were "practically indistinguishable" from non-host stars of similar metallicities.

Another possible explanation for the planet-metallicity correlation is that planet-host stars form in chemically-peculiar environments with abundance ratios that differ from typical Galactic chemical evolution models. Numerous studies have found little to no differences in the overall trends of [X/Fe] between stars with and without known planets. Based on these results, stars with planets appear to simply lie on the high-metallicity end of otherwise “normal” stellar distributions.

It would seem, then, that the tendency for planets to orbit relatively metal-rich stars is best explained through the core accretion model of planet formation, whereby planets grow through accretion of solid, metal-rich material to form massive cores. Iron (the typically-used proxy for overall stellar metallicity) is certainly an important component, but there are other significant contributors, especially oxygen, carbon, silicon, magnesium, sulfur, nitrogen and aluminum.

Exploring any trends with these elements in precise detail – and doing so using true, robust differential measurements (with respect to the Sun) – requires line-by-line individual abundance determinations using uniform, high-resolution and high signal-to-noise data. And this is best accomplished using traditional, tried-and-true equivalent width (EW) curve of growth (COG) analysis methods, such as that employed by the popular line analysis program MOOG (Sneden 1973). Unfortunately, comprehensive analysis of the planetary community’s ever-growing stellar data-sets is not practical using the traditional, widely available (manual) EW measurement and COG analysis tools. Recognizing this, much of the community has turned to automated spectral synthesis and/or spectral matching techniques. Such approaches present their own unique problems, however, some of which could have serious consequences when attempting to determine precise stellar parameters and relative abundances. The primary goal of the present project was development of an integrated, flexible, convenient tool for the (semi-)automated spectroscopic analysis of high-quality data-sets using established, well-researched COG methods, as a possible alternative to the increasing number of spectral synthesis and spectral matching tools.

1.3 Outline

Chapter 2 of this work presents published research in which we focused first on silicon and oxygen abundances in planet-hosting stars. We chose these two elements as a starting point because they represent the most abundant refractory and volatile elements, respectively, thought to play in important role in the formation of planet cores.

Chapter 3 of this work presents soon-to-be-published research in which we announce the discovery of two new long-period giant planets orbiting main-sequence stars, via the radial velocity technique. We also discuss two cases of radial velocity signatures indicative of planet presence, but that appear to be related instead to stellar activity.

Chapter 4 of this work discusses our developed and tested pipeline for the semi-automated determination of fundamental stellar parameters and selected elemental abundances.

Chapter 5 of this work offers a conclusion and outlook for the future.

The appendix lists the titles, author lists, and abstracts of 14 published papers to which I contributed in meaningful ways, and on which I'm listed as a contributing author. The majority of these were projects related to the Kepler space mission. Kepler has helped show us that (1) small, rocky planets are everywhere; (2) circumbinary planets are not all that rare; and (3) that small, rocky planets are found around stars with a wide range of metallicities, unlike hot Jupiters which are found preferentially around metal-rich stars.

Chapter 2

Silicon and Oxygen Abundances in Planet-Host Stars[1]

2.1 Introduction

The tendency for planets to orbit metal-rich stars lends strong support to the core accretion model of planet formation, whereby planets grow through accretion of solid, metal-rich material to form massive cores. Within the context of core accretion (cf. Safronov 1969; Pollack et al. 1996), heavy element abundances are important to the extent that they contribute to the inventory of solid material available for planetesimal formation. Iron (the typically-used proxy for overall stellar metallicity) is certainly an important component, but there are other significant contributors, especially oxygen, carbon, silicon, magnesium, sulfur, nitrogen and aluminum.

Oxygen is thought to be the single most important contributor to the mass of giant planets, primarily via water ice accreted beyond the snow line of the disk (Hayashi 1981, Weidenshilling 1977) and, to a lesser extent, through the oxides of Si, Mg, Ca, and Al. Carbon, via heavy organic

---

[1] This chapter has been published as Brugamyer, E., Dodson-Robinson, S.E., Cochran, W.D., and Sneden, C. 2011, ApJ, 738, 97.

compounds, is probably the second most important mass contributor (Lodders 2004), followed by silicon. These elements often demonstrate different abundance patterns relative to iron. Robinson et al. (2006) reported relative silicon and nickel enrichment in planet hosts and Fuhrmann & Bernkopf (2008) have reported enhancements in alpha-capture elements. Thus, iron is likely not an ideal proxy for measuring the abundances of material used to build planet cores.

Previous tests of how individual elements contribute to planet formation have focused on the possibility that planet hosts are chemically peculiar stars with abundance ratios that differ from typical Population I stars. If planet hosts are chemically peculiar, the slopes of [X/Fe] vs. [Fe/H] among them should be distinct from what Galactic chemical enrichment models (e.g. Timmes et al. 1995) predict. Bodaghee et al. (2003) found no such differences in their sample for alpha- and iron-peak elements. They observe no difference in the overall trends of [X/Fe] between planet hosts and their volume-limited sample of stars without any known planetary-mass companions. Based on their results, stars with planets appear to be indistinguishable from other field stars, and seem to simply lie on the high-metallicity end of otherwise "normal" stellar distributions.

Given the metal-rich nature of planet-hosting stars, a pressing need when further exploring the planet-formation importance of individual elements is to carefully match the underlying iron distributions of planet-host and control samples. Previous planet-host studies (e.g. Fischer & Valenti

2005, Neves et al. 2009) have found that, in addition to iron, the abundances of various other metals are enhanced in these stars compared to stars with no known planets. This comes as no surprise, however, given the known positive correlation between host star iron abundance and planet detection rate. Since planet-hosts are found to have higher overall iron content (which serves as a proxy for overall metallicity) compared to non-hosts, they are indeed expected to have a higher content of other metals as well. An ideal study would consist of an arbitrarily large number of hosts and non-hosts, such that the samples could be divided into arbitrarily small [Fe/H] bins and still have a statistically significant number of hosts and control stars in each bin. It would then be trivial to determine if, *at a given [Fe/H]*, a difference existed between the two groups of stars in the average abundances of elements important for planet formation. In the absence of such an ideal sample, we have devised a statistical method for matching the underlying iron distributions.

The present analysis is aimed at examining the most abundant heavy elements important for planet formation. We have chosen to focus first on silicon and oxygen. Our hypothesis is that if core-accretion is responsible for the majority of known giant planets, then for a given [Fe/H] their stellar hosts should show enhancements in silicon and oxygen relative to iron. We therefore wish to determine whether there is a statistically significant difference in the silicon and oxygen abundance distributions of stars with planets, compared to those without any known giant planets.

2.2 Observations and Data Reduction

For this study, we selected 76 FGK dwarf and sub-giant host stars and 80 non-host stars for comparison. The data were obtained between July 1998 and March 2010 on the 2.7-meter Harlan J. Smith telescope and the Hobby-Eberly telescope ("HET") at McDonald Observatory. Our program stars span the following ranges: $-0.67 \leq [Fe/H] \leq +0.54$; $4935 \leq T_{\mathrm{eff}} \leq 6250$ (K); $3.15 \leq \log g \leq 4.63$; and $0.54 \leq v_{\mathrm{mic}} \leq 1.53$ (km s^{-1}), where v_{mic} represents the microturbulent velocity.

2.2.1 Non-host stars

All non-host stars were selected from the ∽300 stars being monitored as part of the McDonald Observatory Planetary Search program (hereafter "MOPS"; see Wittenmyer et al. 2006 for a description of the program and detection limits) on the 2.7m telescope. For these, we used template spectra taken without the iodine cell in the optical path. Using the current instrumental configuration ("Phase III"; begun in 1998), the program achieves routine internal precision of 6–9 m s^{-1}. With a monitoring baseline of over 10 years, we can thus exclude roughly Jupiter-mass companions out to 5 AU, or roughly Neptune-mass companions out to 1 AU, around these stars.

Since planet-hosting stars tend to have higher overall metallicity, we built our non-host sample by choosing the most metal-rich stars available from the MOPS program. This was done by cross-referencing the MOPS list with available metallicity references from the SIMBAD Astronomical

Database[2] and the NASA/IPAC/NExScI Star and Exoplanet Database ("NStED")[3] and choosing non-host stars in such a manner that the final overall metallicity distributions of our host and non-host samples were as similar as possible. Note that we attempt to statistically control for imperfect matching of the [Fe/H] distributions later in our analysis.

2.2.2 Host stars

Our host stars were selected in a statistically haphazard manner, as follows. Data for twenty-six of our planet-host stars came from the MOPS program (as in the case of the non-host stars), by selecting only those MOPS host stars with data having a signal-to-noise ratio ≥ 100. The remaining 50 hosts were observed independently, using both the 2.7m telescope (in the same instrumental setup as the MOPS program) and the HET. For these, we selected the brightest objects with confirmed planetary companions in the literature that were available for observation from McDonald Observatory during our supplemental observing runs from December 2009 to March 2010. Fifty-six of our host stars were ultimately observed with the 2.7m telescope, and 20 with the HET.

---

[2] http://simbad.u-strasbg.fr/simbad/

[3] http://nsted.ipac.caltech.edu/

2.2.3 Instruments

For the 2.7m telescope, we utilized the Tull Coudé Spectrometer (Tull et al. 1994). This cross-dispersed echelle spectrograph uses a 2048x2048 Tektronix CCD with 24 μm pixels and our configuration uses the "E2" grating with 52.67 groove mm^{-1}. With a 1.2 arcsec slit, we achieve a resolving power (=$\lambda/\Delta\lambda$) of R=60,000 in this configuration. The wavelength coverage extends from 3750 Å to 10,200 Å. Coverage is complete from the blue end to 5691 Å, with increasingly large inter-order gaps thereafter.

For the HET, we utilized the fiber-fed High Resolution Spectrograph (Tull 1998). The spectrograph uses a mosaic of two 2048x4102 Marconi Applied Technologies (now E2V Technologies) CCDs with 15 μm pixels and a grating with 316 groove mm^{-1}. Using a 2.0 arcsec fiber, we achieve a resolving power of R=60,000 with this instrument. The wavelength coverage extends from 4090 Å to 7875 Å. Coverage is complete except for the range 5930 Å to 6012 Å, corresponding to the gap between the two CCDs. The signal-to-noise ratio of our 2.7m and HET data range from $\backsim$100-500.

2.2.4 Data reduction

The data were reduced using standard routines within the *echelle* and *onedspec* packages of the Image Reduction and Analysis Facility (IRAF). The process included overscan trimming, bias frame subtraction, removal of scattered light, flat field division, extraction of the orders and wavelength calibration using a Th-Ar calibration lamp spectrum. We then manually removed any cosmic rays that IRAF's interpolation routines were unable to handle. The final steps involved dividing out the blaze function, normalizing the continuum and combining orders.

2.3 Measuring Abundances

The results of our stellar parameter and abundance determinations are listed in Table 2.1 (for planet-host stars) and Table 2.2 (for non-host stars).

Table 2.1. Summary of Results for Planet-Host Stars

Star Name	[Fe/H]	[Si/Fe]	[O/Fe] (LTE)[a]	[O/Fe] (NLTE)[a]	$T_{\rm eff}$ (K)	log g	$v_{\rm mic}$ (km s^{-1})
109 Psc	0.19	-0.04	-0.08	-0.10	5675	4.12	1.16
14 Her	0.51	0.03	-0.28	-0.19	5355	4.47	1.07
16 Cyg B	0.06	0.01	0.05	0.03	5705	4.36	1.13
47 UMa	0.05	0.01	0.01	-0.02	5880	4.40	1.16
51 Peg	0.25	0.02	-0.04	-0.03	5800	4.50	1.03
55 Cnc	0.38	0.10	-0.10	-0.04	5250	4.49	1.11
6 Lyn	-0.04	0.02	0.15	0.07	4990	3.34	1.26
61 Vir	0.03	0.00	0.08	0.08	5550	4.42	1.00
70 Vir	-0.01	-0.02	0.03	0.01	5549	4.14	1.18
eps Eri	-0.02	-0.04	0.14	0.19	5110	4.54	1.11
HD 100777	0.33	0.07	-0.09	-0.05	5585	4.44	0.98
HD 102195	0.11	0.01	0.05	0.10	5270	4.56	1.13
HD 106252	-0.05	-0.01	0.11	0.06	5870	4.41	1.07
HD 107148	0.33	0.07	-0.04	-0.02	5810	4.56	1.08
HD 114762	-0.67	0.16	0.43	0.33	5960	4.54	1.17
HD 118203	0.15	0.09	0.26	0.14	5690	3.87	1.15

Table 2.1 (cont'd)

Star Name	[Fe/H]	[Si/Fe]	[O/Fe] (LTE)[a]	[O/Fe] (NLTE)[a]	T_{eff} (K)	log g	v_{mic} (km s^{-1})
HD 11964	0.14	-0.02	-0.06	-0.07	5345	4.02	1.18
HD 12661	0.39	0.04	-0.07	-0.04	5720	4.42	1.22
HD 130322	0.09	-0.03	-0.09	-0.05	5410	4.48	1.12
HD 132406	0.16	0.00	-0.04	-0.03	5820	4.48	1.01
HD 136118	-0.02	-0.04	0.27	0.10	6095	4.07	1.12
HD 136418	-0.04	0.05	0.01	-0.02	4985	3.50	1.03
HD 13931	0.10	-0.04	0.07	0.02	5850	4.26	1.14
HD 1461	0.23	0.01	-0.07	-0.05	5745	4.51	1.19
HD 149026	0.31	0.04	0.08	0.02	6140	4.35	1.23
HD 149143	0.25	0.07	0.15	0.07	5825	4.05	1.15
HD 154345	-0.08	0.02	0.06	0.09	5430	4.54	0.75
HD 155358	-0.61	0.10	0.55	0.41	5860	4.24	0.75
HD 16175	0.36	0.05	0.18	0.14	6020	4.39	1.28
HD 164922	0.21	0.09	-0.03	0.02	5395	4.57	0.90
HD 168443	0.12	0.01	0.18	0.15	5580	4.22	1.17
HD 178911 B	0.14	-0.01	0.29	0.17	5730	3.97	1.18

Table 2.1 (cont'd)

Star Name	[Fe/H]	[Si/Fe]	[O/Fe] (LTE)[a]	[O/Fe] (NLTE)[a]	T_{eff} (K)	log g	v_{mic} (km s^{-1})
HD 185269	0.13	0.04	0.19	0.07	5990	4.03	1.26
HD 189733	0.01	0.07	0.13	0.18	5020	4.55	0.82
HD 190228	-0.20	-0.02	0.03	0.00	5310	3.91	1.22
HD 195019	0.07	-0.04	0.10	0.05	5790	4.24	1.26
HD 19994	0.19	-0.01	0.22	0.08	6095	4.05	1.32
HD 202206	0.36	-0.04	-0.22	-0.18	5770	4.50	1.15
HD 20367	0.14	-0.08	0.11	0.06	6120	4.51	1.18
HD 20782	0.01	-0.07	0.07	0.05	5770	4.45	1.12
HD 209458	0.01	0.03	0.18	0.09	6090	4.40	1.17
HD 210277	0.28	0.04	0.01	0.04	5565	4.51	1.04
HD 217107	0.45	-0.03	-0.20	-0.14	5690	4.55	1.13
HD 219828	0.25	-0.01	0.03	-0.01	5895	4.25	1.18
HD 30562	0.24	0.00	0.10	0.03	5860	4.13	1.25
HD 33283	0.36	0.02	0.14	0.06	5995	4.16	1.39
HD 34445	0.20	-0.05	0.12	0.07	5830	4.24	1.13
HD 3651	0.17	0.06	0.04	0.08	5185	4.38	1.10

Table 2.1 (cont'd)

Star Name	[Fe/H]	[Si/Fe]	[O/Fe] (LTE)[a]	[O/Fe] (NLTE)[a]	$T_{\rm eff}$ (K)	log g	$v_{\rm mic}$ (km s^{-1})
HD 37124	-0.41	0.20	0.49	0.47	5505	4.57	0.87
HD 38529	0.40	-0.03	-0.03	-0.07	5600	3.90	1.40
HD 40979	0.23	-0.02	0.10	0.04	6160	4.42	1.10
HD 43691	0.31	0.03	0.09	0.02	6225	4.33	1.19
HD 44219	0.04	0.01	0.16	0.10	5710	4.21	1.31
HD 45350	0.33	0.01	-0.04	-0.02	5605	4.35	1.15
HD 45652	0.33	0.07	-0.07	-0.01	5340	4.52	0.83
HD 46375	0.30	0.08	-0.01	0.05	5250	4.51	1.04
HD 49674	0.34	0.07	-0.05	0.00	5630	4.61	0.93
HD 50554	-0.04	0.01	0.27	0.18	5915	4.33	1.12
HD 52265	0.21	0.02	0.23	0.15	6105	4.38	1.34
HD 60532	-0.06	-0.01	0.43	0.17	6220	3.88	1.18
HD 66428	0.34	0.07	-0.03	0.01	5765	4.62	1.11
HD 6718	0.03	-0.04	-0.01	0.00	5745	4.53	0.98
HD 68988	0.36	0.07	0.01	0.02	5960	4.56	1.10
HD 72659	0.01	-0.03	0.16	0.06	5870	4.16	1.23

Table 2.1 (cont'd)

Star Name	[Fe/H]	[Si/Fe]	[O/Fe] (LTE)[a]	[O/Fe] (NLTE)[a]	$T_{\rm eff}$ (K)	$\log\ g$	$v_{\rm mic}$ (km s^{-1})
HD 73534	0.23	0.08	-0.01	0.00	4965	3.71	1.08
HD 75898	0.20	0.05	0.23	0.11	5880	4.01	1.24
HD 81040	-0.06	-0.01	0.07	0.08	5730	4.60	0.80
HD 82943	0.30	-0.02	0.03	0.02	5975	4.47	1.20
HD 8574	-0.04	0.00	0.21	0.09	6010	4.22	1.35
HD 88133	0.41	0.04	-0.11	-0.09	5475	4.16	1.12
HD 89307	-0.14	0.02	0.24	0.18	5915	4.47	1.21
HD 92788	0.37	0.02	-0.07	-0.02	5800	4.61	1.06
HD 9446	0.14	-0.02	0.07	0.07	5770	4.55	1.20
HD 96167	0.36	0.07	0.06	0.02	5775	4.14	1.22
HIP 14810	0.27	0.10	0.05	0.06	5510	4.30	1.08
rho CrB	-0.18	0.03	0.23	0.17	5825	4.37	1.02

[a] For the "NLTE" [O/Fe] values we incorporated the non-LTE corrections of Ramírez, Allende Prieto & Lambert (2007). The "LTE" values are our original abundance determinations, ignoring any possible non-LTE effects (see section 3.3).

Table 2.2. Summary of Results for Non-Host Stars

Star Name	[Fe/H]	[Si/Fe]	[O/Fe] (LTE)[a]	[O/Fe] (NLTE)[a]	T_{eff} (K)	log g	v_{mic} (km s^{-1})
10 CVn	-0.43	-0.01	0.18	0.14	5900	4.57	0.85
11 Aqr	0.27	0.01	0.05	0.02	5905	4.30	1.21
13 Ori	-0.16	0.05	0.26	0.18	5740	4.25	1.20
13 Tri	-0.10	-0.03	0.11	0.01	5950	4.18	1.17
18 Cet	-0.18	-0.03	0.14	0.07	5840	4.17	1.30
31 Aql	0.46	0.02	-0.05	-0.02	5635	4.34	1.21
36 UMa	-0.02	-0.09	0.06	-0.01	6150	4.42	1.00
58 Eri	0.04	-0.02	0.02	0.02	5830	4.58	1.10
83 Leo A	0.38	0.04	-0.20	-0.13	5472	4.50	1.06
88 Leo A	0.03	-0.03	0.06	0.02	6000	4.50	1.12
alp For	-0.14	-0.04	0.17	0.02	6250	4.17	1.20
beta Com	0.10	-0.04	-0.02	-0.04	6060	4.56	1.06
gam Lep B	0.11	-0.06	-0.19	-0.11	4990	4.61	1.20
gam2 Del	0.31	-0.11	-0.26	-0.27	4935	3.15	1.53
HD 10086	0.13	-0.04	-0.01	0.01	5670	4.52	1.18
HD 105844	0.33	-0.03	-0.19	-0.14	5590	4.48	0.98

Table 2.2 (cont'd)

Star Name	[Fe/H]	[Si/Fe]	[O/Fe] (LTE)[a]	[O/Fe] (NLTE)[a]	T_{eff} (K)	log g	v_{mic} (km s^{-1})
HD 107146	0.00	-0.06	0.10	0.08	5870	4.56	1.18
HD 108942	0.28	-0.02	0.02	0.00	5770	4.23	1.28
HD 110010	0.38	0.00	0.10	0.10	6010	4.52	1.28
HD 11007	-0.17	0.00	0.14	0.04	6015	4.24	1.27
HD 110537	0.12	-0.02	0.05	0.04	5690	4.35	1.30
HD 111431	0.09	0.00	0.20	0.10	5880	4.13	1.27
HD 115043	0.01	-0.05	0.03	0.01	5840	4.47	0.99
HD 116956	0.11	0.01	0.04	0.07	5325	4.41	1.21
HD 129357	0.02	-0.02	0.10	0.06	5750	4.32	1.17
HD 13825	0.22	0.02	-0.01	-0.01	5660	4.35	1.26
HD 138776	0.44	-0.02	-0.13	-0.12	5700	4.25	1.18
HD 149028	0.21	0.00	-0.05	-0.05	5520	4.22	1.23
HD 184385	0.13	0.01	-0.02	0.02	5565	4.61	1.24
HD 184499	-0.40	0.13	0.48	0.40	5830	4.50	0.96
HD 185414	-0.10	-0.01	0.06	0.04	5820	4.55	1.23
HD 187748	0.08	-0.04	0.13	0.08	5980	4.44	1.18

Table 2.2 (cont'd)

Star Name	[Fe/H]	[Si/Fe]	[O/Fe] (LTE)[a]	[O/Fe] (NLTE)[a]	T_{eff} (K)	log g	v_{mic} (km s^{-1})
HD 190613	0.04	-0.01	0.15	0.10	5720	4.22	0.91
HD 19256	0.25	-0.01	0.11	0.04	5910	4.14	1.33
HD 200078	0.25	0.03	0.24	0.19	5630	4.14	1.28
HD 221146	0.12	0.04	0.11	0.05	5880	4.30	1.24
HD 299	0.20	-0.05	0.07	0.02	6000	4.35	1.22
HD 31609	0.26	-0.06	-0.08	-0.03	5560	4.50	1.08
HD 39480	0.19	0.00	0.20	0.11	5750	4.00	1.24
HD 47127	0.14	0.02	0.08	0.08	5615	4.43	1.15
HD 56124	0.00	-0.02	0.07	0.04	5750	4.35	1.12
HD 59062	0.38	0.03	-0.06	-0.03	5575	4.37	1.04
HD 60521	0.13	0.00	0.18	0.12	5805	4.22	1.25
HD 73350	0.13	-0.01	0.01	0.01	5815	4.57	1.23
HD 75880	0.16	0.04	0.08	0.06	5595	4.25	1.23
HD 8038	0.17	-0.01	0.19	0.17	5590	4.32	1.18
HD 87000	0.14	0.01	-0.06	0.00	5170	4.49	1.16
HD 92719	-0.04	-0.07	0.04	0.02	5760	4.42	0.94

Table 2.2 (cont'd)

Star Name	[Fe/H]	[Si/Fe]	[O/Fe] (LTE)[a]	[O/Fe] (NLTE)[a]	T_{eff} (K)	log g	v_{mic} (km s^{-1})
HD 94126	0.40	0.07	-0.12	-0.09	5570	4.30	0.97
HD 94482	-0.02	-0.05	0.15	0.04	5995	4.15	1.33
HD 95653	0.54	-0.04	-0.26	-0.20	5585	4.35	0.93
HD 97037	-0.05	-0.03	0.12	0.07	5830	4.32	1.18
HD 97854	0.20	-0.03	0.10	0.00	5985	4.06	1.38
HD 99505	-0.11	-0.07	0.09	0.08	5700	4.48	0.93
HR 173	-0.56	0.20	0.49	0.42	5360	4.09	1.01
HR 1980	0.06	-0.04	0.03	-0.01	6085	4.53	1.17
HR 2208	-0.01	-0.05	-0.02	0.00	5700	4.55	1.24
HR 2225	0.02	-0.04	-0.05	-0.03	5590	4.52	1.17
HR 2721	-0.30	0.01	0.25	0.18	5860	4.40	1.04
HR 2997	-0.06	-0.03	-0.02	0.01	5470	4.52	1.10
HR 3538	0.13	0.01	0.01	0.02	5775	4.57	1.08
HR 3862	-0.02	-0.04	0.16	0.06	6180	4.41	1.18
HR 3881	0.14	-0.01	0.15	0.07	5915	4.20	1.24
HR 4051	0.05	-0.04	0.13	0.03	6040	4.29	1.26

Table 2.2 (cont'd)

Star Name	[Fe/H]	[Si/Fe]	[O/Fe] (LTE)[a]	[O/Fe] (NLTE)[a]	$T_{\rm eff}$ (K)	log g	$v_{\rm mic}$ (km s^{-1})
HR 448	0.18	-0.01	0.08	0.01	5840	4.07	1.50
HR 4525	-0.18	-0.01	0.09	0.11	5600	4.59	0.98
HR 4767	-0.05	-0.03	0.10	0.05	6010	4.52	1.04
HR 4864	0.14	-0.03	-0.08	-0.04	5630	4.57	1.15
HR 5183	0.07	0.00	0.15	0.07	5810	4.15	1.32
HR 6669	0.08	-0.06	0.08	-0.03	6140	4.24	1.12
HR 7569	-0.13	0.07	0.32	0.25	5720	4.31	1.18
HR 8964	0.14	-0.05	-0.05	-0.04	5840	4.57	1.27
iota Psc	-0.05	-0.02	0.19	0.05	6240	4.24	1.16
kap1 Cet	0.07	-0.01	0.00	0.01	5705	4.51	1.11
lam Aur	0.13	-0.02	0.06	0.02	5899	4.34	1.10
lam Ser	0.03	-0.01	0.06	0.00	5920	4.25	1.22
mu Her	0.34	-0.05	-0.07	-0.08	5600	4.06	1.35
pi1 UMa	-0.03	-0.03	0.09	0.06	5820	4.49	1.14
tau Cet	-0.44	0.11	0.27	0.29	5345	4.54	0.54
xi Boo A	-0.09	-0.03	-0.01	0.03	5530	4.63	1.20

Table 2.2 (cont'd)

Star Name	[Fe/H]	[Si/Fe]	[O/Fe] (LTE)[a]	[O/Fe] (NLTE)[a]	$T_{\rm eff}$ (K)	log g	$v_{\rm mic}$ (km $\rm s^{-1}$)

[a] For the "NLTE" [O/Fe] values we incorporated the non-LTE corrections of Ramírez, Allende Prieto & Lambert (2007). The "LTE" values are our original abundance determinations, ignoring any possible non-LTE effects (see section 3.3).

Our process of determining stellar parameters and abundances involved the following steps:

1. We constructed a list of neutral and singly-ionized iron lines.
2. We obtained a spectrum of the Sun.
3. We measured the equivalent widths of each of our selected iron lines in the solar spectrum.
4. We used these measurements to determine the solar parameters (effective temperature, surface gravity, microturbulent velocity and overall metallicity).
5. With our final solar model atmosphere we then determined the silicon and oxygen abundances using spectral synthesis.
6. Steps 2-5 were repeated for each of our target stars.

The process is explained in further detail in the following subsections.

2.3.1 Atmospheric parameters and iron abundances

All stellar parameters and abundances were determined using MOOG[4] (Sneden 1973) – a local thermodynamic equilibrium (LTE) line analysis and

---

[4] available at http://www.as.utexas.edu/∼chris/moog.html

spectrum synthesis code – and a grid of Kurucz (1993a) ATLAS9 model atmospheres. We constrained the stellar parameters of our targets using a carefully-selected list of 65 isolated, unblended neutral iron lines and 22 singly-ionized iron lines, spanning a wide range in excitation potentials and equivalent widths. The equivalent widths of each of these lines was measured in our program stars using an Interactive Data Language (IDL) routine written exclusively for this purpose (cf. Roederer et al. 2010). The program fits either a gaussian or voigt profile to each line, and allows for manual adjustment of the continuum. The program output is a list of equivalent widths for use with MOOG.

MOOG force-fits abundances to match the measured equivalent widths for each line, using the input atomic line parameters (wavelength, excitation potential and oscillator strength). Our Fe I line parameters, including oscillator strengths (or "log *gf*" values), were taken from the National Institute of Standards and Technology (NIST) Atomic Spectra Database[5], supplemented with values from O'Brian et al. (1991). For the NIST values, we used only those lines with a log *gf* accuracy grade of "D" or better (i.e. we excluded the lowest-quality "E" data from our analysis). See Table 2.3 for the full list of neutral iron lines used in our analysis. Our Fe II parameter values were taken from Meléndez & Barbuy (2009) and are listed in Table 2.4.

---

[5] http://www.nist.gov/physlab/data/asd.cfm

Table 2.3. List of Fe I lines

Wavelength (Angstroms)	Excitation Potential (eV)	Oscillator Strength (log *gf*)	Solar Equivalent Width (mÅ)
4445.47	0.09	-5.38	44.5
4537.67	3.27	-2.88	19.6
4556.93	3.25	-2.69	28.2
4593.54	3.94	-2.06	30.4
4788.75	3.24	-1.76	69.5
4873.75	3.30	-3.06	12.8
5123.72	1.01	-3.06	116.6
5127.68	0.05	-6.12	22.5
5151.91	1.01	-3.32	105.1
5213.81	3.94	-2.76	6.5
5247.05	0.09	-4.98	72.4
5250.21	0.12	-4.90	75.4
5295.30	4.42	-1.69	28.4
5373.70	4.47	-0.87	65.6
5386.34	4.15	-1.77	32.9
5560.21	4.43	-1.19	51.9
5577.03	5.03	-1.55	13.0
5636.70	3.64	-2.61	21.4
5705.47	4.30	-1.60	38.5
5753.12	4.26	-0.69	87.6
5778.45	2.59	-3.59	21.6
5811.92	4.14	-2.43	10.6
5814.81	4.28	-1.97	22.1
5849.68	3.69	-2.99	7.5
5858.78	4.22	-2.26	13.2
5927.79	4.65	-1.09	44.3
5956.69	0.86	-4.50	57.6
6034.03	4.31	-2.42	8.8
6120.24	0.92	-5.95	5.6
6151.62	2.18	-3.37	51.2
6159.37	4.61	-1.97	11.7
6165.36	4.14	-1.47	46.2
6187.99	3.94	-1.72	48.5
6226.73	3.88	-2.20	29.8
6265.13	2.18	-2.54	92.5
6380.75	4.19	-1.38	55.5
6392.54	2.28	-4.03	17.8
6498.94	0.96	-4.69	46.7
6509.61	4.08	-2.98	3.6
6591.33	4.59	-2.06	10.5
6593.87	2.43	-2.37	90.7
6597.56	4.79	-1.06	42.8
6608.02	2.28	-4.04	18.3
6609.11	2.56	-2.66	72.5
6646.93	2.61	-3.99	11.0
6667.42	2.45	-4.40	5.6
6667.73	4.58	-2.15	9.6

Table 2.3 (cont'd)

Wavelength (Angstroms)	Excitation Potential (eV)	Oscillator Strength (log gf)	Solar Equivalent Width (mÅ)
6699.16	4.59	-2.18	8.5
6703.57	2.76	-3.15	37.4
6704.48	4.22	-2.66	5.7
6710.32	1.49	-4.87	16.1
6725.35	4.10	-2.30	17.6
6732.07	4.58	-2.21	6.8
6739.52	1.56	-4.94	11.0
6745.09	4.58	-2.17	9.1
6745.95	4.08	-2.76	6.3
6746.95	2.61	-4.35	4.8
6753.47	4.56	-2.28	6.2
6837.02	4.59	-1.80	17.7
6839.83	2.56	-3.45	32.3
6843.65	4.55	-0.93	65.5
6851.63	1.61	-5.31	5.4
6857.24	4.08	-2.16	22.4
6862.49	4.56	-1.57	30.7
6978.85	2.48	-2.45	88.3

Table 2.4. List of Fe II lines

Wavelength (Angstroms)	Excitation Potential (eV)	Oscillator Strength (log gf)	Solar Equivalent Width (mÅ)
4413.60	2.68	-3.79	39.9
4491.40	2.86	-2.71	80.0
4582.84	2.84	-3.18	61.7
4620.52	2.83	-3.21	62.9
5132.67	2.81	-4.08	24.9
5197.58	3.23	-2.22	89.6
5234.62	3.22	-2.18	91.4
5264.81	3.23	-3.13	48.0
5325.55	3.22	-3.16	48.2
5414.07	3.22	-3.58	31.7
6084.11	3.20	-3.79	21.1
6149.26	3.89	-2.69	39.6
6247.56	3.89	-2.30	57.3
6369.46	2.89	-4.11	20.7
6383.72	5.55	-2.24	9.4
6416.92	3.89	-2.64	43.2
6446.41	6.22	-1.97	4.5
6516.08	2.89	-3.31	62.1
7222.39	3.89	-3.26	19.6
7224.49	3.89	-3.20	24.9
7515.83	3.90	-3.39	14.8
7711.72	3.90	-2.50	53.5

2.3.2 Calibration using the solar spectrum

We began the analysis by measuring iron line equivalent widths in a spectrum of the daytime sky, taken through the solar port of the 2.7m telescope. With these measurements in hand, we then used MOOG to constrain the effective temperature by eliminating any trend of iron abundance with excitation potential (i.e. by assuming excitation equilibrium). The microturbulent velocity was determined by eliminating any trend of abundance with reduced equivalent width (= EW/λ). The surface gravity was constrained by forcing the derived abundance using singly-ionized iron to match that of neutral iron (i.e. by assuming ionization equilibrium). During this process we rejected any lines that did not give "solar-like" parameters (most likely due to inaccurate oscillator strengths), leaving us with our final list of 65 Fe I and 22 Fe II lines, which was used to constrain the stellar parameters of all our target stars. Once these requirements were met, we used the resulting stellar parameters to construct a final model atmosphere and used this model to derive an average iron abundance. Figure 2.1 shows the results of these measurements, by plotting the derived solar Fe abundance from each line as a function of reduced equivalent width (top panel), or as a function of excitation potential (bottom panel). Our derived stellar parameters and iron abundance (used as a proxy in the model atmosphere for the overall metallicity) agree well with canonical values. From our fiducial solar spectrum, we derive $T_{\rm eff}$ = 5780 $\pm$ 70 K, $\log\, g$ = 4.50 $\pm$ 0.08 dex, and $v_{\rm mic}$ = 1.16 $\pm$ 0.04 km s^{-1}. We measure an iron abundance of $\log \epsilon$(Fe) = 7.52 $\pm$ 0.04.

Here we are using the normal notation where $\log \epsilon(\mathrm{X}) = 12.00 + \log \mathrm{N(X)/N(H)}$, so that $\log\ \epsilon = 12.00$ for hydrogen.

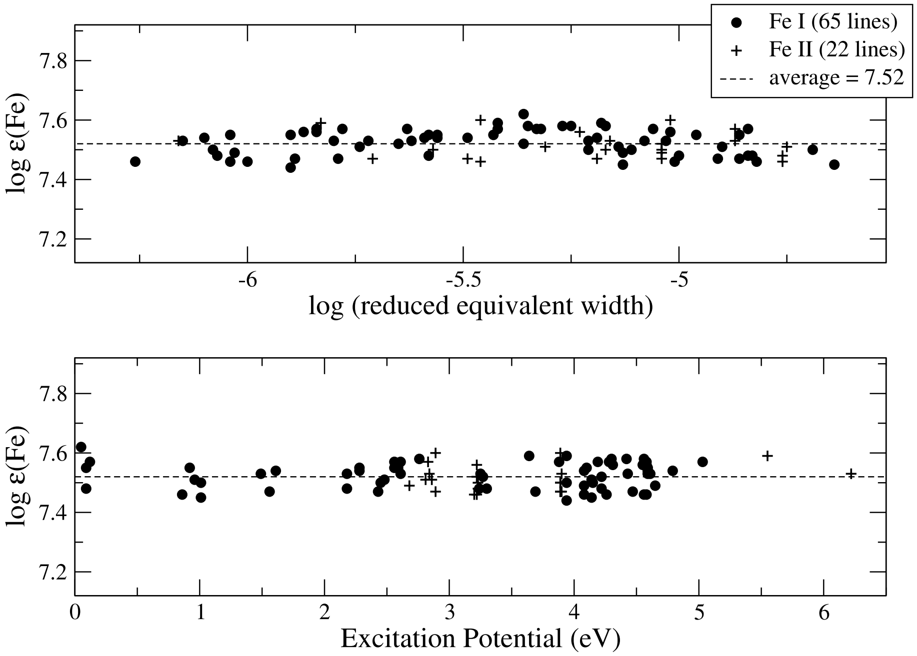

Figure 2.1 Plots of $\log\ \epsilon$(Fe) for each measured iron line in the Sun. A similar analysis was performed on each of our target stars in order to determine stellar atmospheric parameters. Effective temperature was constrained by eliminating any trend in iron abundance with excitation potential; microturbulent velocity by eliminating any trend with reduced equivalent width; and surface gravity by forcing the derived abundances of Fe I and Fe II to match. The top panel shows the derived solar iron abundance as a function of reduced equivalent width (= EW/λ); the bottom panel as a function of excitation potential. Fe I is represented by filled circles; Fe II by crosses.

We wish to stress that our derived iron abundances are based on one-dimensional, hydrostatic model atmospheres and the assumption of LTE. As such, they are likely subject to various uncertainties, including surface inhomogeneities and non-LTE effects (see Asplund 2005 for a thorough discussion of these effects); and perhaps even the effects of magnetic fields (Fabbian et al. 2010). However, non-LTE calculations predict relatively small effects for Sun-like stars, with larger effects seen at higher temperatures and lower surface gravities and metallicities. For our metal-rich sample of FGK dwarf and sub-giant stars, we expect non-LTE effects to be minimized. Furthermore, since our targets are sun-like stars, we expect any non-LTE effects to calibrate out (at least partially) when calculating a differential abundance with respect to the Sun.

The process described above was repeated for each star in our sample in order to determine stellar parameters and iron abundance. We then took the difference, on a line-by-line basis, of the derived iron abundance in the star and that of the solar port spectrum. Note that by calculating an average iron content difference based on a line-by-line analysis, uncertainties in the log gf values are removed from the differential iron abundance. Our derived iron abundances are thus quoted relative to the Sun in all cases.

2.3.3 Spectral synthesis of silicon and oxygen lines

With estimates of the stellar parameters in hand, we then determined the silicon and oxygen abundances. For these, we synthesized a small portion of the spectrum around each absorption feature considered. The program then varies the abundance of the species until the best fit (the minimum residual) to the observed spectrum is found. For Si we used six neutral lines between 5645 Å and 5793 Å in our analysis, listed in Table 2.5. The initial line lists used to construct the synthetic spectra were taken from the Kurucz (1993b) atomic linelist, and oscillator strengths were then adjusted where necessary to match our solar port spectrum. Figure 2.2 shows an example of the synthesis process for the Si I line at 5708 Å. We find an average Si abundance of $\log\ \epsilon(\mathrm{Si}) = 7.58 \pm 0.03$ from these six lines for the Sun. This value is somewhat higher than the $\log\ \epsilon(\mathrm{Si}) = 7.51 \pm 0.03$ reported in the recent work of Asplund et al. (2009); however, our stellar [Si/Fe] values are independent of the exact derived solar silicon abundance since our stellar abundances are ultimately calculated differentially with respect to the Sun. Note that we have chosen to ignore non-LTE effects in our Si I analysis, as these effects are thought to be quite small – on the order of 0.01 dex – in the Sun (Wedemeyer 2001, Shi et al. 2008).

Table 2.5. List of Si I lines

Wavelength (Angstroms)	Excitation Potential (eV)	Oscillator Strength (log gf)
5645.61	4.93	-2.10
5665.56	4.92	-2.07
5684.48	4.95	-1.62
5708.40	4.95	-1.47
5772.15	5.08	-1.71
5793.07	4.93	-2.05

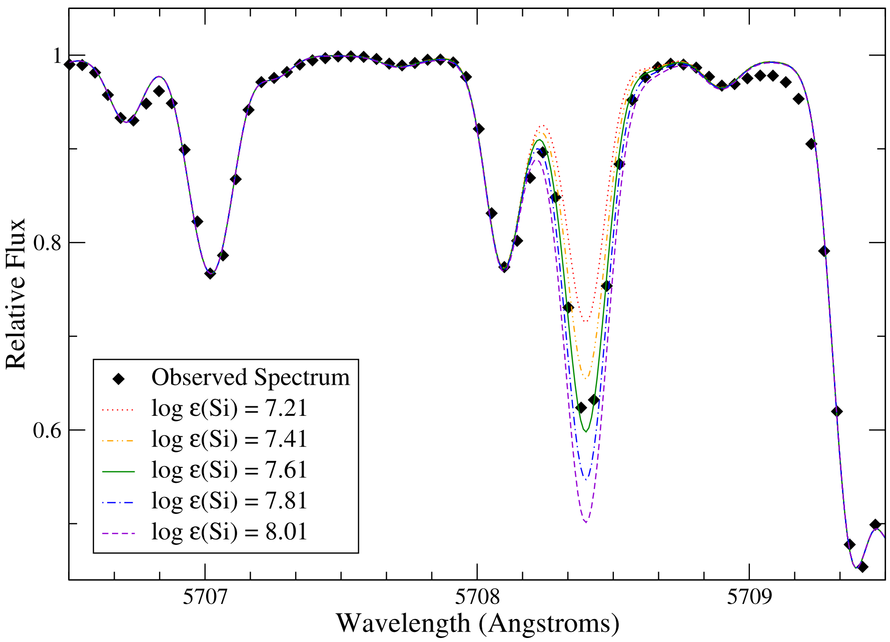

Figure 2.2 A MOOG-synthesized portion of the solar spectrum around the 5708 Å Si I absorption feature. Similar synthetic spectra were used to determine Si and O abundances in each of our target stars, by minimizing the residuals to the fits of the various observed spectra. The plot displays the observed solar port spectrum as diamond symbols, and the synthetic spectra as lines. In this synthesis, the silicon abundance was varied by ± 0.2 dex and ± 0.4 dex from the best-fit value of $\log\ \epsilon$(Si) = 7.61.

For oxygen, we used the allowed transition triplet at 7771 Å, 7774 Å and 7775 Å. These lines have high excitation potentials (9.15 eV) and are known to be formed under conditions that depart significantly from the LTE approximation (cf. Kiselman 1993, 2001). These non-LTE effects are appreciable – on the order of a few tenths of a dex (LTE assumptions always result in an overestimation of the abundance derived from the oxygen triplet) – and are sensitive to stellar atmospheric parameters (temperature, gravity and overall metallicity) and to the efficiency of collisions with hydrogen that is adopted in the non-LTE calculations (Takeda & Honda 2005, Fabbian et al. 2009). We have chosen to apply the non-LTE corrections of Ramírez, Allende Prieto & Lambert (2007) to our derived oxygen abundances. (Note that they chose to ignore inelastic collisions with neutral hydrogen atoms, as these collisions are expected to play a small role at solar metallicities.) We first synthesized each line of the triplet individually, and then applied the corrections on a line-by-line basis. For the Sun, we obtained an average non-LTE correction of -0.13 dex, yielding an oxygen abundance of $\log\ \epsilon$(O) = 8.70 ± 0.04. This is in good agreement with the $\log\ \epsilon$(O) = 8.69 value reported by Asplund et al. (2009); although, as with silicon, our differential stellar [O/Fe] values are independent of the exact derived solar oxygen abundance value. The average $\log\ \epsilon$(O) non-LTE correction for all our targets was -0.16 dex, with a range from -0.39 dex to -0.04 dex. The application of the corrections reduced the scatter in our [O/Fe] measurements by approximately 20%.

The final step in the process of determining silicon and oxygen abundances was to calculate the difference, on a line-by-line basis, between our target stars and the Sun. Our quoted Si and O abundances are therefore differential with respect to the Sun in all cases.

2.4 Measurement Repeatability and Uncertainties

In an effort to characterize the random errors in our atmospheric parameter determinations, we obtained and analyzed 22 separate observations of the field dwarfs 47 UMa (a G1 V star) and 70 Vir (G4 V) on the 2.7m telescope, and 20 separate observations of 70 Vir with the HET. These observations were made using the same instruments and configurations as our program stars, and were subjected to identical analysis methods. Figures 2.3 and 2.4 show histograms of the derived [Fe/H] and T_{eff} for the two sets of observations of 70 Vir. The maximum standard deviations for these measurements are 0.01 dex for [Fe/H]; 10 K for effective temperature; 0.03 dex for $\log\ g$; and 0.04 km s^{-1} for microturbulent velocity (v_{mic}). Our analysis of 47 UMa yielded similar results. These represent our internal "repeatability" precisions. The small offsets of 20 K in the mean derived effective temperature and 0.01 dex in the mean derived [Fe/H] are most likely due to the differing number of pixels per resolution element of the two instruments. Given that these offsets are both a factor of a few smaller than our total error budget, we have not attempted to correct for these minimal differences.

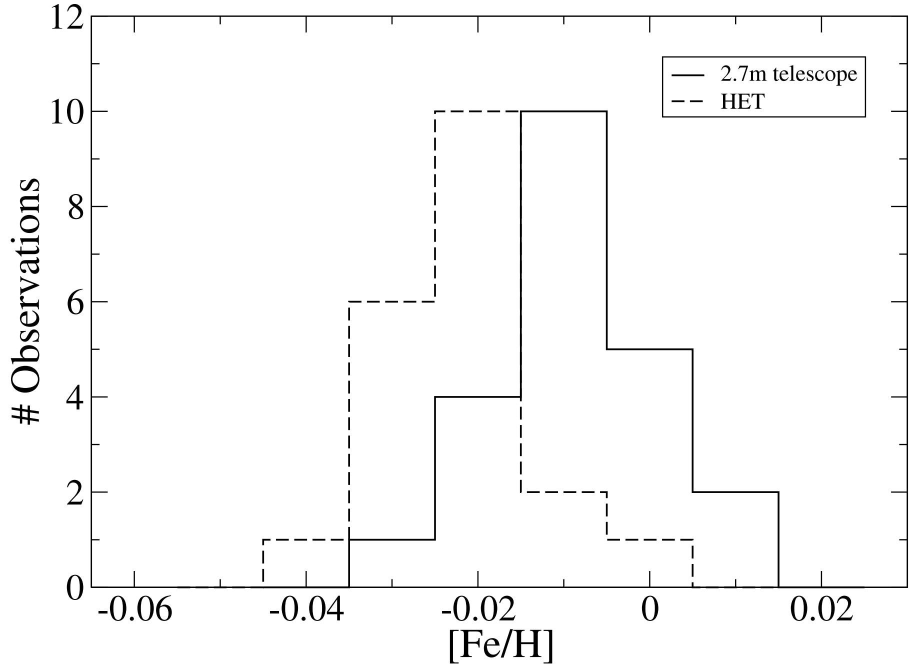

Figure 2.3 Histograms showing the number of observations of 70 Vir as a function of [Fe/H] for the 2.7m telescope (solid line, 22 observations in total) and HET (dashed line, 20 observations in total). The distributions appear roughly gaussian, with a standard deviation of 0.01 dex in both cases. Note the small bin size of 0.01 dex. Our measurements are highly repeatable, with a minimal offset of 0.01 dex in the mean derived abundances from the two instruments. This difference is well within our error bars and is likely due to the differing number of pixels per resolution element on the two detectors.

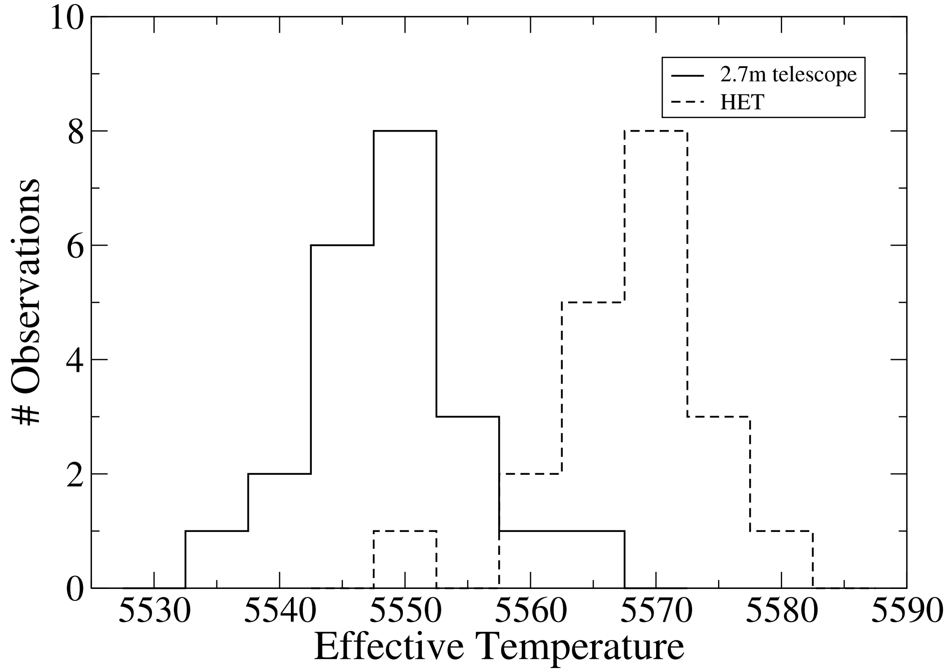

Figure 2.4 Histograms showing the number of observations of 70 Vir as a function of effective temperature for the 2.7m telescope (solid line, 22 observations in total) and HET (dashed line, 20 observations in total). The distributions appear roughly gaussian, with a standard deviation of 10 K in both cases. Note the small bin size of 5 K. Our measurements are highly repeatable, with a minimal offset of 20 K in the mean derived temperatures from the two instruments. This difference is well within our error bars and is likely due to the differing number of pixels per resolution element on the two detectors.

To get an estimate of the accuracy of our measurements, we compared our results to other work in the literature. Thirty of our 76 planet-host stars also appear in the Fischer & Valenti (2005) dataset, and 31 of the remaining 46 have stellar parameters listed from at least one source in SIMBAD and/or NStED. Sixty-two of our 80 non-host stars have stellar parameters listed from at least one source in the online databases. For these, we averaged the difference between our results and those of Fischer & Valenti or the databases, yielding standard deviations of 0.06 dex for [Fe/H]; 70 K for effective temperature; and 0.08 dex for log g. Note that microturbulent velocities are not typically reported in the literature.

In order to characterize our systematic errors, we then performed an analysis of the sensitivity of our derived abundances to variations in the stellar atmospheric parameters. We chose 16 Cyg B – a G3 V dwarf – for this analysis, as its stellar parameters are typical of our sample. After varying the parameters by the amounts discussed in the previous paragraph, we find systematic uncertainties of ± 0.02 dex in silicon and ± 0.11 dex in oxygen.

The precisions of our Si and O measurements are approximately 0.03 dex and 0.04 dex, respectively. We estimated these by simply averaging the standard deviations of the derived abundances for the six Si lines and three O lines in all our program stars. Adding these random uncertainties and the systematic uncertainties in quadrature yields final errors of ± 0.04 dex for silicon and ± 0.12 dex for oxygen. Since all measurements were made relative to the Sun, we stress that we have not attempted to determine the absolute abundances of Si or O; rather, we simply wish to rank our targets from least to most silicon/oxygen-rich.

2.5 Statistical Methods

Figures 2.5 and 2.6 show scatter plots of our derived [Si/Fe] and [O/Fe] abundances, as a function of [Fe/H]. In both cases, we recover the overall distribution expected for field stars (e.g. Timmes et al. 1995), whereby Si and O are overabundant relative to Fe for more metal-poor stars. The slope of [Si/Fe] flattens out around [Fe/H] of zero, while the slope of [O/Fe] turns further negative at supra-solar metallicities. Thus, we see that the distributions follow a sequence constrained by the Galactic chemical enrichment history. For metallicity bins already well-populated in our sample ([Fe/H] of -0.2 to +0.4 dex), we observe that our host stars tend to be enriched in Si compared to non-host stars. Indeed, two-thirds of our host stars lie at or above [Si/Fe] of zero; while three-fourths of our non-host stars lie at or below [Si/Fe] of zero. We observe no such tendency for oxygen.

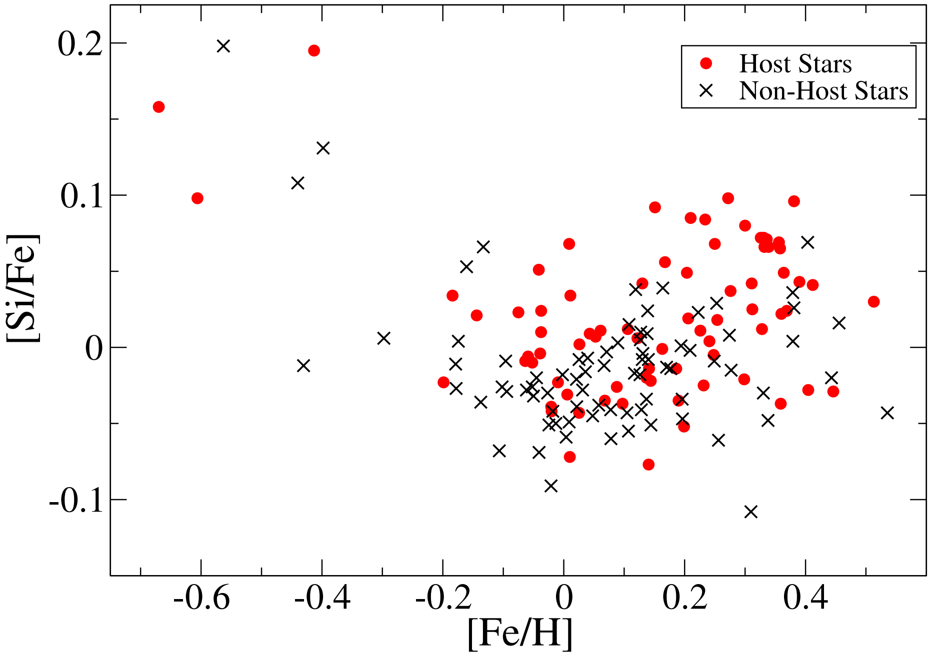

Figure 2.5 A plot of [Si/Fe] as a function of [Fe/H] for our sample. At iron abundances above [Fe/H] of -0.2 dex, where the vast majority of our sample lies, we observe that the planet-hosting stars in our sample tend to be enhanced in silicon when compared to stars without any known giant planets. Two-thirds of the host stars lie at or above [Si/Fe] of zero, while three-fourths of our non-host stars lie at or below [Si/Fe] of zero. We note that the distribution agrees well with galactic chemical evolution models and observations (e.g. Timmes et al. 1995). Planet-hosting stars are represented by filled circles; non-host stars by crosses.

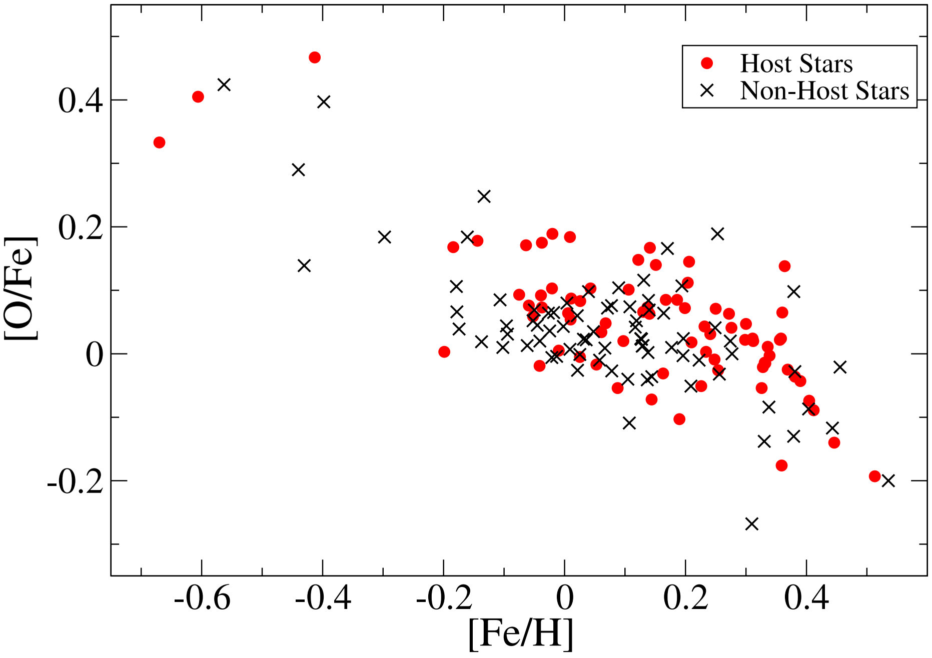

Figure 2.6 A plot of [O/Fe] as a function of [Fe/H] for our sample. No discernible trends are apparent between planet-hosting stars and non-host stars in our sample. We note that the distribution agrees well with galactic chemical evolution models and observations (e.g. Timmes et al. 1995). Planet-hosts are represented by filled circles; non-hosts by crosses.

In order to quantify any potential differences in the Si and O distributions of stars with and without planets, the fact that planet-hosting stars tend to have higher overall metal content than typical nearby stars needs to be taken into account. The more metal-rich nature of stars hosting giant planets now seems well-established (Gonzalez 1997, 1998, 1999; Santos et al. 2005; Fischer & Valenti 2005). This means that the locus of typical giant-planet-hosting stars is shifted towards higher overall [Fe/H] compared to the locus of typical local field stars. Figure 2.7 is a cartoon depicting the situation. Stars with and without planets appear to follow the same general Galactic chemical evolution trend (Bodaghee et al. 2003, Santos et a. 2005), but because this trend is not flat, the expected average [Si/Fe] of the two groups of stars is different, for reasons having nothing to do with planets. Since any difference in oxygen and silicon that is related to planets would be a small effect, it is imperative that the overall [Fe/H] distribution of any studied planet-host sample match that of the control sample of field stars. Ideally, this could be accomplished by constructing arbitrarily large samples of stars, making it possible to separate the planet-host and control samples into arbitrarily small [Fe/H] bins and still leave a statistically significant number of targets in each bin. In such an ideal case, determining whether a significant difference in the silicon and oxygen content between the two samples is present would be trivial. Absent an infinite data set, another possibility is to select matching samples a priori – that is, to ensure samples are constructed such that every planet-host has a matching control star at the exact same [Fe/H]. As described in section 2, we chose non-host stars for our analysis in such a manner that the distributions of [Fe/H] for our host and non-host samples were as similar as possible. Perfect matching proved impossible, however, given the finite number of non-hosts in the MOPS parent sample, as well as the uncertainties in determining stellar parameters – targets selected beforehand for a specific [Fe/H] often ended up at a slightly different [Fe/H] after analysis. We describe our approach to the problem of matching metallicity distributions – and of compensating for imperfect matching – below.

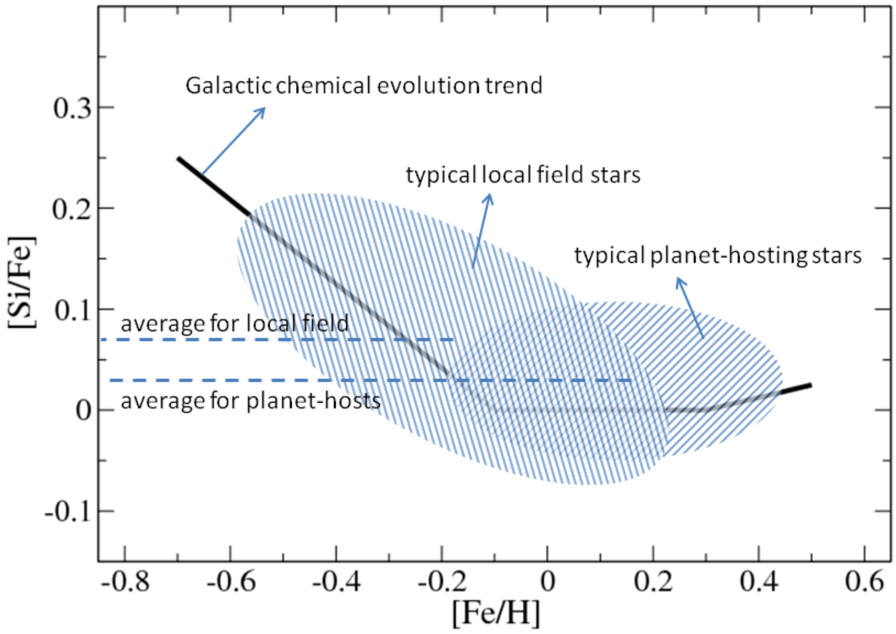

Figure 2.7 A cartoon demonstrating the need for careful matching of the underlying [Fe/H] distributions for any sample of planet-hosting stars to the control set of field stars. Planet hosts appear to follow the same general galactic chemical evolution trend as typical field stars, but tend to preferentially lie on the iron-rich end of the distribution (Bodaghee et al. 2003, Santos et a. 2005). Since the trend is not flat, the expected average [Si/Fe] for the typical local field is different than the expected average for planet-hosting stars. It is therefore imperative that the underlying [Fe/H] distribution of the control sample match that of the planet-host sample, by selecting local field stars that are more metal-rich than average.

Although our samples contain large numbers of targets, we nevertheless do not have enough data to adequately bin the samples by [Fe/H] and still have a statistically significant number of stars in each bin. We therefore require a statistical method for quantifying the difference, or lack thereof, between the distributions of [Si/Fe] and [O/Fe] in our planet-host and non-host stars. To accomplish this objective, we performed a bootstrapped Monte Carlo simulation. The process is described below. Note that we first removed the three planet-hosts and five non-planet-hosts at [Fe/H] $<$ -0.2 dex from our sample, as this region is very poorly populated.

Create realization of planet hosts

1. We created a realization of the observed planet hosts, as follows:
    - We randomly drew a number between 30 and 60, to determine the size of the realization.
    - We then selected this number of planet hosts, using random sampling with replacement (meaning some stars may have been duplicates).

Calculate [Fe/H] histogram for planet hosts

2. We determined the [Fe/H] distribution of the planet-host realization by calculating a histogram with bins of width 0.1 dex.

Create realization of non-hosts

3. We created a realization of the observed non-host stars by randomly selecting – again with replacement – a number of stars equal to the size of the host realization, while forcing the [Fe/H] distribution to match (or as closely as possible) that of the host sample. This was done in the following manner:

    - We randomly drew a number between zero and one.
    - If this probability was lower than the normalized [Fe/H] distribution of the host set at the metallicity of the non-host, we included the star in our non-host realization. If not, we rejected the selection.
    - This process was repeated until a number of non-hosts equal to the size of the host realization was selected.

Calculate [Fe/H] histogram for non-hosts

4. We determined the [Fe/H] distribution of the non-host realization by calculating a histogram with bins of width 0.1 dex.

Evaluate difference

5. We then performed two-sided Kolmogorov-Smirnov (K-S) tests on the [Fe/H], [Si/Fe] and [O/Fe] distributions of the two sets.

6. The entire process was repeated 10^6 times, and the K-S probability was noted for each trial.

The process described in step 3 above, in which we construct pairs of samples with iron abundance distributions that match as closely as possible, is crucial to our experiment, since we do not wish to simply reproduce the known planet-metallicity correlation. Rather, we wish to know whether differences exist between our host and control sets at a given [Fe/H]. Since any minor differences in the distributions of a single trial will average out over 10^6 trials, forcing the iron distributions to match in this manner serves as a method for binning our data by [Fe/H].

Given the finite nature of our samples, the statistical procedure explained above offers an excellent method for determining any possible compositional differences in individual elements between host and non-host stars. The results of our experiment are explained in the following section.

2.6 Results

Our statistical investigation of the silicon and oxygen content of stars hosting giant planets reveals a distinct compositional difference for silicon, but not for oxygen, when these stars are compared to similarly iron-rich non-host stars. In figure 2.8 we show that the [Si/Fe] distributions of planet-hosts and non-hosts are significantly different. The variable on the horizontal axis is the K-S probability, which is a measure of the statistical significance of the difference between the cumulative distributions of two samples. In this sense, it measures the probability that two samples were drawn from the same parent distribution. Thus, a low K-S probability is consistent with the host and non-host samples being drawn from different distributions, while a high probability indicates similar parent distributions. The peak at a K-S probability of zero in figure 8 is strong evidence of such a difference. In figure 2.9 we show the same plot for oxygen, where we see little evidence of a difference for [O/Fe].

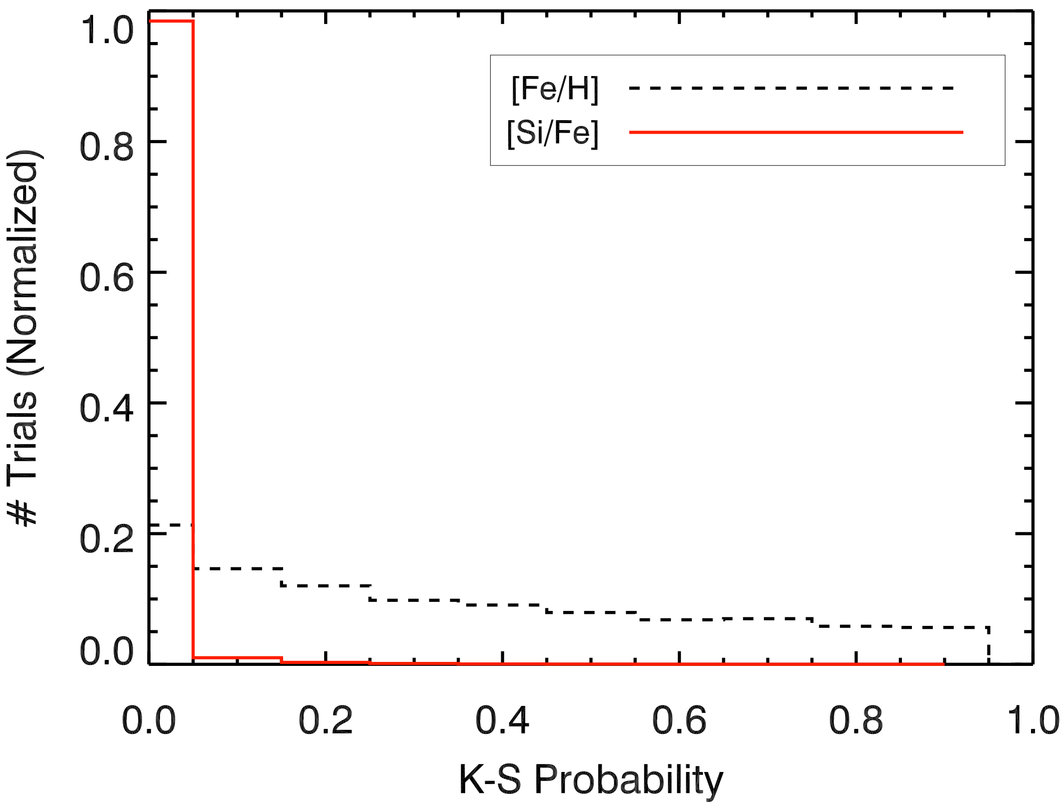

Figure 2.8 A histogram of the percentage of trials vs. probability for [Si/Fe] (solid line) and [Fe/H] (dashed line; shown for reference), with bin widths of 0.10. The peak at a K-S probability of zero is strong evidence of a difference in the Si abundances of our planet-host and non-host samples.

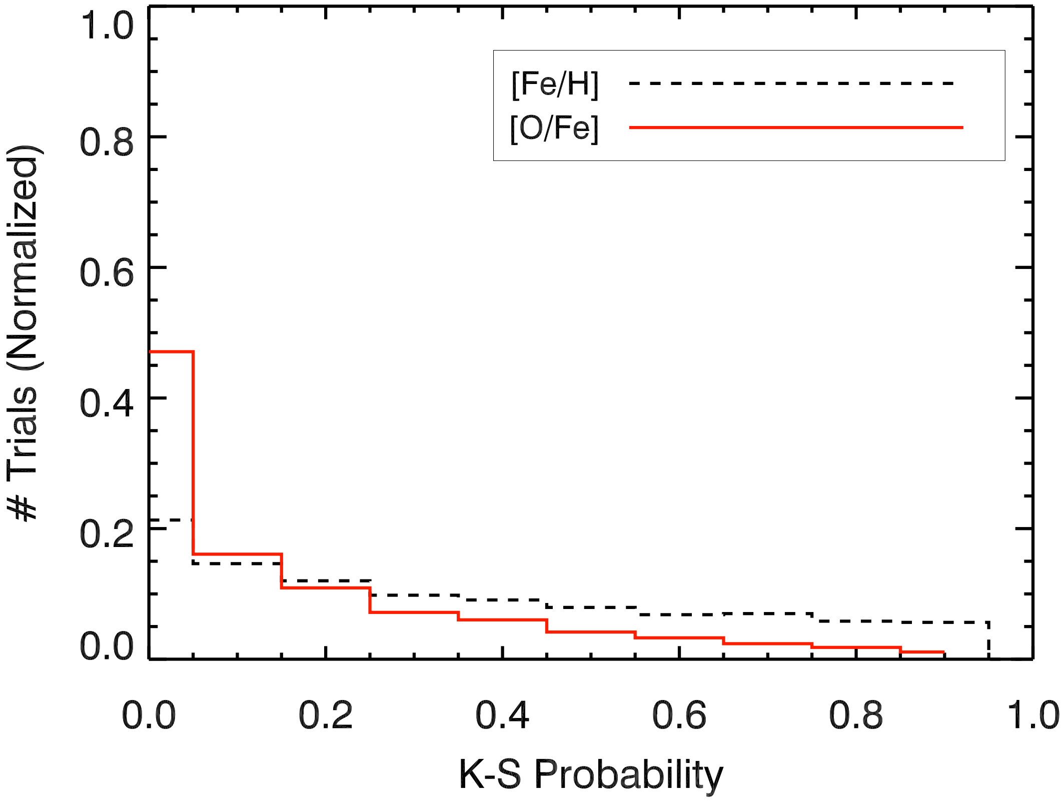

Figure 2.9 A histogram of the percentage of trials vs. probability for [O/Fe] (solid line) and [Fe/H] (dashed line; shown for reference), with bin widths of 0.10. The histogram for [O/Fe] appears qualitatively similar to that for [Fe/H], indicating no significant difference in the O abundances of our planet-host and non-host samples.

The dashed line in figures 2.8 and 2.9 depicts the K-S probability for [Fe/H], which shows that our matching of host stars to equally iron-rich non-host stars was not perfect. For perfect control sets in each trial, we would expect the dashed lines to have single peaks at probability = 1. Better matching could be achieved with smaller histogram bin widths, but this would require unrealistically larger samples to draw from. We note, however, that we have devised a mathematical method to control for this imperfect matching, as discussed below.

In order to quantify the difference, or lack thereof, in the distributions of Si and O, we devised a "total" probability P, representing the product of integrated K-S probabilities for [Fe/H] and [Si/Fe] or [O/Fe] divided by the integrated [Fe/H] probability squared:

$$P_X = \frac{\int_0^1 f_{[X/Fe]} f_{[Fe/H]} p dp}{\int_0^1 f_{[Fe/H]}^2 p dp} \tag{2.1}$$

where *f* represents the percentage in a particular probability bin *p* of width *dp*. This equation represents a method of controlling for spurious low K-S statistics that result from the [Fe/H] distributions of our two sets not matching perfectly in some trials. That is, if the underlying Fe distributions don't match, we can't expect the Si or O distributions to match.

With this definition in hand, and using a probability bin size of dp = 0.10, we find a total probability for Si and O of:

$$P_{Si} = 0.01 \tag{2.2}$$

$$P_O = 0.57 \tag{2.3}$$

The small total Si probability is consistent with the hosts and non-hosts in our sample being drawn from separate parent distributions of stars. Put differently, there is only a 1% chance that the planet-harboring stars and non-planet-harboring stars in our sample were drawn from the same parent distribution. The results of our statistical analysis therefore suggest a significant difference in the Si abundances of planet host stars, when compared to stars hosting no known giant planets. The rather large total O probability is consistent with the samples being drawn from the same parent distribution (a 57% chance).

2.7 Conclusions and Future Work

We have determined stellar atmospheric parameters and derived differential abundances of Fe, Si, and O for a uniform sample of 76 planet-host stars and 80 non-host stars, using high resolution and high signal-to-noise data obtained on the 2.7m and HET telescopes at McDonald Observatory. We find a statistically significant difference in the [Si/Fe] distribution between the two groups of stars. This result lends strong support to the core-accretion theory of planet formation, since much of the solid material available for core formation is thought to consist of silicate grains with icy mantles. We find no statistically significant difference in the [O/Fe] distributions. Although the uncertainties in our oxygen measurements are significantly larger than for silicon, we nevertheless find it unlikely that a statistically significant trend – at the level of that seen with silicon – would emerge with smaller error bars. Reducing the error bars would likely require 3D model atmospheres and the incorporation of non-LTE effects in the line formation process. Such models are becoming available (Asplund 2005), and future studies could likely measure oxygen to higher precision with the use of these.

The lack of a trend with oxygen is a surprising result, as we would expect this alpha element to track the silicon abundance (as predicted in Robinson et al. 2006). Our interpretation is that the stellar photospheres are tracing species important for grain nucleation, rather than subsequent icy mantle growth. Since silicon rather than oxygen is the limiting reagent for grain nucleation, the entire process of dust formation would in that case depend on the silicon abundance. Oxygen is so over-abundant relative to refractory species that the process of core accretion may be insensitive to variations in the overall oxygen abundance. We liken the process to cloud formation on Earth, in which condensation nuclei play a key role. The atmosphere may be virtually saturated with water vapor, but without seeds (such as dust, sea salt and bacteria) onto which this vapor can condense, no clouds can form. We posit that silicon and other refractory elements serve as these seeds in protostellar discs. Without them, the process of giant planet formation may be independent of the amount of volatile material available.

When comparing our results to the work of others, we note the studies by Meléndez et al. (2009) and Ramírez et al. (2009, 2010), who argue that the Sun is deficient in refractory elements relative to volatile elements when compared to nearby solar twins and solar analogs. They attribute this difference to efficient planet formation around the Sun, whereby refractory elements were preferentially locked up in the terrestrial planets during the early protostellar period. At first glance, this result seems to contradict our findings, but further inspection reveals that for silicon specifically the results are inconclusive. Meléndez et al. (2009) actually find that Si is enhanced by ∽0.03 dex in the Sun when compared to the average Si abundance of their sample of 21 solar twins and analogs, while Ramírez et al. (2009) find a ∽0.03 dex decrement in the Sun when compared to the average Si abundance of their sample of 64 solar twins and analogs. Ramírez et al. (2010) report no difference at all in their meta-analysis of solar analogs from six independent studies. Further studies addressing any possible difference in the silicon content of the Sun compared to solar twins and analogs need to be performed before any definite conclusions can be made.

Based on our results and interpretation, we predict that planet detection rate should correlate positively with host star abundance for those elements responsible for grain nucleation, and that no such trend should exist for the most abundant volatile elements responsible for icy mantle growth. The most important refractory contributors to the composition of dust in planet-forming regions are thought to be silicon, iron, magnesium, sulfur and aluminum; while the most important volatiles are probably oxygen, carbon and nitrogen. Carbon is an interesting case in that it might contribute significant mass both to grain nuclei and icy mantles. Henning & Salama (1998) argue that up to 20% of the carbon in the universe is probably locked in refractory grains, while simulations by Dodson-Robinson & Bodenheimer (2010) demonstrate that the ice giants Uranus and Neptune required solid methane in their feeding zones to grow to their present size. Hence, we expect it to contribute significant amounts of mass to giant planet cores; and we predict that planet detection rate should correlate positively with host star carbon abundance for any population of planets formed by core accretion.

The present analysis represents an important "first look" study in which we focused on the single most abundant volatile contributor to dust grains (oxygen), and the single most important refractory contributor (silicon) after iron. Our future work will involve a more comprehensive analysis, in which we will increase our sample sizes, to allow for better matching of the overall metallicity distributions of our planet-host and control samples, and increase the number of studied species to include the most abundant elements (discussed above) thought to be important for planet-formation.

E.B.'s and S.D.R.'s work was funded by the University of Texas through a faculty startup package awarded to S.D.R. W.D.C.'s work was made possible by funding through NASA Origins grant NNX09AB30G. C.S.'s work was made possible by funding through NSF grant AST 09-08978.

This research has made use of the NASA/IPAC/NExScI Star and Exoplanet Database, which is operated by the Jet Propulsion Laboratory, California Institute of Technology, under contract with the National Aeronautics and Space Administration. This research has also made use of the SIMBAD database, operated at CDS, Strasbourg, France. The Hobby-Eberly Telescope is a joint project of the University of Texas at Austin, the Pennsylvania State University, Stanford University, the Ludwig Maximilians-Universität München, and the Georg-August-Universität at Göttingen. The HET is named in honor of its principal benefactors, William P. Hobby and Robert E. Eberly.

The authors thank Ian Roederer for the use of his IDL equivalent width measurement software; Ivan Ramírez for providing his grid of non-LTE oxygen corrections, along with an IDL routine for interpolating within this grid; and Julia Bryson for help measuring iron abundances. We are grateful to the anonymous referee, whose careful reading and many suggestions helped improve the manuscript.

Finally, we would like to thank all the people who have helped gather data over the years for the 2.7m radial velocity search program at McDonald Observatory, including Phillip MacQueen, Mike Endl, Paul Robertson, Rob Wittenmyer, Diane Paulsen, and Artie Hatzes.

Chapter 3

The McDonald Observatory Planet Search: Two New Long-Period Giant Planets and Two Cases of Long-Period RV Signals Related to Stellar Activity

3.1 Introduction

"How common are solar system analogs?" Until relatively recently, this fundamental question had little in the way of observational answers. Although the *Kepler* mission (Borucki et al. 2010) has helped us place constraints on an answer to the related question of "how common are Earth analogs?", until our instruments and techniques improve to the point that we are capable of detecting the range of analogous solar system masses, a definitive answer is beyond our reach. However, as a next first step we might instead ask: "how common are Jupiter analogs?" As the time baseline of radial velocity searches grows, we are becoming better equipped to answer this last question.

The radial velocity (RV) technique has been used to detect/discover $\backsim$600 of the $\backsim$2000 known, confirmed exoplanets (as of mid-2014). Since the technique is heavily biased towards massive planets in short-period orbits, the majority of these are gas-giants in orbits of less than one Earth-year.

Only about 25 of these can be considered "Jupiter analogs", which we define as within a factor of a few Jupiter-masses and in orbits longer than 8 years (about 3000 days). Although the *Kepler* spacecraft – utilizing the planet transit method – has delivered ∽1000 planets and a further ∽3000 candidates, none of these can be classified as "long-period", due to the limited time baseline of the mission data.

Finding and characterizing such long-period Jovian planets is arguably more important to answering the uniqueness question, since it seems terrestrial planets are everywhere (Howard et al. 2012, Wittenmyer et al. 2011b, Fressin et al. 2013, Petigura et al. 2013) but Jupiter analogs are rather rare, even though surveys like The McDonald Observatory Planet Search and Anglo-Australian Planet Search have "outgrown" the time-baseline selection bias. While *Kepler* has revolutionized exoplanetary science and provided a first estimate of the frequency of Earth-size planets in Earth-like orbits, long-term radial-velocity surveys complement these data with measurements of the frequency of Jupiter-like planets in Jupiter-like orbits. This in turn will reveal how common Solar-system-like architectures are.

While the idea that Jupiter analogues are required to shield terrestrial planets from impacts has been conclusively dismantled (e.g. (26), (27)), the presence of Jupiter analogues is a critical component for the delivery of water to planets that would otherwise have formed as dry, lifeless husks (Horner & Jones 2010, Raymond 2006). The search for Jupiter analogues thus provides a key datum for models of planetary formation and evolution - attempting to answer the question"how common are planetary systems like our own."

The McDonald Observatory Planet Search (Cochran & Hatzes 1993) is a high precision RV survey of hundreds of FGKM stars, begun in 1987 using the 2.7 m Harlan J. Smith (HJS) telescope. Since our migration to our current instrumental configuration in 1998 ("Phase III", described in Hatzes et al. 2003), we achieve routine internal velocity precision of 5∽9 m s^{-1}. With this precision and an observational time baseline approaching 17 years, we are now sensitive to Jovian analogues. In this paper, we present three such substellar companions. We also report two cases of Keplerian-like signals that appear to be due to stellar magnetic activity.

3.2 Observations

Our radial velocity measurements were obtained using the HJS and Keck I telescopes. The specific instruments/observations are described below.

3.2.1 Harlan J. Smith Telescope Observations

For the 2.7 m HJS telescope, we utilize the cross-dispersed echelle Tull Spectrograph (Tull et al. 1994). Our configuration uses a 1.2 arcsec slit, a grating with 52.67 groove mm^{-1}, and a 2048x2048 Tektronix CCD with 24 μm pixels, yielding a resolving power ($=\lambda/\Delta\lambda$) of R=60,000. The wavelength coverage extends from 3,750 $\AA$ to 10,200 $\AA$, and is complete from the blue end to 5,691 $\mathring{A}$, after which there are increasingly large inter-order gaps.

3.2.2 Keck Telescope Observations

For HD 95872, we also obtained 10 precise RV measurements using Keck/HIRES during three observing runs allocated to the NASA CoRoT key science project, during times when the CoRoT fields were unobservable.

The spectra for HD 95872 were taken with HIRES with a resolving powerof $R = 60,000$, using an instrumental setup similar to the California Planet Search (e.g. Howard et al. 2010). The iodine cell setup was utilized to monitor real time instrumental variations relevant to measuring precise radial velocities.

3.2.3 Data Reduction

The raw CCD data were reduced using a pipeline written by WC, implemented in the Image Reduction and Analysis Facility (IRAF) using standard routines within the `echelle` and `onedspec` packages. The process includes overscan trimming, bad pixel processing, bias frame subtraction, scattered light removal, flat field division, order extraction, and wavelength solution application using a Th-Ar calibration lamp spectrum. Most cosmic rays are succesfully removed via IRAFs interpolation routines; however, particularly troublesome hits are removed by hand.

3.3 Analysis

3.3.1 Radial Velocity Measurements

Our radial velocity measurements were obtained using our standard iodine cell RV reduction pipeline `Austral` (Endl, Kürster, & Els 2000). Our approach follows the standard iodine cell data analysis methodology: the stellar RV is calculated by comparing all spectra of the target star, taken with the iodine cell, with a high S/N stellar template spectrum free of iodine lines. During regular RV observations the temperature-controlled iodine cell is inserted in the light path and superimposes a dense reference spectrum onto the stellar spectrum. The iodine lines thus provide a simultaneous wavelength calibration and allow the reconstruction of the shape of the instrumental profile at the time of observation. The iodine cell at the HJST has been in regular operation for more than two decades.

3.3.2 Stellar Activity Indicators

As a check against photospheric activity masquerading as planet-like Keplerian motion, we measure the Ca H and K Mount Wilson S_{HK} index simultaneously with each RV data point. In addition, we have calculated the line bisector velocity spans (BVSs; Brown et al. 2008) of lines outside the region of iodine cell absorption. These time-series measurements are then checked for any possible correlation(s) with the RV measurements.

3.3.3 Stellar Characterization

We determined stellar atmospheric parameters for all four stars using a traditional absorption line curve-of-growth approach, following a procedure similar to that outlined in Brugamyer et al. (2011). The method utilizes an updated list of suitable Fe and Ti lines, the local thermodynamic equilibrium (LTE) line analysis and spectral synthesis code `MOOG`[1], and a grid of 1-D, plane-parallel `ATLAS9` (Kurucz 1993) model atmospheres. We first manually measured the equivalent widths of 132 Fe I and 41 Ti I lines, along with 18 Fe II and 8 Ti II lines, in our template spectra (without the reference iodine cell in the light path). With these measurements in hand, stellar effective temperature is constrained by assuming and enforcing excitation equilibrium – by varying the model atmosphere temperature until any trends in derived abundances with temperature are removed. Surface gravity is constrained by assuming and enforcing ionization equilibrium – by varying the model atmosphere gravity until the derived abundances of neutrals and ions agree. Microturbulent velocity is constrained by forcing the derived abundances for stronger lines to match those for weaker lines. For these processes, we used a weighted average of Fe (2x) and Ti (1x) when computing the relevant slopes/offsets.

The results of our stellar characterization are summarized in Table 3.1. Spectral types, photometric data, and parallaxes are taken from the

---

[1] available at http://www.as.utexas.edu/∽chris/moog.html

ASCC-2.5 catalog (Version 3; Kharchenko & Roeser 2009). We also include mass and age estimates from Yonsei-Yale model isochrones.

Using the stellar parameters T_{eff}, $\log g$, [Fe/H], and their errors, we determined the masses and ages of our stars using the procedure outlined in Ramírez et al. (55, their Section 4.5). Briefly, the location of each star on stellar parameter space was compared to that of stellar interior and evolution model predictions. The Yonsei-Yale isochrone grid (80, 33) was used in our implementation. Each isochrone point was given a probability of representing an observation based on its distance from the measured stellar parameters and weighted by the observational errors. Then, mass and age probability distribution functions were computed by adding the probabilities of individual isochrone points binned in mass and age, respectively. The peaks of these distributions were adopted as the most probable mass and age, while the $1\,\sigma$-like widths were used to estimate the errors.

Contrary to a more common practice, we did not use parallaxes in our mass and age determinations. This is because one of our stars, HD 95872, does not have a reliable measurement of trigonometric parallax; this star was not included in the *Hipparcos* catalog. To maintain consistency in our analysis, we employed the spectroscopic $\log g$ values as luminosity indicators instead of absolute magnitudes computed using measured parallaxes. If we had used the *Hipparcos* parallaxes for the three stars which have those values available, their masses would be only about $0.01 \pm 0.01\,M_{\odot}$ smaller.

Table 3.1. Stellar Properties

Star	T_{eff} (K)	log g	[Fe/H]	ξ (km s^{-1})	Mass ($M_\odot$)	Age (Gyr)
HD 95872	5312 ± 100	4.43 ± 0.15	0.41 ± 0.09	0.84 ± 0.15	0.95 ± 0.04	10.0 ± 3.7
ψ^1 Dra B	6212 ± 75	4.20 ± 0.12	0.01 ± 0.06	1.45 ± 0.10	1.19 ± 0.07	3.3 ± 1.0
HD 10086	5722 ± 65	4.43 ± 0.10	0.10 ± 0.04	1.23 ± 0.08	1.01 ± 0.03	5.5 ± 2.3
β Vir	6145 ± 75	3.98 ± 0.12	0.15 ± 0.05	1.51 ± 0.10	1.34 ± 0.10	3.2 ± 0.7

3.3.4 Planetary Orbit Modelling

We performed our planetary orbit modelling using the `Systemic Console`[2] package (Meschiari et al. 2009), a software application for the analysis and fitting of Doppler RV datasets.

3.4 Two New Planetary Systems

3.4.1 HD 95872

HD 95872 was originally selected for monitoring by MS & ME from a sample of 22 thin disk stars observed by MS on the 2.7 m in 1998 for a project to characterize the metal rich end of chemical evolution of the Galactic disk. The sample of 22 stars were selected by M. Grenon (Observatorie de Geneve) for Sandra Castro (ESO) and MS on the basis of their extreme kinematical (perigalactica $\sim$ 3 kpc) and photometric properties.

Table 3.2 presents the complete set of our RV observations for HD 95872. The RV coverage spans approximately 10 years of monitoring over 39 measurements. The median internal uncertainty for our observations is $\approx$ 5.9 $\mathrm{m\,s^{-1}}$, and the peak-to-peak velocity is $\approx$ 137.2 $\mathrm{m\,s^{-1}}$. The velocity scatter (standard deviation) around the average RV is $\approx$ 31.3 $\mathrm{m\,s^{-1}}$. For this star, our normal 2.7 m HJS telescope observations were supplemented with 10 data points obtained with Keck/HIRES. In addition to the 10 spectra taken with the iodine cell, we also observed a high S/N pure star template

---

[2] available at http://www.stefanom.org/systemic/

spectra with Keck. The precision of the HIRES RVs is superior to the HJST results, with a mean uncertainty of only $2.4\,\mathrm{m\,s^{-1}}$. We were also able to use the HIRES template to compute RVs from the HJST spectra and achieved a slightly better RV precision than using our HJST template, owing to the higher S/N of the Keck spectrum.

Table 3.2. Radial Velocity observations for HD 95872

	JD	RV ($\mathrm{m\,s^{-1}}$)	Uncertainty ($\mathrm{m\,s^{-1}}$)
1	2453073.87	66.24	5.33
2	2453463.78	98.52	5.91
3	2453843.77	109.16	5.87
4	2454557.76	63.50	6.65
5	2455286.71	-22.15	4.11
6[a]	2455366.78	15.53	1.92
7[a]	2455368.79	13.28	3.47
8	2455549.00	-8.50	4.60
9	2455583.90	-7.49	9.76
10	2455615.89	-4.40	5.37
11	2455632.79	-9.17	4.46
12	2455646.74	-25.82	5.86
13	2455667.75	-0.16	7.12
14	2455701.66	-10.18	4.45
15[a]	2455937.12	-2.35	3.48
16[a]	2455938.10	-2.30	2.68

Table 3.2 (cont'd)

	JD	RV ($\mathrm{m\,s^{-1}}$)	Uncertainty ($\mathrm{m\,s^{-1}}$)
17[a]	2455962.10	-4.15	1.66
18[a]	2455962.11	-1.15	2.59
19[a]	2455962.12	-6.69	2.14
20[a]	2455963.01	-5.43	1.54
21[a]	2455964.02	-2.21	2.35
22	2455964.88	-28.03	8.21
23[a]	2455965.04	-4.52	2.30
24	2455966.88	-8.26	5.55
25	2455968.87	-16.59	9.92
26	2455990.89	-9.42	6.18
27	2456017.77	-15.23	8.59
28	2456048.66	5.15	9.17
29	2456266.00	-20.73	7.64
30	2456370.79	9.35	5.93
31	2456402.69	0.00	7.54
32	2456671.95	19.07	6.47

Table 3.2 (cont'd)

	JD	RV ($\mathrm{m\,s^{-1}}$)	Uncertainty ($\mathrm{m\,s^{-1}}$)
33	2456700.87	21.31	7.91
34	2456730.77	7.99	5.11
35	2456744.65	17.91	6.07
36	2456756.71	5.78	6.81
37	2456786.65	20.58	6.63
38	2456788.68	22.00	5.98
39	2456815.62	10.63	4.66

[a] Observed with Keck/HIRES; all others with the HJS telescope

3.4.1.1 Companion Orbit Model

The top panel of Figure 3.1 shows the 39 individual RV measurements. The second panel shows the error-weighted, normalized Lomb-Scargle periodogram (82). The three horizontal lines in the plot represent different levels of false alarm probability (FAP; 10%, 1% and 0.1%, respectively). The FAPs were computed by scrambling the dataset 100,000 times, in order to determine the probability that the power at each frequency could be exceeded by chance (e.g. **?**). Computing the FAPs for this sparse dataset required scanning only frequencies that were effectively sampled by the set of observation times. We determined an "effective" Nyquist frequency for the dataset using the calculation formula of **?**). For irregularly spaced datasets, the effective Nyquist frequency is much higher than the corresponding Nyquist frequency of a regularly spaced dataset of the same size. The algorithm of **?**) finds a clear minimum at $P \approx 2$ days (fourth panel of Figure 3.1), corresponding to the effective Nyquist frequency for the data. Accordingly, we exclude periods shorter than 2 days from our calculations.

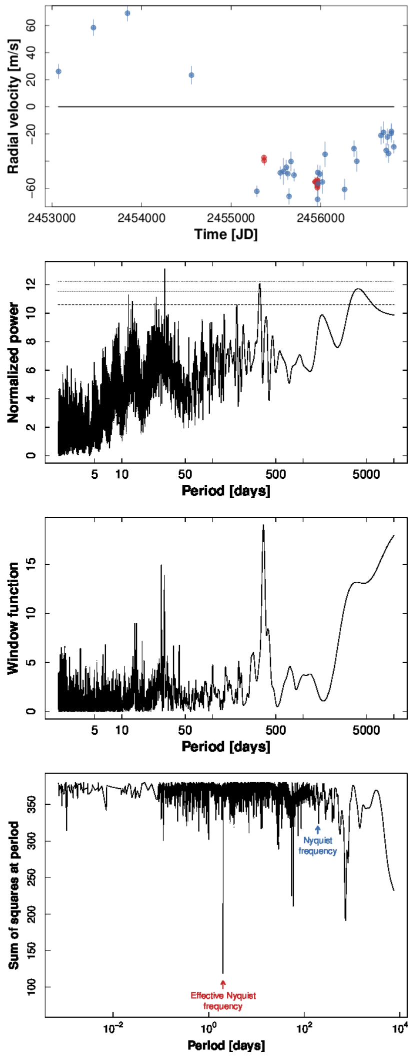

Figure 3.1 Radial velocity and Lomb-Scargle periodograms for HD 95872. *First panel:* Relative RV data. McDonald data is plotted in blue, while Keck data is plotted in red. *Second panel:* Error-weighted Lomb-Scargle periodogram for HD 95872. False-alarm probability levels are shown at the 10%, 1% and 0.1% level. *Third panel:* Periodogram of the window function. *Fourth panel:* Determination of the “effective” Nyquist frequency for the dataset. Both the effective Nyquist frequency, and the corresponding Nyquist frequency for a regularly spaced dataset are marked.

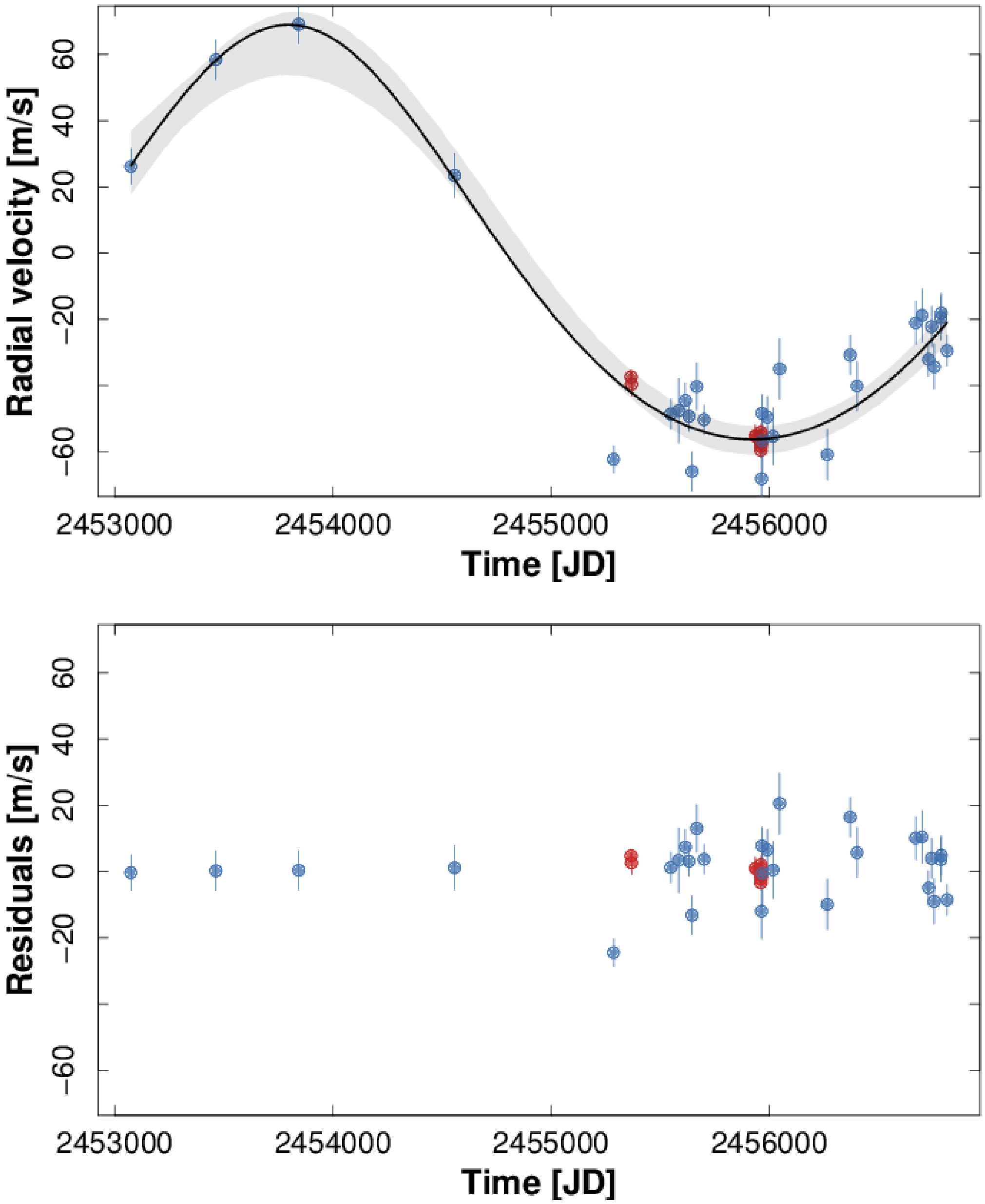

Figure 3.2 *Top panel:* Best-fit Keplerian model. The shaded area marks the 10%-90% percentiles of the radial velocity curves sampled from the MCMC trials, and indicates the range of the models compatible with the data. *Bottom panel:* Radial velocity residuals.

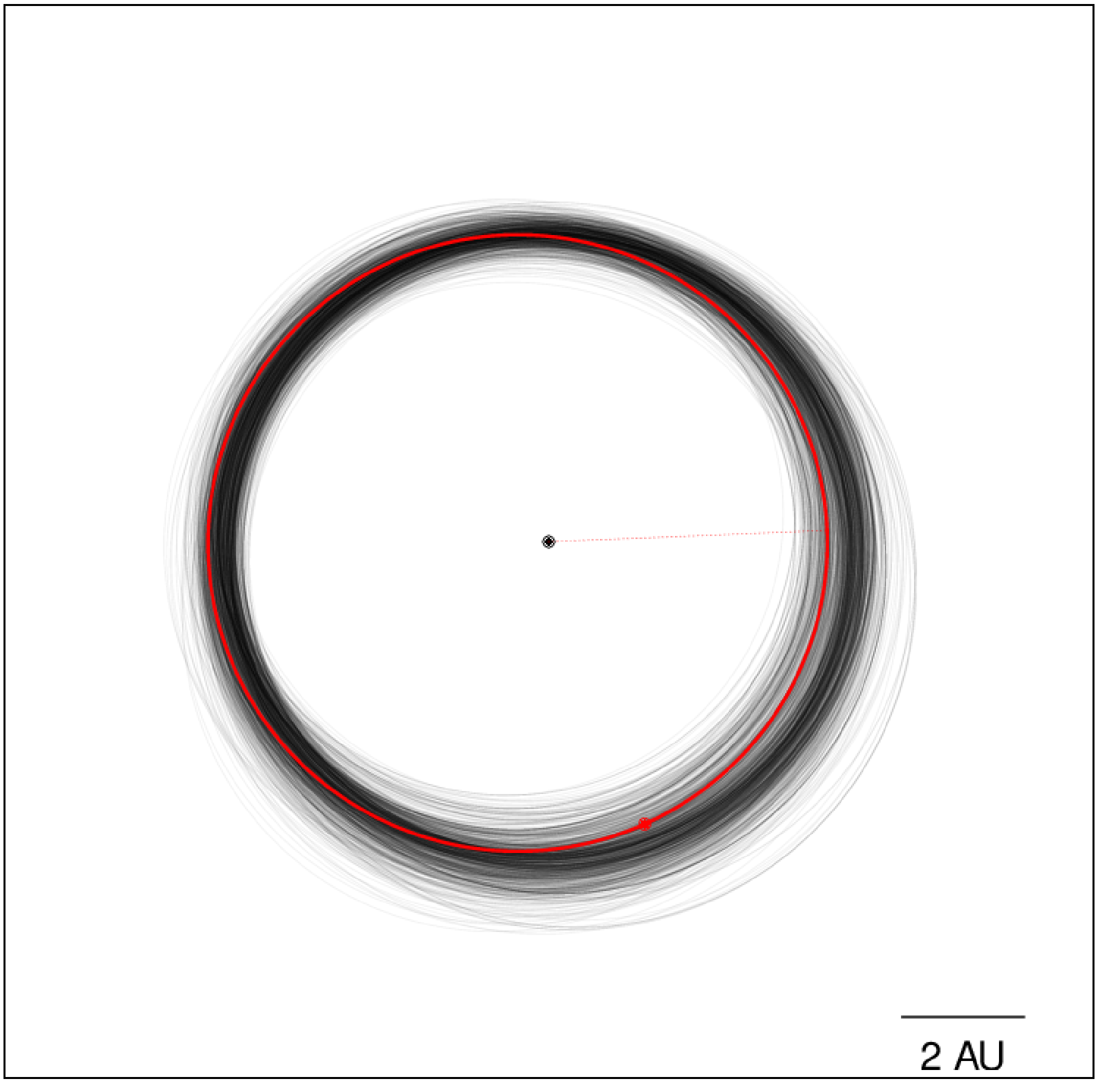

Figure 3.3 Orbital plot for the 1-planet model. Each orbit is sampled from the MCMC trials. The red line corresponds to the best-fit orbit and phase at epoch.

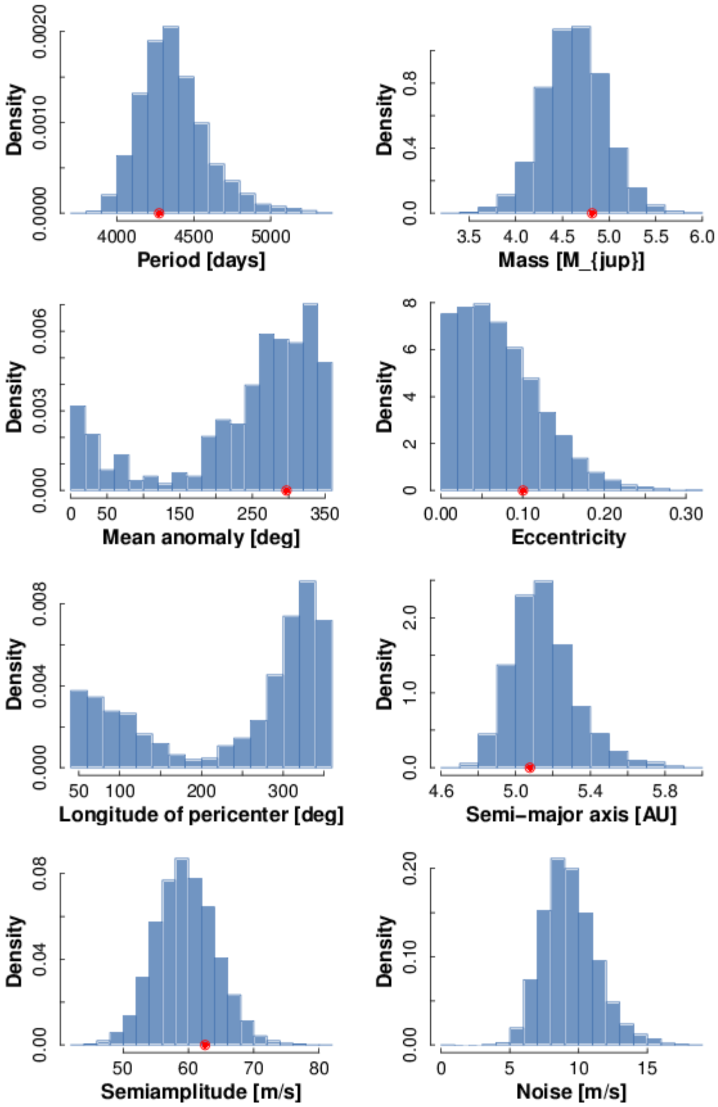

Figure 3.4 Marginal distributions of the orbital elements, as computed by the Markov-Chain Monte Carlo algorithm. The red dot marks the value of the best-fit solution.

Visual inspection of the data suggests the presence of a sparsely sampled, long-period signal. The Lomb-Scargle periodogram (Figure 3.1) bears this out. The two strongest signals, at $P = 29.6$ days (FAP $< 2.0 \times 10^{-5}$) and $P = 331.7$ days (FAP = 1.7×10^{-3}) have significant power in the window function, and they are likely related to the periodicities in the observational cadence (the lunar synodic month and the solar year). The remaining peak is at $P = 4000.5$ days (FAP = 5.5×10^{-3}). This signal is well fit with a Keplerian orbit of period $P = 4347 \pm 200$ days and semi-amplitude $K = 59 \pm 5$ $\mathrm{m\,s^{-1}}$(Figure 3.2). Together with the assumed stellar mass of 0.95 $\mathcal{M}_{\odot}$, this implies a minimum mass of $\mathcal{M} \sin i = 4.6 \pm 0.3 \mathcal{M}_J$ and a semi-major axis $a = 5.1 \pm 0.2$ AU. The best-fit orbit for the planet shows a small amount of eccentricity ($e = 0.06 \pm 0.05$, broadly consistent with circular). Orbital uncertainties were derived by running a Markov Chain Monte Carlo (MCMC) algorithm (Ford 2005) on the dataset. Non-informative priors were adopted over all parameters (uniform in logarithm for mass and period). A plot of 1,000 samples drawn from the output of the MCMC algorithm is shown in Figure 3.3, with the orbit corresponding to best-fit values shown in red. Marginal distributions of the parameters are shown in Figure 3.4; no significant correlations among parameters were observed. A summary of the astrocentric orbital elements of HD95872 b is reported in Table **??**.

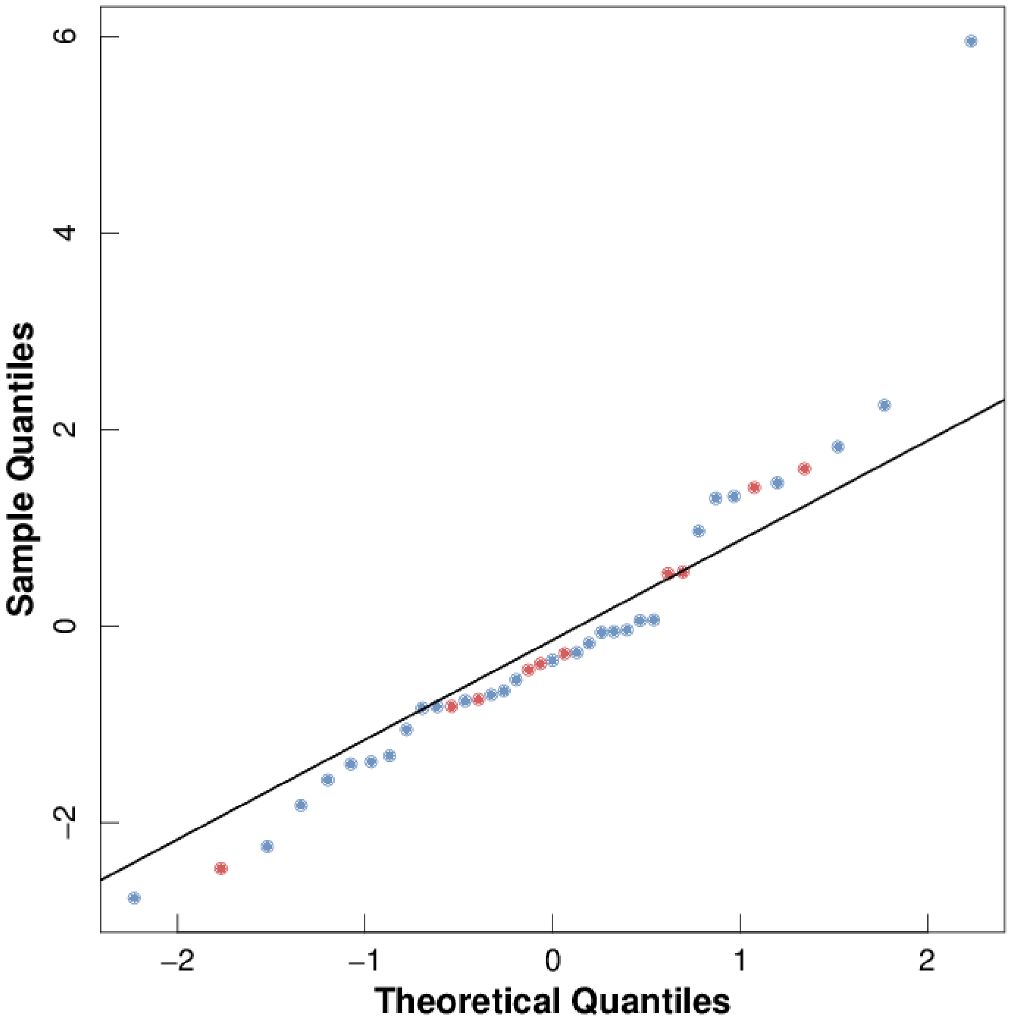

Figure 3.5 Quantile-quantile plot of the residuals from the 1-planet model. Perfectly normally distributed residuals would fall on the solid line.

The one-planet fit reduces the root mean square (RMS) of the data from 47.4 $\mathrm{m\,s^{-1}}$ to 8.7 $\mathrm{m\,s^{-1}}$. The stellar jitter for HD 95872 (that is, the required amount of uncertainty added in quadrature to the internal errors in order to completely fit the residuals) is $9 \pm 2\ \mathrm{m\,s^{-1}}$, and is derived self-consistently from the MCMC analysis. We note that the normalized residuals are very nearly normally distributed, aside from a single outlier (Figure 3.5).

As a final test to assess the quality of the fit, we use a cross-validation algorithm on the data, comparing a 1-planet model with a 0-planet model (where the only fit parameters are the relative shift between the Keck and McDonald datasets and a linear trend). In the "leave-one-out" flavor used for the present paper, we divide the full dataset of N observations into a *training set* of $N-1$ observations and a *testing set* of a single observation, rotated among all observations; each training set is used to derive a new fit. The combined likelihood of the prediction derived with this technique is sensitive to both underfitting and overfitting. In our case, we find that the 1-planet model significantly improves the test statistic over the 0-planets model ($\log \mathcal{L}_1 = -2.5$ vs. $\log \mathcal{L}_0 = 12.9$).

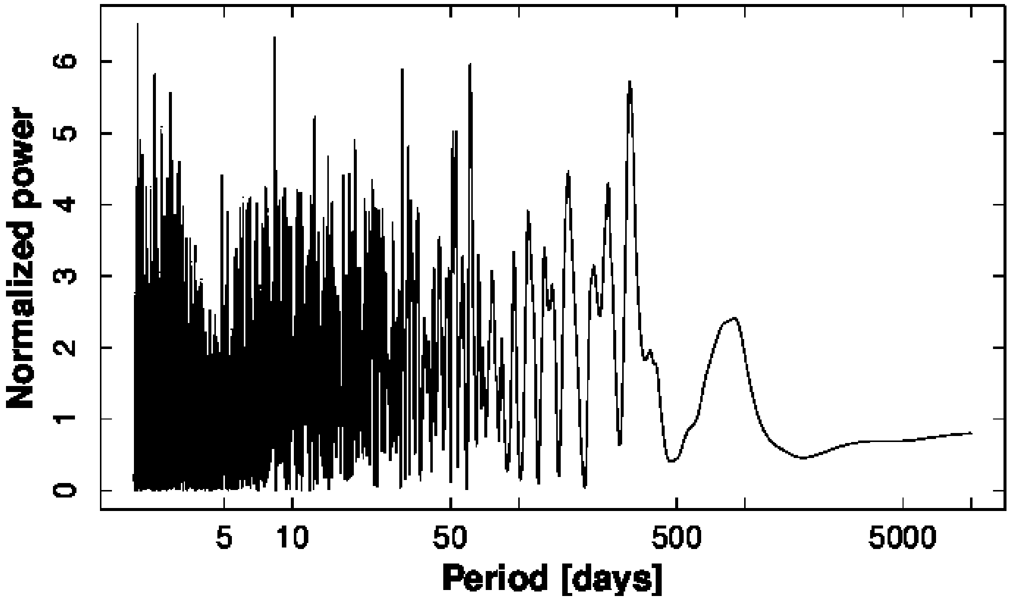

Figure 3.6 Lomb-Scargle periodogram of the residuals. No peaks are found above the FAP = 10% boundary.

Figure 3.6 shows the Lomb-Scargle periodogram of the RV residuals from the 1-planet best fit. There is no strong periodicity (FAP $<$ 10%) in the residuals supporting the presence of additional planets in the system.

	HD 95872 b
Period [days]	4347 [200]
Mass [$\mathcal{M}_{\text{jup}}$]	4.6 [0.3]
Mean anomaly [deg]	305 [61]
Eccentricity	0.06 [0.05]
Longitude of pericenter [deg]	353 [62]
Semiamplitude [m/s]	59 [5]
Semi-major axis [AU]	5.1 [0.2]
Periastron passage time [JD]	2449749 [740]
Noise parameter (McDonald) [m/s]	9 [2]
Noise parameter (KECK) [m/s]	0.5 [0.5]
Stellar mass [$\mathcal{M}_{\text{sun}}$]	0.95
RMS [m/s]	8.69
Jitter (best fit) [m/s]	6.40
Epoch [JD]	2453073.87 (04/09/2004)
Data points	39
Span of observations [JD]	2453073.87 (04/09/2004)
	2456815.62 (06/07/2014)

Table 3.3 Astrocentric orbital elements for HD 95872 b. For parameters derived from the MCMC analysis, we report their median values and their mean absolute deviation (in brackets).

3.4.1.2 Stellar Activity Check

The Ca H & K indices and line bisector velocity spans for this star show no correlation with our measured radial velocities.

3.4.2 ψ^1 Draconis System

The psi1 Draconis system is a visual binary composed of an F5 V primary (psi1 Dra A) and an F8 V secondary star (psi1 Dra B) separated by about 30.1 arcsec. At a distance of 22.2 pc, this corresponds to a sky-projected separation of approximately 667 AU. Previously, Toyota et al. (2008) reported evidence of an unseen companion orbiting the A component of the system, with a minimum mass of 50 M_J. We have monitored both stars for long-term RV variability and also find evidence for a stellar-mass companion around the A component, and two sub-stellar companions around the B component. Thus, the psi1 Draconis system is at least a heirarchical triple that hosts at least two candidate sub-stellar objects.

3.4.2.1 Direct Imaging

Both the A and B components of the psi1 Draconis system were separately observed with the Differential Speckle Survey Instrument (DSSI) at the Gemini North telescope on 19 July 2014 UT. DSSI is a two-channel speckle camera described in Horch et al. (2009), which yields diffraction-limited information in two pass bands simultaneously. A 1000-frame sequence was recorded by each channel on each component. All frames were

60 ms exposures, and had format of 256 × 256 pixels. The seeing for both observations was 0.65 arc seconds. The image scale is approximately 0.011 arcseconds per pixel for both cameras.

We reduced and analyzed the results as follows. We form the average autocorrelation and average triple correlation of the set of speckle frames, and from these we estimate both the magnitude and phase of the Fourier transform of the source. The former must be deconvolved by a point source observation in general; in the case of the data here, we constructed a point source matching the elevation and azimuth of the source by taking an observation of a point source at very high elevation and correcting it for the atmospheric dispersion expected for the elevation and azimuth of the science target. After the deconvolution, the magnitude and phase are assembled in the Fourier plane, low-pass filtered to suppress high-frequency noise, and inverse-transformed to arrive at a reconstructed (i.e. diffraction-limited) image of the target. More information about the reduction method with the current EMCCD cameras used with DSSI can be found in Horch et al. (2011).

With the reconstructed image in hand, we attempt to find companions by first examining the image. This yielded a strong stellar candidate at approximate separation of 0.16 arcseconds from the primary star for psi1 Dra A, but no candidates for psi1 Dra B. [Do I show these images? – not very informative, but maybe needed for referencing in subsequent text...]

We then also computed a detection limit curve for the image; that is, a curve showing the largest magnitude difference that could be detected as a function of separation from the central star in the image. To construct the curve, we choose a set of concentric annuli centered on the central star, and determine the statistics of the local maxima (peaks) occurring inside the annulus. If a peak in the annulus has a value of more than five times the sigma of all of the peaks above the average value of the peaks, we consider it to be a definitive detection of a stellar companion. Details of this process for Gemini data can be found in e.g. Horch et al. (2012).

We next used our power spectrum fitting routine to determine the separation, position angle, and magnitude difference of the secondary. The results are summarized in Table 3.4, when deconvolving by the calculated point sources described above:

filter (nm)	position angle (deg)	separation (arcsec)	magnitude difference (mag)
692	91.8	0.155	4.13
880	91.5	0.158	3.80

Table 3.4 Results of imaging for psi1 Dra A, using generic point source deconvolution

Since psi1 Dra B is not resolved in our images, we also used it as the point source to deconvolve the images of psi1 Dra A, and in doing the power spectrum fitting that way, we obtain the results summarized in Table 3.5.

filter (nm)	position angle (deg)	separation (arcsec)	magnitude difference (mag)
692	91.8	0.156	4.22
880	91.3	0.158	3.71

Table 3.5 Results of imaging for psi1 Dra A, using psi1 Dra B point source deconvolution.

The differences between these numbers and the above give a feel for the internal precision of the measurement technique. In looking at the power spectra for each file, we also see clear fringes that match the location shown in the reconstructed image. This gives an additional layer of confidence that we have detected a real stellar companion.

We note that this separation, at this distance, corresponds to a sky-projected separation of approximately 3.5 AU. This magnitude difference would make the companion a roughly M0 star.

3.4.2.2 A component

Table 3.6 presents the complete set of our RV observations for Psi1 Dra A. The RV coverage spans approximately 14 years of monitoring over 71 measurements. The median internal uncertainty for our observations is $\approx 9.7\ \mathrm{m\,s^{-1}}$, and the peak-to-peak velocity is $\approx 8749\ \mathrm{m\,s^{-1}}$. Our measurements are visually summarized in Figure 3.7. We see evidence of a close-in massive companion in an eccentric orbit.

Table 3.6. Radial Velocity observations for Psi1 Dra A

	JD	RV ($\mathrm{m\,s^{-1}}$)	Uncertainty ($\mathrm{m\,s^{-1}}$)
1	2451809.66	1922.73	10.99
2	2451809.674	1932.5	11.77
3	2452142.68	1848.05	6.21
4	2453319.639	2439.3	7.44
5	2453585.854	2558.43	12
6	2453585.875	2556.56	3.77
7	2453634.641	2647.22	7.73
8	2453635.624	2557.66	5.86
9	2453655.636	2706.32	2.83
10	2453655.642	2761.48	38.26
11	2453689.538	2660.54	6.86
12	2453907.849	2966.63	6.83
13	2453928.797	2856.7	5.67
14	2454019.603	2944.7	10.39
15	2454279.752	3073.95	9.09
16	2454279.757	3061.9	9.65

Table 3.6 (cont'd)

	JD	RV ($\mathrm{m\,s^{-1}}$)	Uncertainty ($\mathrm{m\,s^{-1}}$)
17	2454309.791	3036.39	8.44
18	2454345.63	3274.26	6.53
19	2454401.56	3161.6	8.29
20	2454662.927	3348.81	6.41
21	2454665.768	3497.42	4.48
22	2454665.772	3494.24	4.77
23	2454730.708	3446.28	10.53
24	2454750.637	3432.89	14.73
25	2454750.642	3414.13	8.3
26	2454750.646	3423.09	10.65
27	2454750.651	3417.82	12.68
28	2454750.656	3425.52	21.02
29	2454750.66	3413.92	10.97
30	2454750.671	3415.63	13.9
31	2454750.675	3411.31	20.07
32	2454750.68	3416.47	14.89

Table 3.6 (cont'd)

	JD	RV ($\mathrm{m\,s^{-1}}$)	Uncertainty ($\mathrm{m\,s^{-1}}$)
33	2455100.575	3860.43	20.23
34	2455100.579	3871.51	10.46
35	2455398.753	4207.3	6.25
36	2455790.722	4952.35	14.18
37	2455869.575	5210.72	4.93
38	2455910.565	5302.28	14.76
39	2455992.019	5545.85	4.01
40	2456016.925	5669.38	7.1
41	2456106.776	5795.34	6.45
42	2456138.837	5959.53	6.73
43	2456145.655	5949.55	9.09
44	2456145.658	5933.53	12.25
45	2456145.661	5946.07	3.89
46	2456173.731	5961.1	4.42
47	2456401.966	6962.55	9.22
48	2456401.969	6955.23	13.44

Table 3.6 (cont'd)

	JD	RV ($\mathrm{m\,s^{-1}}$)	Uncertainty ($\mathrm{m\,s^{-1}}$)
49	2456433.742	7233.4	7.38
50	2456433.744	7223.59	3.38
51	2456435.87	7222.44	5.75
52	2456435.872	7210.36	14.13
53	2456461.872	7358.05	11.4
54	2456461.875	7351.35	10.83
55	2456461.878	7348.7	6.68
56	2456465.805	7275.47	6.32
57	2456497.857	7582.3	14.77
58	2456519.616	7756.74	10.6
59	2456525.66	7722.62	5.41
60	2456560.583	7821.68	7.63
61	2456564.594	7807.76	11.32
62	2456613.552	8097.24	12.65
63	2456614.579	8140.56	12.94
64	2456755.984	9315.62	14.78

Table 3.6 (cont'd)

	JD	RV ($\mathrm{m\,s^{-1}}$)	Uncertainty ($\mathrm{m\,s^{-1}}$)
65	2456759.969	9388.21	12.61
66	2456784.838	9602.88	9.61
67	2456816.672	9913.72	11.55
68	2456816.674	9911	15.3
69	2456860.727	10397.26	11.96
70	2456860.729	10415.12	11.07
71	2456885.624	10597.11	13.56

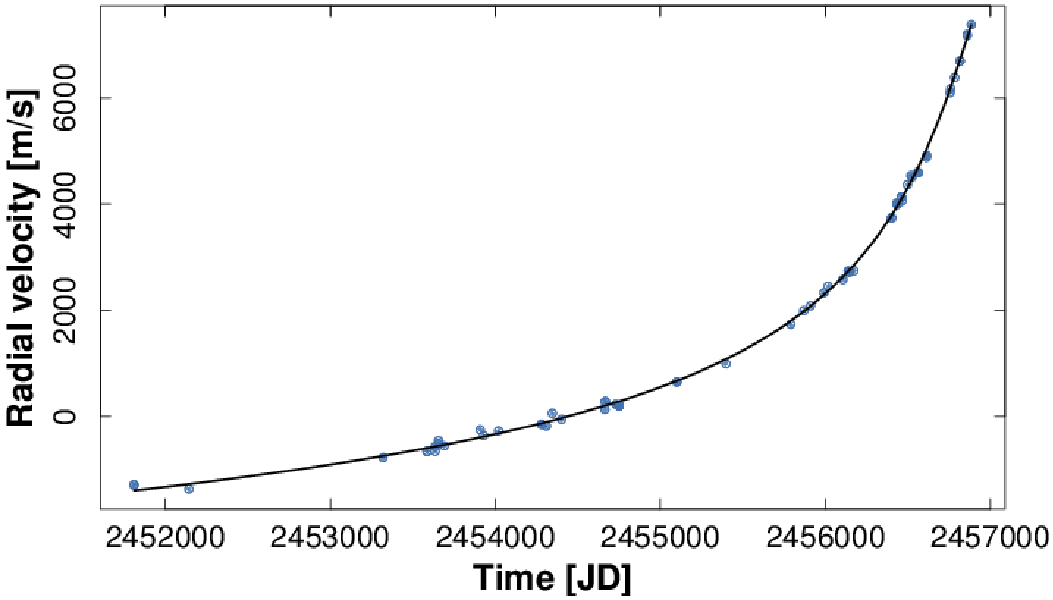

Figure 3.7 A plot of our measured radial velocities for psi1 Dra A, as a function of observation date. We see evidence of a massive companion in an eccentric orbit.

3.4.2.3 B component

Table 3.7 presents the complete set of our RV observations for Psi1 Dra B. The RV coverage spans approximately 16 years of monitoring over 112 measurements. The median internal uncertainty for our observations is $\approx 5.6\ \mathrm{m\,s^{-1}}$, and the peak-to-peak velocity is $\approx 61.6\ \mathrm{m\,s^{-1}}$. The velocity scatter around the average RV is $\approx 14.7\ \mathrm{m\,s^{-1}}$.

	JD	RV $(\mathrm{m\,s^{-1}})$	Uncertainty $(\mathrm{m\,s^{-1}})$
1	2451066.73	-48.83	6.13
2	2451121.61	-48.50	3.78
3	2451271.99	-39.10	7.28
4	2451329.86	-33.41	5.50
5	2451360.88	-39.06	4.22
6	2451417.78	-24.46	4.97
7	2451451.69	-24.87	6.06
8	2451504.58	-12.33	3.38
9	2451627.97	-11.25	4.94
10	2451686.86	-20.18	1.07
11	2451753.69	-15.18	6.04
12	2451777.75	-1.06	4.37
13	2451862.53	-0.39	4.29
14	2452037.93	0.93	4.37
15	2452115.77	7.42	6.55
16	2452145.76	6.66	4.72
17	2452181.66	7.72	3.96
18	2452454.83	7.85	4.96
19	2452471.78	-5.10	3.94
20	2452495.69	0.91	4.03

Table 3.7 Radial Velocity observations for Psi1 Dra B (sample)

3.4.2.4 Companion Orbit Models

The relative radial velocity data for Psi1 Dra B is plotted in Figure 3.8. The Lomb-Scargle periodogram (Figure 3.8) for the unreduced data shows two strong peaks at $P_1 \approx 2381$ days and $P_2 > 6000$ days (longer than the time span of our observations). We model the second signal with two parameters representing a linear and a quadratic term (evaluated at the epoch of the fit).

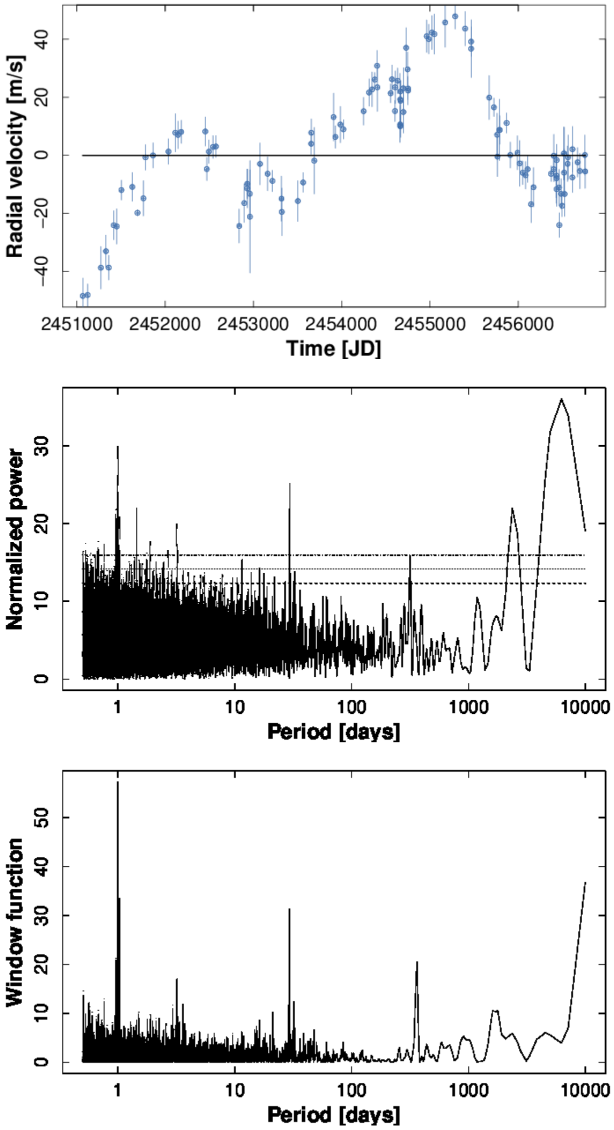

Figure 3.8 Radial velocity and Lomb-Scargle periodograms for Psi1 Dra B. *Top panel:* Relative RV data. *Middle panel:* Error-weighted Lomb-Scargle periodogram for Psi1 Dra B. False-alarm probability levels are shown at the 10%, 1% and 0.1% level. *Bottom panel:* Periodogram of the window function.

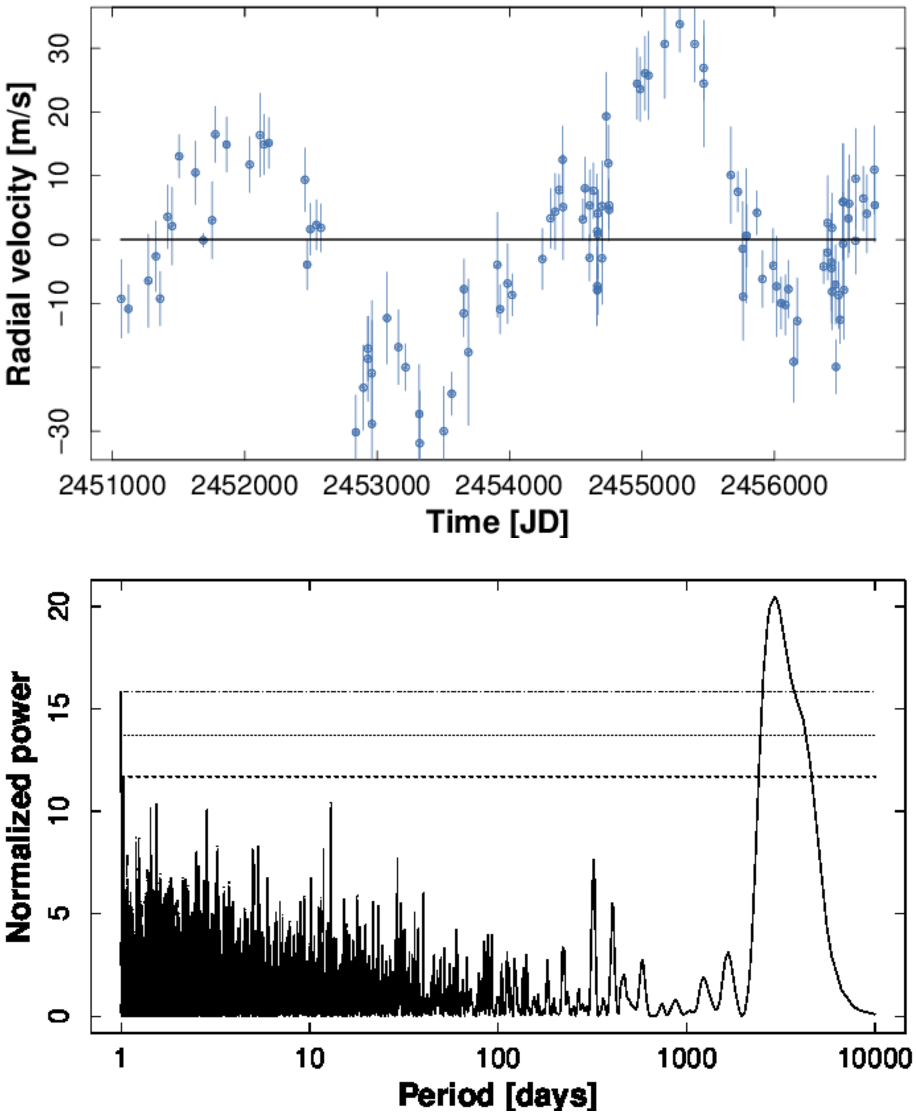

Figure 3.9 Radial velocity and Lomb-Scargle periodograms for Psi1 Dra B, with the linear and quadratic trends removed. *Top panel:* Relative RV data. *Middle panel:* Error-weighted Lomb-Scargle periodogram for Psi1 Dra B. False-alarm probability levels are shown at the 10%, 1% and 0.1% level.

Once the linear and quadratic trend terms are removed (Figure 3.9), a strong periodicity arises at $P \approx 3030$ days. The bootstrapped FAP probability is very low ($FAP < 2 \times 10^{-5}$). We fit this periodicity with a model that simultaneously minimizes the linear and quadratic trend terms and the five orbital elements describing an eccentric orbit (period, mass, mean anomaly, eccentricity and longitude of periastron). The best-fit model is show in Figure 3.10. The data is well modeled by a Keplerian orbit of period $P = 3122 \pm 40$ days and semi-amplitude $K = 21 \pm 1 \text{ m s}^{-1}$ (Figure 3.2). Together with the assumed stellar mass of 1.19 $\mathcal{M}_{\odot}$, this implies a minimum mass of $\mathcal{M} \sin i = 1.53 \pm 0.10 \mathcal{M}_J$ and a semi-major axis $a = 4.43 \pm 0.04$ AU. No compelling peaks are evident in the periodogram of the residuals.

The data strongly favors a substantial eccentricity for Psi1 Dra B b ($e = 0.39 \pm 0.05$). The cross-validation algorithm corroborates the clear preference for an eccentric model ($\log \mathcal{L}_{circular} \approx 0.02$ vs. $\log \mathcal{L}_{eccentric} \approx -21.3$; lower is better).

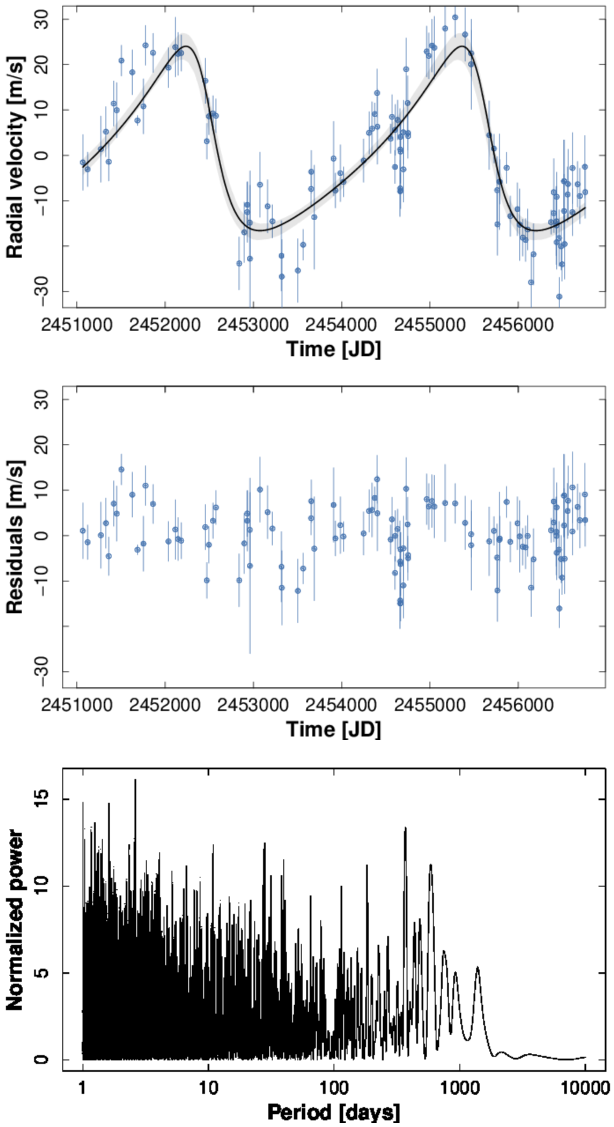

Figure 3.10 Best 1-planet fit of the RV dataset for Psi1 Dra B. *Top:* Radial velocity observations (linear and quadratic term subtracted) and 1-planet best fit. The shaded area marks the 10%-90% percentiles of the radial velocity curves sampled from the MCMC trials, and indicates the range of the models compatible with the data. *Middle:* Residuals from the 1-planet best fit. *Bottom:* Periodogram of the residuals from the 1-planet best fit.

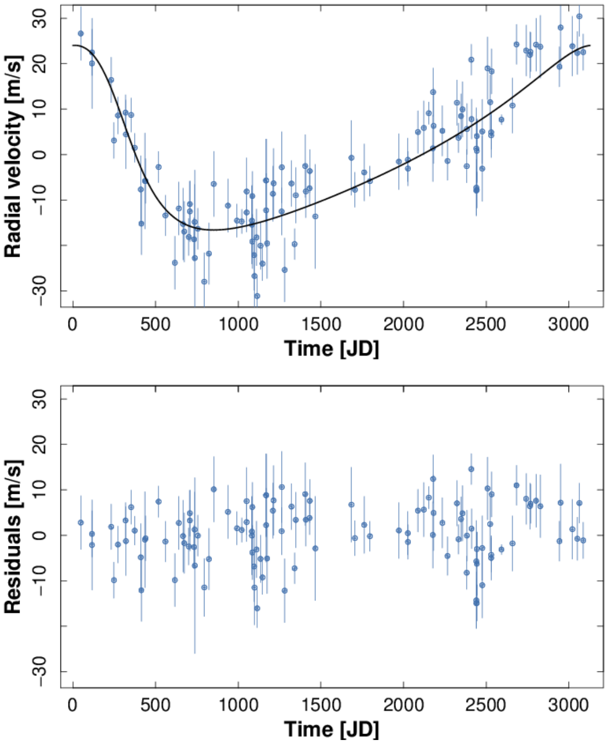

Figure 3.11 Phased best 1-planet fit of the RV dataset for Psi1 Dra B. *Top:* Radial velocity observations (linear and quadratic term subtracted) and 1-planet best fit. *Bottom:* Residuals from the 1-planet best fit.

The distribution of the orbital elements is shown in Figure 3.10, while an orbital plot is shown in Figure 3.13. There is no strong correlation between any of the parameters of the fit, including between the trend parameters and the semi-amplitude of the planet (bottom row). The derived stellar jitter is $4.5 \pm 0.7\,\mathrm{m\,s^{-1}}$. The distribution of the residuals shows no evidence for unmodeled periodicities in the data. Indeed, we note that the normalized residuals are again very nearly normally distributed (Figure 3.14).

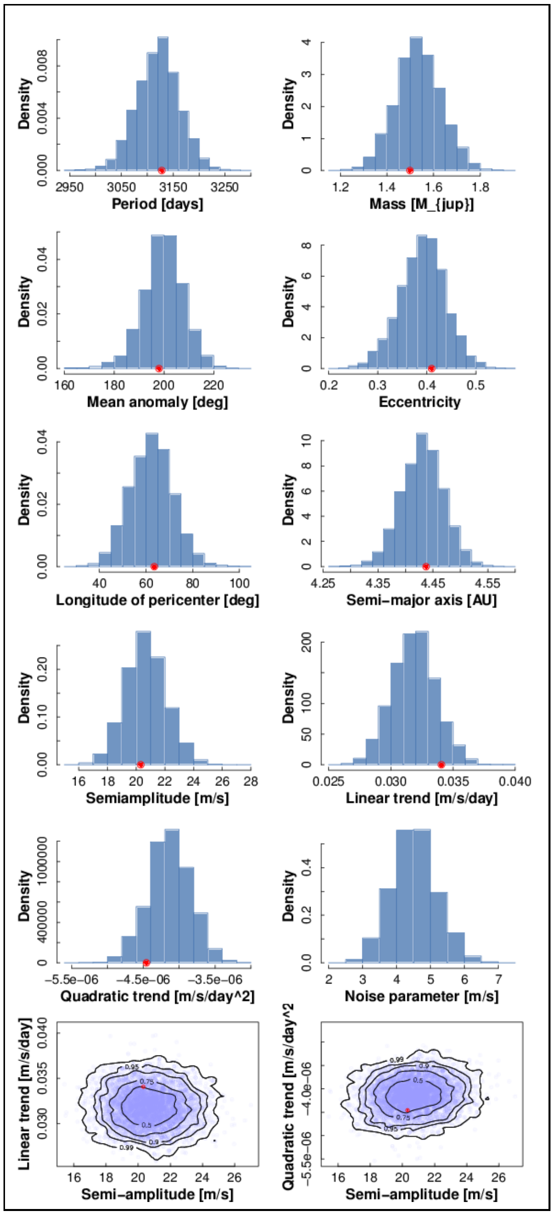

Figure 3.12 Marginal distributions of the orbital elements for the 1-planet model, as computed by the Markov-Chain Monte Carlo algorithm. The red dot marks the value of the best-fit solution. The bottom row shows a contour plot of the planet semi-amplitude K versus the linear and quadratic trend parameters.

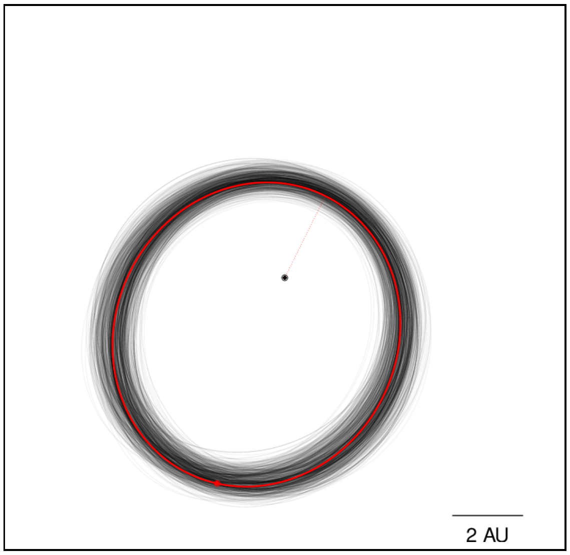

Figure 3.13 Orbital plot for the 1-planet model. Each orbit is sampled from the MCMC trials. The red line corresponds to the best-fit orbit and phase at epoch.

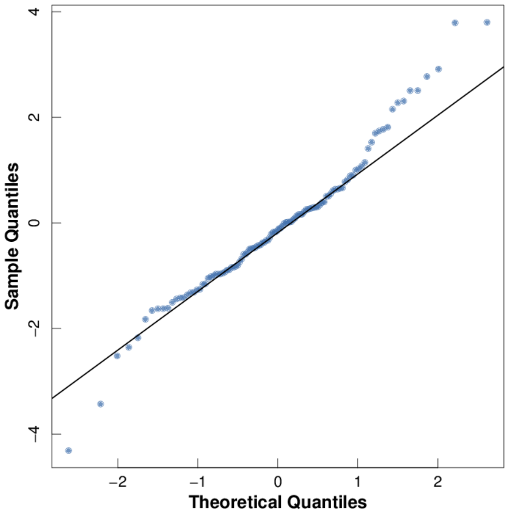

Figure 3.14 Quantile-quantile plot of the residuals from the 1-planet model. Perfectly normally distributed residuals would fall on the solid line.

	Psi Dra Bb
Period [days]	3122 [40]
Mass [$\mathcal{M}_{\text{jup}}$]	1.53 [0.10]
Mean anomaly [deg]	200 [8]
Eccentricity	0.39 [0.05]
Longitude of pericenter [deg]	62 [9]
Semiamplitude [m/s]	21 [1]
Semi-major axis [AU]	4.43 [0.04]
Periastron passage time [JD]	2449332 [78]
Noise parameter [m/s]	4.5 [0.7]
Quadratic trend [$\mathrm{m/s}^2$]	-0.0000041 [0.0000003]
Linear trend [m/s]	0.032 [0.002]
Stellar mass [$\mathcal{M}_{\text{sun}}$]	1.19
RMS [m/s]	6.50
Jitter (best fit) [m/s]	1.84
Epoch [JD]	2451066.73 (09/10/1998)
Data points	112
Span of observations [JD]	2451066.73 (09/10/1998)
	2456759.96 (04/12/2014)
$\log \mathcal{L}$ [0 planets]	23.6
$\log \mathcal{L}$ [0 planets, l+q trend]	13.7
$\log \mathcal{L}$ [1 circular planet, l+q trend]	0.02
$\log \mathcal{L}$ [1 eccentric planet, l+q trend]	-21.3

Table 3.8 Astrocentric orbital elements for Psi Dra Bb. For parameters derived from the MCMC analysis, we report their median values and their mean absolute deviation (in brackets).

Origin of the trend

In this Section, we investigate the nature of the long-term trend observed in the data. In particular, we ascertain whether Psi Dra A ($a \approx 600$ AU, $\mathcal{M}_A \approx 1.38\mathcal{M}_\odot$, $P \approx 9.4 \times 10^4$ years) is the source of the long-term trend.

To model the long-term trend, we first assume that the gravitational pull is provided by an external perturber (Psi1 Dra c) in a circular orbit. We fit the data by fixing the eccentricity of the perturber to zero and sampling periods between 4,000 days and 15,000 years. The top panel of Figure 3.15 shows the best-fit for the mass of the perturber at each period sampled. The goodness of the fit (as measured by the RMS of the residuals) is shown in the bottom panel. Beyond approximately 10^4 days, the RMS is flat and the period and mass of the perturber are degenerate. We note that A cannot be the source of the long-term trend, given the minimum mass required for A at the observed binary separation.

If we relax the assumption of a circular orbit for the external perturber, then the predicted mass of the perturber at each orbital period will be smaller at higher eccentricities (Figure 3.16). This is because at higher eccentricities and fixed periods, the curvature of the RV signal will be provided at the pericenter swing of the perturber. Therefore, the mass of the outer companion is determined by the pericenter distance ($q = a(1-e)$; Figure 3.16, bottom panel), as expected. Again, A is not close or massive enough to produce the observed curvature.

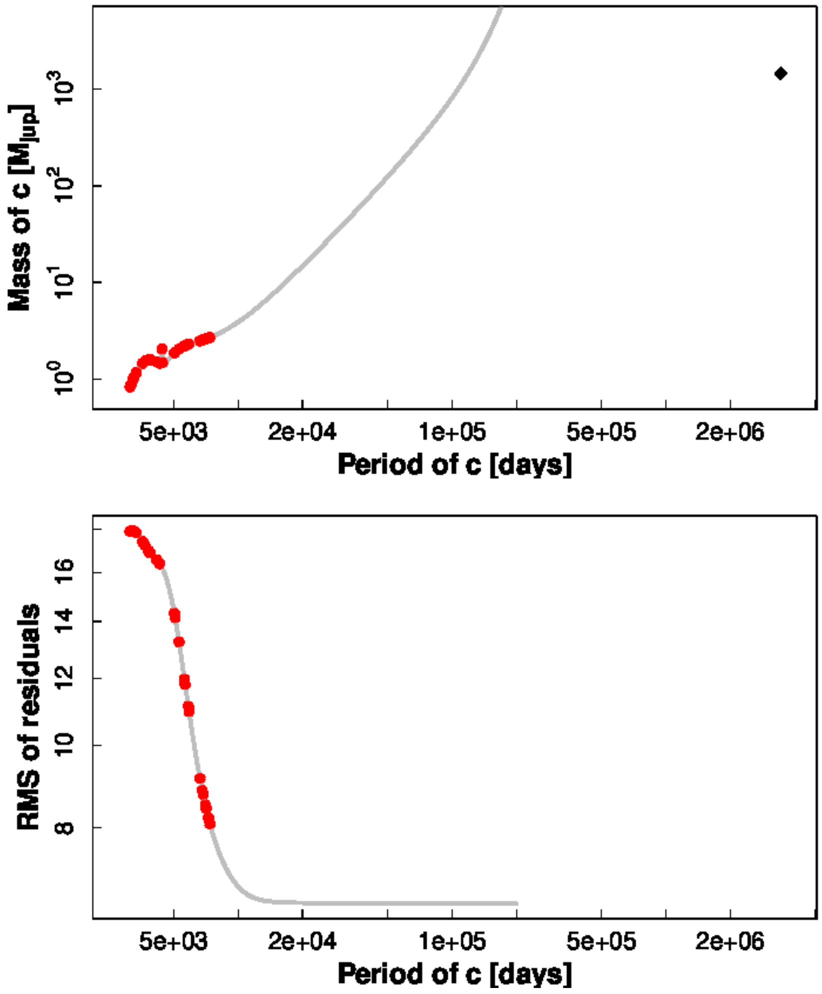

Figure 3.15 *Top:* Correlation between the period and the mass of an outer body in a circular orbit that best fits the trend in the RV data. The red points correspond to systems that were unstable over a 10^6 years period. The black diamond marks the semi-major axis and mass of Psi Dra A from **?**). *Bottom:* RMS of the residuals for the best-fit at each orbital period of the outer companion. At periods larger than $\approx 10^4$ days, the marginal distributions of the period and mass of the outer companion are flat.

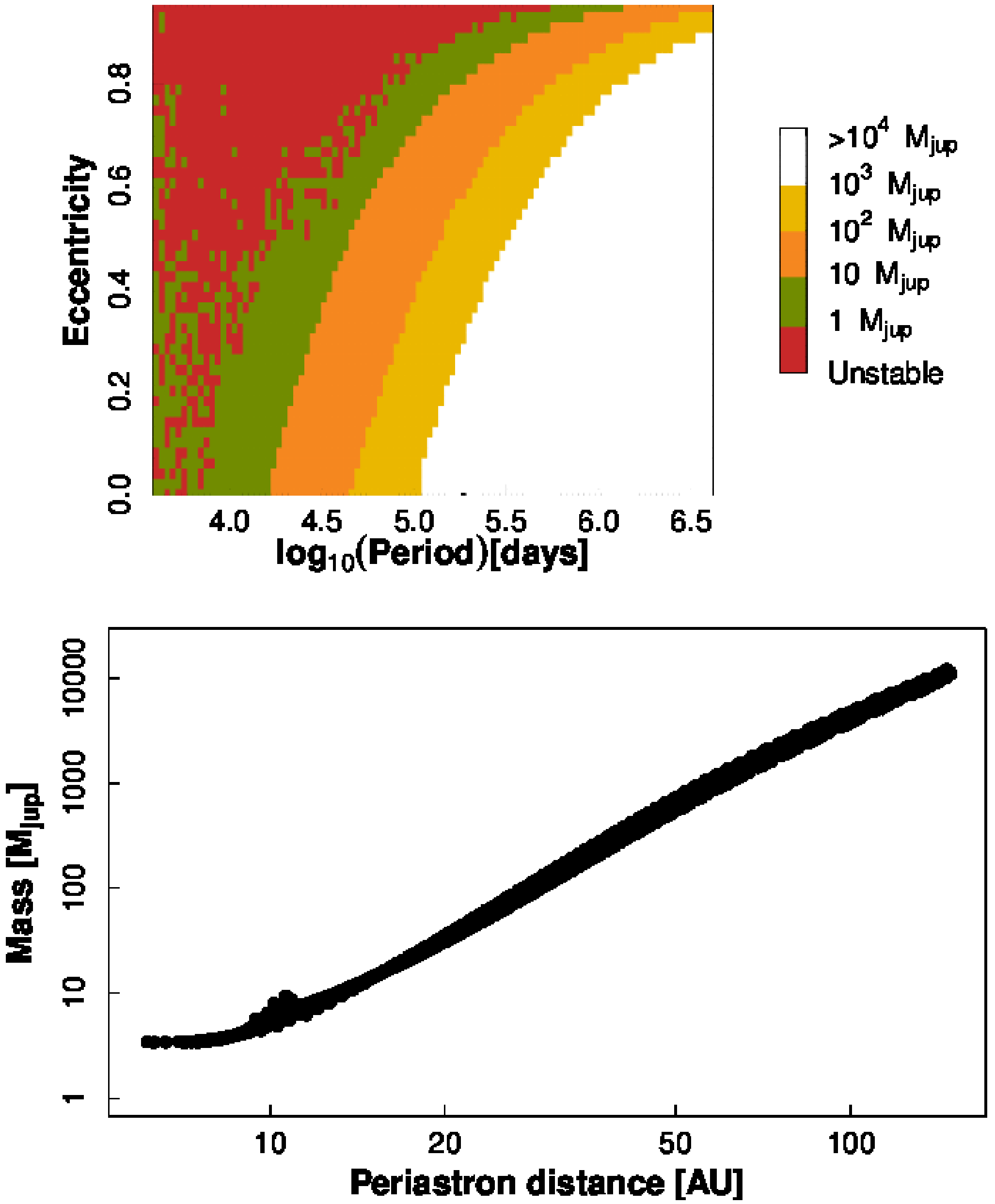

Figure 3.16 *Top:* Contours of best-fit masses for the outer perturber, computed over a grid of fixed periods and eccentricities. Systems unstable within 10^5 years are marked in red. *Bottom:* Relationship between the periastron distance and the mass of the outer perturber.

3.4.2.5 Stellar Activity Check

The Ca H & K indices and line bisector velocity spans for this star show no correlation with our measured radial velocities.

3.4.2.6 Dynamical Stability Analysis

A number of recent studies have highlighted the value of examining the dynamical behaviour of candidate planetary systems as a critical part of the planet discovery process (e.g. Horner et al. 2012a,b; Robertson et al. 2012a,b; Wittenmyer et al. 2012a, 2014a). We therefore chose to carry out a detailed dynamical study of the stability of the proposed ψ^1 Dra B system, as a function of the orbit of the newly discovered planet. As in our earlier work, we carried out a total of 126075 individual simulations of the ψ^1 Dra B planetary system, following the evolution of the two candidate planets for a period of 100 Myr using the Hybrid integration package within the n-body dynamics program MERCURY (Chambers, 1999). For these simulations, we have ignored the binary companion ψ^1 Dra A – with a projected orbital separation of $\sim$600 AU, it is expected to have a negligable effect on the dynamics of the two planets considered here. In the case that one of the planets collided with the other, or was either flung into the central body or ejected from the system, the time at which that event occurred within the simulation was recorded, and the simulation was then terminated. This allowed us to create a map of the dynamical stability of the ψ^1 Dra B system as a function of the initial semi-major axis and eccentricity of the outermost planet, as can be seen in Figure 3.17

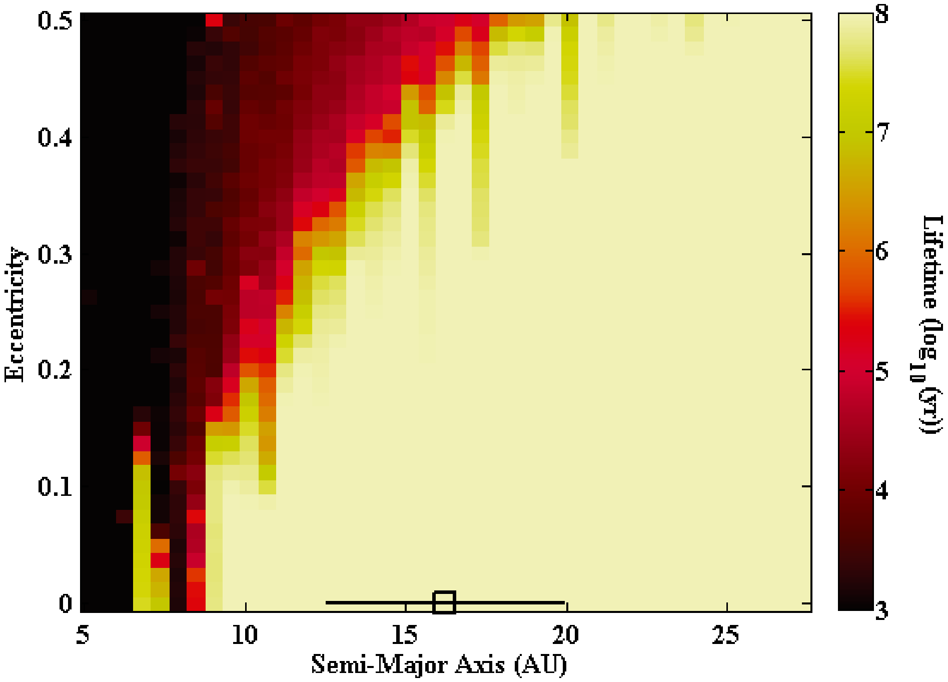

Figure 3.17 Lifetime as a function of eccentricity and orbital separation for the outer companion to psi1 Dra B. The best-fit orbit is indicated with a square box, and lies in a stable region with a lifetime of order Gyr.

In each of our 126075 simulations, we used the same initial conditions for the orbit of the innermost planet, as given in Table 3.7. For ψ^1 Dra B c, we systematically varied the semi-major axis, eccentricity, argument of periastron (ω) and mean anomaly (M) to create a grid of 41x41x15x5 possible orbital solutions for that planet. In the case of the planet's semi-major axis, ω, and mean anomaly, we sampled the full $\pm 3\sigma$ range around the nominal best fit values for each parameter. For the eccentricity, we sampled 41 equally spaced values ranging between 0.0 and 0.5. This allowed us to investigate in some depth the influence that the eccentricity of the planet's orbit will have on the system's stability.

The results of our simulations can be seen in Figure 3.17. At each of the a-e locations in that figure, the lifetime given is the mean of 75 individual runs at that a-e location, sampling the full $\omega - M$ parameter space. Most readily apparent in Figure 3.17 is that the nominal best-fit orbit is located in a broad region of orbital stability. Indeed, all solutions within $\pm 1\sigma$ of the best-fit semi-major axis are dynamically stable, unless the initial orbital eccentricity is in excess of 0.2. This is not surprising: the relatively sharp delineation between stable and unstable orbits that can be seen curving upwards from an origin at ($a \sim 9, e \sim 0$) is a line of almost constant periastron distance, and separates those orbits on which the planets cannot experience close encounters from those on which they can (and do). Following Chambers et al. (6), we can determine the mutual Hill radius of the two companions at various semi-major axes (using their equation 1). Doing this, we note that when ψ^1 Dra B c is located at $a = 9$ AU, the mutual Hill radius of the two companions is ~1.02 AU, meaning that their orbits would be separated by less than 5 mutual Hill radii. More critically, however, this situation would allow the two companions to approach one another within two mutual Hill radii should a close encounter happen whilst ψ^1 Dra B b (with its moderately large orbital eccentricity of 0.42) were close to apastron.

A few other noteworthy features can be readily observed in Figure 3.17. Interior to the broad area of stability lies a narrow island of stability at a ~7 AU. Orbits in this region can be protected from destabilisation by the influence of the mutual 2:1 mean-motion resonance between the two companions. Given an initial semi-major axis for ψ^1 Dra B b of 4.31, a perfect 2:1 commensurability between the orbits of the two planets would occur at $a_c \sim$ 6.84 AU, so long as the initial architecture of the system is appropriate, and the eccentricity of the orbit of ψ^1 Dra B c is not too large. Such islands of resonant stability are not uncommon, and are thought to ensure the stability of several known exoplanetary systems (77, 79, e.g.).

Finally, a number of "bites" can be seen taken out of the broad region of stability – vertical strips of lower-than-average stability dotted at regular intervals through the whole range of semi-major axes examined (with the most prominent visible at a ~11 AU). These represent locations where resonant interactions between the two companions act to destabilise, rather than stabilise, their orbits. These features serve as a reminder that even when two planets are well separated in their orbits around a given star, their orbits should still be checked for dynamical verisimilitude.

3.4.2.7 Comparison of Elemental Abundances

Planet signatures in stellar abundances

An independent stellar parameter and detailed (multi-element) chemical composition analysis for both stars in the psi1 Draconis system was carried out in order to search for chemical abundance anomalies that could be related to planet formation processes, as suggested by a number of recent studies. In their highly precise spectroscopic studies of solar twin stars, (**?**) and (51) have found the Sun to be slightly deficient in refractory elements, attributing this observation to the formation of rocky bodies in the solar system. They suggest that these objects captured the refractory elements that would have otherwise ended up in the Sun. In related work, (53) and (68) have found that the two solar-analog components of the 16 Cygni binary system have slightly different overall metallicities and have attributed this effect to the formation of the gas giant planet that orbits 16 Cygni B (9).

The rocky planet formation hypothesis for the refractory element depletion seen in the Sun has been challenged by (21, 22) while (64) have found no chemical abundance differences for the 16 Cygni stars. Thus, further investigation of other relevant stellar systems could shed light on this problem. The psi1 Draconis system is an interesting target in this context. Although not similar to the Sun, these stars are similar to each other, which is favorable to high-precision relative chemical composition analysis. Our psi1 Dra A spectrum is contaminated by that of its M-dwarf companion at the 1 % level. Although we expect a small error in our measurements to be introduced by this spectroscopically-unresolved star, it does not compromise our analysis, which assumes that each spectrum corresponds to an individual star.

Atmospheric parameter determination

We acquired very high signal-to-noise ratio spectra of the psi1 Draconis stars with the Tull spectrograph on the 2.7 m Telescope at McDonald Observatory on April 21st, 2014. At 6 000 Å, these spectra have $S/N \simeq 500$ per pixel and a spectral resolution $R = 60\,000$. These spectra are not part of the RV planet search dataset; they were acquired specifically for the purpose of carrying out a detailed, strict differential atmospheric parameter and chemical abundance analysis. As described below, we analyzed psi1 Dra A relative to psi1 Dra B, but we also tested our differential calculations using a solar spectrum as reference. The latter was taken from a previous observing run (December 18th, 2013) in which reflected sunlight from the asteroid Vesta was used to collect a high signal-to-noise ratio ($S/N \simeq 350$ at 6 000 Å) solar spectrum with the same instrument/telescope and identical configuration.

Equivalent widths of 73 Fe I lines and 18 Fe II lines were measured by fitting Gaussian profiles to the observed spectral lines in the psi1 Draconis stars' and solar spectra using the `splot` task in IRAF. The linelist and atomic parameters adopted are those by (54). The uncertainty of the adopted $\log gf$ values and whether those were taken from laboratory measurements or calibrated using reference spectra (i.e., "astrophysical" values) are irrelevant in the strict differential approach implemented here. As mentioned above, the psi1 Dra A spectrum is contaminated at the 1 % level by its M-dwarf companion. We noticed this minor contamination in our spectra and attempted to remove it in our equivalent width measurements by using the "deblend" feature of `splot` whenever possible or by excluding sections of line wings in the line profile fits. Nevertheless, we expect the equivalent widths measured for psi1 Dra A to be less precise than those of psi1 Dra B, not only due to the M-dwarf companion contamination, but also because of its somewhat faster projected rotational velocity.

The equivalent widths of each of the psi1 Draconis stars and the Sun were employed to calculate iron abundances using the `abfind` driver of the MOOG spectrum synthesis code, adopting Kurucz's `odfnew` grid of model atmospheres interpolated linearly to the assumed atmospheric parameters of each star. Then, on a line-by-line basis, differential iron abundances relative to the Sun were computed for the psi1 Draconis stars. The stellar parameters of the psi1 Draconis stars were modified iteratively until correlations of the iron abundance with excitation potential and reduced equivalent width disappeared and until the mean abundance of iron derived from Fe I and Fe II lines separately agreed. This procedure is standard in stellar spectroscopy and it is sometimes referred to as the excitation/ionization equilibrium method of stellar parameter determination. To be more specific, hereafter we refer to this technique as the "iron line only" method. The particular implementation used here, including the error analysis, is described in detail in Ramírez et al. (55, their Sect. 3.1 and references therein).

Table 3.9 Atmospheric Parameters of the psi1 Draconis Stars

Component	$T_{\rm eff}$	$\log g$	[Fe/H][3]	Reference
A	6546 ± 56	3.90 ± 0.14	-0.10 ± 0.04 (± 0.07)	Sun
B	6213 ± 20	4.35 ± 0.05	$+0.00 \pm 0.01$ (± 0.04)	Sun
A	6544 ± 42	3.90 ± 0.11	-0.10 ± 0.03 (± 0.05)	B

[1] The error bars in parenthesis correspond to the $1\,\sigma$ line-to-line scatter.

The atmospheric parameters of the psi1 Draconis stars, derived as described above, are given in the first two rows of Table 3.9. The errors listed in that table are formal, i.e., they represent the precision with which we are able to find a self-consistent solution for the parameters, but do not take into account possible systematic errors. The psi1 Draconis stars are both significantly warmer than the Sun. Thus, we expect the analysis using the solar spectrum as reference to be affected by systematic errors in a non-negligible way. Since we are interested in the relative elemental abundances of the two psi1 Draconis stars, we could attempt to reduce these formal errors, and also minimize the potential systematics, by analyzing psi1 Dra A using psi1 Dra B as the reference star. Adopting the parameters derived for psi1 Dra B using the Sun as reference (row 2 in Table 3.9), we computed the parameters of psi1 Dra A given in row 3 of Table 3.9. Note that the formal errors reduced, but the average values of the parameters were not significantly affected. This proves that, when using the Sun as reference, systematic errors are introducing line-to-line scatter to the iron abundances of the psi1 Draconis stars.

In the last step we implicitly assumed that the parameters of psi1 Dra B derived using the Sun as reference are reliable. We tested this assumption by computing those parameters using independent techniques. For T_{eff}, we employed the effective temperature – color calibrations by (5). For $\log g$, we used the stars' trigonometric parallaxes as given in the *Hipparcos* catalog along with the Yonsei-Yale theoretical isochrone grid. Details on these techniques and the implementation used here are also provided in Ramírez et al. (55, their Sects. 5.1 and 5.3 and references therein).

Using the $[\mathrm{Fe/H}]$ values from Table 3.9, the (5) T_{eff} calibrations for the $(B-V)$, $(b-y)$, and $(B_{\mathrm{T}}-V_{\mathrm{T}})$ colors provide mean values of 6519 ± 20 K for psi1 Dra A and 6194 ± 21 K for psi1 Dra B. Both these values are in agreement within formal error with those computed from the iron lines only (i.e., with the parameters given in Table 3.9). Moreover, their difference is 325 K according to the T_{eff}-color calibrations and 333 K according to the iron line analysis. This test confirms that the T_{eff} adopted for psi1 Dra B in the strict differential analysis for psi1 Dra A is reliable.

The trigonometric $\log g$ values were computed using the T_{eff} from the color calibrations, thus making them completely independent of the iron line only analysis. We calculated $\log g = 4.02 \pm 0.02$ for psi1 Dra A and $\log g = 4.32 \pm 0.02$ for psi1 Dra B. The spectroscopic (iron line only) $\log g$ of psi1 Dra A appears slightly low, yet it is still in marginal agreement with the trigonometric value within formal error. However, for psi1 Dra B, the agreement is excellent, which also suggests that the $\log g$ adopted for psi1 Dra B in the strict differential analysis of psi1 Dra A is reliable.

Multi-element abundance analysis

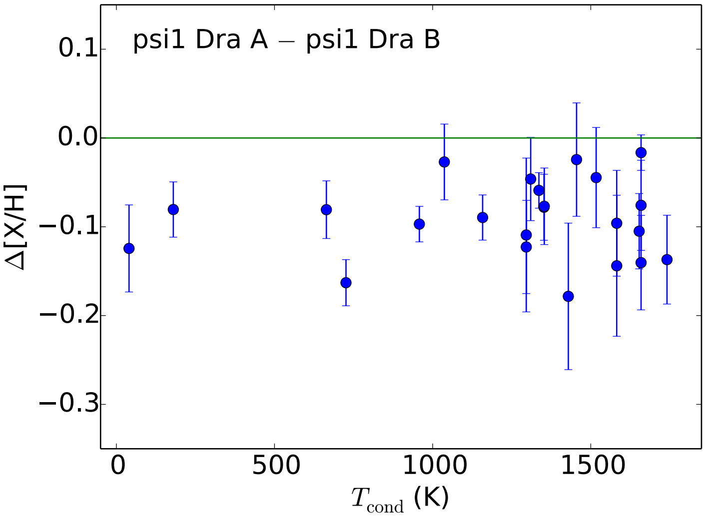

Figure 3.18 Elemental abundance difference between psi1 Dra A and psi1 Dra B as a function of the elements' condensation temperatures.

Equivalent widths of spectral lines due to species other than iron were measured to compute differential abundances of 20 chemical elements in the psi1 Draconis stars. The linelist and adopted atomic data, including hyperfine structure parameters when available, are from (51, 53). Oxygen abundances were inferred using the O I triplet lines at 777 nm, corrected for non-LTE effects using the grid by (50).

The relative elemental abundances we measured are plotted in Figure 3.18 as a function of the elements' 50 % condensation temperatures, as computed by (39) for a solar composition gas. Note that this "A–B" difference in chemical abundances was obtained when psi1 Dra A was directly analyzed with respect to psi1 Dra B in a strict line-by-line differential manner. The error bars are significantly smaller compared to the case in which the elemental abundances are first determined with respect to the Sun and then subtracted. This is a consequence of reducing the systematic errors of the analysis by avoiding a reference that is very dissimilar to either one of the psi1 Draconis stars.

Figure 3.18 shows that psi1 Dra A is metal-poor relative to psi1 Dra B. On average, the metallicity difference is -0.09 ± 0.04 dex. We do not detect a statistically significant correlation with the condensation temperature, but this is likely due to the relatively large errors in the abundance differences. In the Meléndez, Ramírez, et al. works the precision of relative abundances is of order 0.01 dex. In our case those errors are about 0.04 dex instead. Thus, we cannot rule out possible trends based on our data.

One may be tempted to attribute the elemental abundance discrepancy shown in Figure 3.18 to uncertain stellar parameters. The derived chemical abundances are most affected by the adopted $T_{\rm eff}$ values, and we have shown above that those of psi1 Dra B are reliable. Thus, we can explore this potential systematic error by simply calculating the relative abundances for different $T_{\rm eff}$ values for psi1 Dra A and keeping everything else constant. Increasing the $T_{\rm eff}$ of psi1 Dra A by 200 K would make the average elemental abundance difference nearly zero, but only for refractory elements ($T_{\rm cond} \gtrsim 1\,000$ K). The abundances of C and O in this case would differ by about -0.2 dex. On the other hand, decreasing the $T_{\rm eff}$ of psi1 Dra A by 200 K would make the C and O abundances difference nearly zero, but then the refractories would differ by about -0.2 dex. In both cases, we note that the element-to-element scatter as well as the line-to-line relative abundance scatter for individual elements increase relative to the case when our derived $T_{\rm eff}$ value is adopted instead. In other words, the elemental abundance differences are more internally consistent for our derived parameters, suggesting that the hotter or cooler temperatures of psi1 Dra A are not realistic (within our modelling assumptions, of course). Thus, it is not possible to reconcile the chemical abundance difference between psi1 Dra A and B by assuming that the $T_{\rm eff}$ of the former is either underestimated or overestimated. The M-dwarf contamination of psi1 Dra A can not explain the observed abundance difference either. Since only 1 % of the flux is from the M dwarf, the equivalent widths and abundances derived could have been underestimated by 1 % at most. This corresponds to less than about 0.005 dex in [X/H]. We are led to conclude that the offset seen in Figure 3.18 is real.

3.4.2.8 Possible interpretations

In the 16 Cygni system, the secondary hosts a gas giant planet whereas the primary has not yet shown evidence of sub-stellar mass companions. (53) found that 16 Cyg B is slightly metal-poor relative to 16 Cyg A and explained this observation as a signature of planet formation. Briefly, they suggested that the missing metals of 16 Cyg B are currently located inside its planet. Considering that hypothesis, possible explanations for our results regarding the psi1 Draconis system include:

1. The 16 Cygni planet signature hypothesis is incorrect because in psi1 Draconis, the secondary, which is a gas giant planet host, is actually more metal-rich than the primary, which does not show evidence of hosting planets in our RV data. Metals should have been taken away from the planet-host star psi1 Dra B and that star should be metal-poor relative to psi1 Dra A, which is the opposite of what we observe. In this case, the cause of the observed abundance differences seen in both 16 Cygni and in psi1 Draconis remains unknown.

2. Planet-like material and perhaps even fully-formed planets were once present in orbit around psi1 Dra A, with a total mass greater than that

of psi1 Dra B's planet or planets combined. However, the M-dwarf companion of psi1 Dra A made its planetary environment unstable, ejecting all of the planet material away from psi1 Dra A. In this scenario, the outer layers of psi1 Dra A would have accreted metal-poor gas during the planet-formation stage. The metals missing from psi1 Dra A would have been locked-up in the material that was ejected later. The late ejection of that material is required to explain our non-detection of planets around psi1 Dra A. Since psi1 Dra B has a planet (or two), its atmosphere is also depleted in metals relative to the initial metallicity of the system, but the metal depletion suffered by psi1 Dra A was greater. The latter would be easily explained by a larger total mass of planet-like material, but it could also be in part due to the thinner convective envelope of this warmer star, which did not dilute the chemical signature as much as psi1 Dra B.

3. psi1 Dra A never formed planets due to the influence of its low-mass stellar companion. On the other hand, psi1 Dra B formed much more planet-like material than seen today in the planet or planets that we have detected. A fraction of this material, that which is not in the planet(s) detected by us, was accreted into the star at a later stage, increasing the metallicity of its atmosphere. The amount of planet material accreted that is necessary to explain our observations had to have been larger than the total mass of the planet or planets detected. This is because the formation of those planets imply that metals were

already taken away from the star and this needs to be first compensated in order to result in a stellar atmosphere that is more metal rich than the birth cloud of the system. In this scenario, the metallicity of psi1 Dra A is that of the gas cloud from which both stars formed whereas psi1 Dra B's atmosphere became metal-rich at a later stage.

Rejecting the hypothesis by (53) that planet formation explains the metallicity difference of the 16 Cygni stars would be the most simplistic way of addressing our result for psi1 Draconis. However, such statement would leave us with no other explanation at the moment. Although the alternative scenarios presented above could appear contrived, they are all viable given our current understanding of how stars and planets form. Future analyses of other binary systems, ideally consisting of twin stars with detected planets, will allow us to put these results in a broader context and determine the real cause of these abundance anomalies.

3.5 Two "False Alarms" Related to Stellar Activity

3.5.1 HD 10086

We have obtained 84 RV measurements of HD 10086 over approximately 16 years, as listed in Table 3.10. The RVs have an RMS of 13.1 $\mathrm{m\,s}^{1}$ with a mean uncertainty of 6.3 $\mathrm{m\,s}^{1}$, indicating the potential presence of a periodic signal. The periodogram of the velocities (Figure 3.19) shows a broad peak centered at 2800 days. This signal may be modeled as a circular Keplerian orbit with period 2800 days and a semi-amplitude $K = 11$

m s^1, which would correspond to a planet with a minimum mass $M \sin i = 0.74 M_{\text{Jup}}$ at $a = 3.9$ AU.

Table 3.10. Radial Velocity and Ca H&K observations for HD 10086

	JD	RV ($\mathrm{m\,s^{-1}}$)	RV Uncertainty ($\mathrm{m\,s^{-1}}$)	S_{HK}	S_{HK} Uncertainty
1	2451152.73	7.03	7.18	0.312	0.020
2	2451213.65	-0.82	5.40	0.302	0.018
3	2451240.60	37.38	10.90	0.299	0.017
4	2451452.88	38.55	5.96	0.335	0.020
5	2451503.71	21.52	7.06	0.327	0.021
6	2451530.77	4.93	6.21	0.290	0.019
7	2451558.61	20.47	6.60	0.304	0.020
8	2451775.90	-2.81	5.69	0.273	0.020
9	2451777.91	12.08	6.24	0.278	0.020
10	2451778.92	11.12	5.88	0.294	0.020
11	2451809.79	12.37	5.89	0.294	0.019
12	2451859.78	-15.13	6.00	0.268	0.017
13	2451862.88	3.15	6.13	0.288	0.019
14	2451920.62	6.36	6.32	0.254	0.019
15	2451946.70	-3.76	6.87	0.226	0.016
16	2452141.93	23.11	5.87	0.310	0.021
17	2452181.95	13.16	6.03	0.288	0.019
18	2452219.91	-5.56	5.58	0.263	0.018
19	2452249.72	-14.36	6.19	0.260	0.018
20	2452306.66	-17.55	5.69	0.253	0.017
21	2452326.58	-6.20	6.24	0.276	0.018
22	2452492.95	15.44	9.75	0.307	0.022
23	2452538.91	-17.75	6.41	0.281	0.019
24	2452597.76	0.32	5.77	0.274	0.020
25	2452621.80	-16.86	5.76	0.266	0.018
26	2452658.69	-19.64	5.68	0.265	0.018
27	2452932.80	-21.56	5.64	0.274	0.018
28	2452959.78	-12.08	5.99	0.272	0.020
29	2453015.68	-17.60	6.22	0.258	0.016
30	2453035.60	-7.34	5.75	0.259	0.018
31	2453630.94	12.71	6.74	0.290	0.019
32	2453689.76	12.98	5.84	0.295	0.020
33	2453746.69	12.12	6.24	0.290	0.019
34	2453969.98	4.24	7.46	0.300	0.020
35	2454018.91	-10.94	6.15	0.266	0.019
36	2454068.81	1.73	6.07	0.286	0.020
37	2454781.88	-9.30	6.26	0.283	0.019
38	2455072.95	16.69	6.84	0.288	0.020
39	2455104.81	2.34	7.02	0.296	0.021
40	2455153.82	-8.54	6.80	0.292	0.018
41	2455173.83	-18.71	7.14	0.283	0.020
42	2455200.67	8.45	6.79	0.266	0.018
43	2455254.62	-0.47	6.66	0.259	0.017
44	2455254.63	-9.38	6.36	0.259	0.017
45	2455467.85	-2.35	6.39	0.264	0.019
46	2455528.76	-1.79	6.13	0.269	0.019
47	2455547.76	-21.86	5.99	0.256	0.020

Table 3.10 (cont'd)

	JD	RV ($\mathrm{m\,s^{-1}}$)	RV Uncertainty ($\mathrm{m\,s^{-1}}$)	S_{HK}	S_{HK} Uncertainty
48	2455616.61	-8.75	6.26	0.244	0.018
49	2455617.59	-6.67	5.93	0.249	0.019
50	2455792.92	-20.15	6.90	0.270	0.022
51	2455816.94	1.93	6.69	0.278	0.021
52	2455841.84	-7.77	5.74	0.263	0.019
53	2455845.82	-12.72	6.24	0.259	0.022
54	2455846.97	-23.20	6.23	0.259	0.019
55	2455874.75	-10.21	5.64	0.243	0.019
56	2455875.93	-24.53	6.30	0.236	0.021
57	2455899.61	0.90	6.53	0.277	0.022
58	2455909.63	-16.97	6.64	0.278	0.024
59	2455988.58	2.51	6.43	0.272	0.019
60	2456142.95	9.41	7.25	0.321	0.023
61	2456172.90	13.74	6.81	0.317	0.023
62	2456201.86	9.25	5.86	0.299	0.020
63	2456204.81	2.16	5.82	0.281	0.019
64	2456236.80	-10.10	5.62	0.283	0.019
65	2456236.80	-0.68	5.20	0.283	0.019
66	2456236.81	-7.00	5.64	0.284	0.020
67	2456266.68	5.30	5.90	0.292	0.020
68	2456315.58	11.21	6.05	0.286	0.019
69	2456354.60	6.41	6.54	0.264	0.018
70	2456354.61	-1.90	6.66	0.258	0.017
71	2456371.58	-6.61	5.89	0.273	0.018
72	2456518.97	6.91	7.17	0.286	0.021
73	2456527.90	3.32	6.45	0.303	0.021
74	2456559.81	0.42	6.63	0.290	0.019
75	2456562.85	-12.34	6.19	0.280	0.019
76	2456564.83	11.80	6.29	0.285	0.020
77	2456565.90	13.39	6.19	0.281	0.019
78	2456588.78	-1.75	5.59	0.314	0.021
79	2456613.80	5.23	5.90	0.268	0.020
80	2456640.62	2.30	6.28	0.268	0.019
81	2456642.67	-0.45	5.67	0.294	0.019
82	2456643.72	-1.31	5.37	0.262	0.018
83	2456671.63	19.27	6.20	0.297	0.018
84	2456698.60	12.09	6.13	0.283	0.018

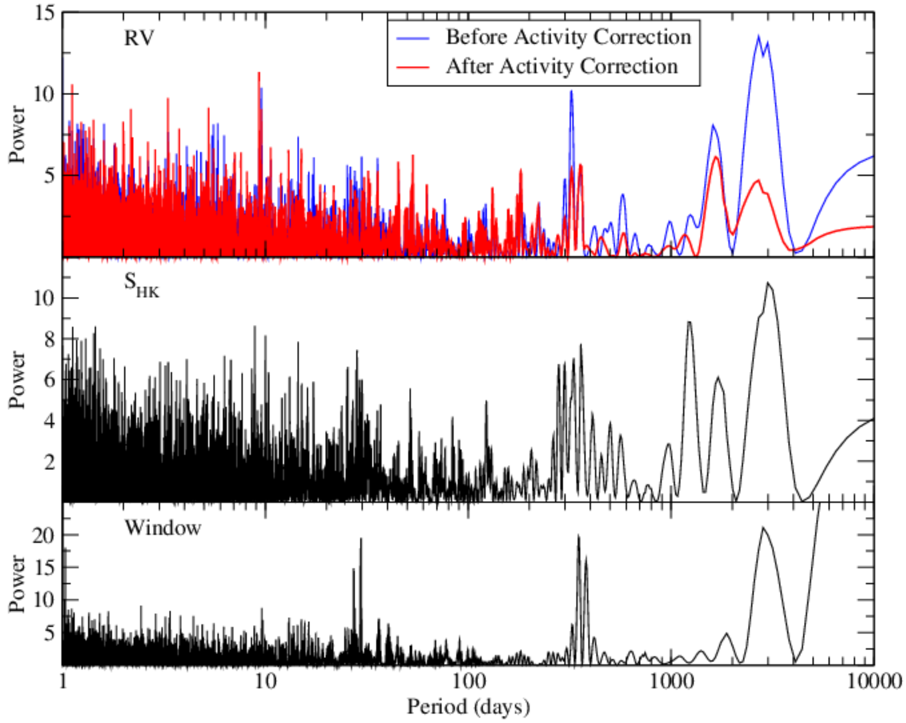

Figure 3.19 Generalized Lomb-Scargle periodograms of RV for HD 10086 before (blue) and after (red) correcting for stellar activity, along with the corresponding periodogram of S_{HK}.

However, in our analysis of stellar activity indicators for HD 10086, we see a 2800d peak in the periodogram of the S_{HK} Ca H&K index, suggesting the RV modulation may reflect a stellar activity cycle rather than a giant planet. Considering RV as a function of S_{HK} (Figure **??**) confirms this hypothesis. The RVs of HD 10086 are very strongly correlated with S_{HK}; a Pearson correlation test yields a correlation coefficient $r = 0.66$ which, for a sample size $N = 84$ indicates a probability of no correlation $P(r)$ less than 10^{-12}.

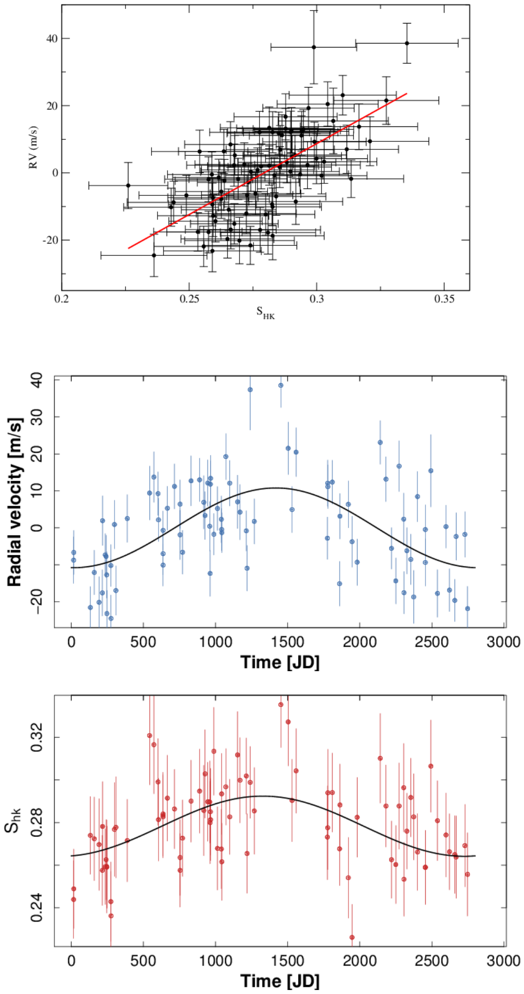

Figure 3.20 *Top Panel*: RV for HD 10086 as a function of S_{HK} at the time of each observation. The linear least-squares fit to the relation is given as a solid red line. *Middle and Bottom Panels*: RV and S_{HK}, respectively, folded to the 2800-day period of the stellar activity cycle. Sinusoidal models to each data set are shown as solid black curves.

Given the tight correlation between RV and Ca H&K emission for this star, we attempted to perform a simple stellar activity correction by fitting and removing a linear least squares model for RV versus S_{HK}. We find a linear fit of $v_r = -120(15) + 420(50) \times S_{HK}$. Upon subtracting this model from the RVs, we see from the activity-corrected periodogram that the 2800-day signal is almost completely eliminated, providing final confirmation that this signal is caused by Doppler shifts associated with a 7.7-year activity cycle. We show both RV and S_{HK} folded to the period of this cycle in Figure **??**. We see no statistically significant additional signals in RV, and conclude we have not discovered any exoplanets around this star to date.

3.5.2 β Virginis

We have observed β Virginis (hereafter β Vir) for approximately 16 years, obtaining a total of 311 RV measurements, as listed in Table 3.11. These velocities have an RMS of 9.0 $\mathrm{m\,s^{-1}}$ with a mean uncertainty of just 3.7 $\mathrm{m\,s^{-1}}$. In Figure 3.21, we show the Lomb-Scargle periodogram of the RVs, which includes a broad, highly significant peak at approximately 2000 days. The best Keplerian model to the data produces an eccentric ($e = 0.26$) orbit with $P = 2040$ days and $K = 9\ \mathrm{m\,s^{-1}}$.

Table 3.11. Radial Velocity and Ca H&K observations for beta Virginis

	JD	RV ($\mathrm{m\,s^{-1}}$)	RV Uncertainty ($\mathrm{m\,s^{-1}}$)	S_{HK}	S_{HK} Uncertainty
1	2451009.62	10.94	2.36	0.158	0.014
2	2451153.96	0.70	6.01	0.164	0.020
3	2451213.04	-4.39	2.46	0.159	0.020
4	2451241.87	-11.34	3.20	0.176	0.020
5	2451274.77	3.11	4.19	0.179	0.019
6	2451326.75	1.57	3.14	0.168	0.017
7	2451358.66	8.16	1.97	0.162	0.016
8	2451504.02	1.98	2.16	0.166	0.023
9	2451531.96	4.86	1.34	0.156	0.024
10	2451556.02	12.35	3.48	0.166	0.023
11	2451625.92	-2.45	3.09	0.165	0.020
12	2451656.75	-8.47	5.24	0.154	0.019
13	2451686.68	-6.96	2.59	0.164	0.018
14	2451751.60	-4.01	4.62	0.142	0.016
15	2451862.01	-0.55	4.19	0.168	0.022
16	2451918.95	-0.24	4.44	0.156	0.022
17	2451984.80	-8.63	1.64	0.158	0.020
18	2452037.71	-8.31	3.90	0.167	0.018
19	2452039.77	-5.37	1.30	0.159	0.018
20	2452249.01	-0.98	2.81	0.148	0.022
21	2452249.01	1.80	2.44	0.154	0.023
22	2452303.90	14.38	5.06	0.135	0.020
23	2452305.88	7.95	3.31	0.162	0.021
24	2452327.93	12.75	8.47	0.157	0.019
25	2452352.89	1.64	6.83	0.170	0.020
26	2452386.72	7.49	3.50	0.173	0.018
27	2452601.01	2.59	1.74	0.163	0.022
28	2452621.98	16.18	5.38	0.159	0.024
29	2452743.81	2.58	2.79	0.177	0.019
30	2452805.65	11.75	2.54	0.196	0.018
31	2452839.61	7.66	3.07	0.156	0.016
32	2453035.92	-0.15	3.66	0.159	0.022
33	2453069.82	-3.59	4.83	0.162	0.018
34	2453392.91	6.92	1.60	0.131	0.019
35	2453464.71	7.44	5.76	0.176	0.019
36	2453747.89	9.50	4.53	0.147	0.020
37	2453807.82	-12.83	2.03	0.167	0.021
38	2453862.76	11.48	2.59	0.177	0.018
39	2453906.62	1.72	2.51	0.164	0.016
40	2454158.86	-0.75	3.58	0.144	0.018
41	2454158.87	1.58	4.18	0.148	0.019
42	2454158.87	-0.93	5.49	0.148	0.018
43	2454158.87	-2.10	4.14	0.150	0.018
44	2454158.92	-3.04	2.87	0.150	0.019
45	2454158.92	-5.06	5.62	0.153	0.019
46	2454158.93	-3.16	4.38	0.153	0.019
47	2454159.88	-6.50	2.07	0.152	0.019

Table 3.11 (cont'd)

	JD	RV ($\mathrm{m\,s^{-1}}$)	RV Uncertainty ($\mathrm{m\,s^{-1}}$)	S_{HK}	S_{HK} Uncertainty
48	2454160.78	-2.83	2.65	0.154	0.018
49	2454160.79	-2.76	2.33	0.157	0.019
50	2454160.80	-5.20	3.54	0.157	0.019
51	2454160.81	-4.95	3.16	0.157	0.019
52	2454160.82	-4.64	3.15	0.160	0.019
53	2454161.75	1.19	3.80	0.151	0.018
54	2454161.76	-0.66	1.97	0.148	0.019
55	2454496.82	4.52	4.67	0.185	0.020
56	2454632.71	3.46	4.37	0.167	0.021
57	2454632.71	4.83	3.01	0.163	0.017
58	2454632.71	2.76	7.20	0.161	0.017
59	2454637.69	0.48	3.06	0.163	0.017
60	2454637.70	-3.28	1.57	0.158	0.017
61	2454637.70	1.95	1.87	0.161	0.018
62	2454821.04	10.63	6.03	0.159	0.017
63	2454821.04	15.65	1.92	0.183	0.024
64	2454821.04	7.46	3.90	0.180	0.023
65	2454837.92	16.57	2.56	0.182	0.023
66	2454837.92	10.69	3.50	0.180	0.022
67	2454838.93	27.78	5.30	0.185	0.023
68	2454838.94	17.80	4.13	0.174	0.022
69	2454838.94	15.41	2.67	0.176	0.022
70	2454839.01	10.23	4.39	0.174	0.022
71	2454839.02	16.87	2.89	0.186	0.023
72	2454839.02	24.31	5.83	0.182	0.023
73	2454841.02	26.04	7.81	0.182	0.023
74	2454841.02	21.51	5.05	0.174	0.022
75	2454841.02	21.63	4.37	0.170	0.021
76	2454869.03	8.84	3.67	0.171	0.021
77	2454869.03	10.65	1.38	0.176	0.020
78	2454869.03	8.03	3.63	0.177	0.020
79	2454869.86	2.78	1.98	0.178	0.020
80	2454869.86	2.40	3.04	0.176	0.021
81	2454869.86	5.25	2.32	0.171	0.020
82	2454870.01	9.61	4.06	0.175	0.021
83	2454870.02	4.91	1.97	0.185	0.020
84	2454870.02	4.51	2.63	0.182	0.019
85	2454870.02	2.66	4.17	0.183	0.020
86	2454871.91	-0.40	1.94	0.183	0.019
87	2454871.92	9.74	2.69	0.198	0.021
88	2454871.92	0.68	3.98	0.198	0.020
89	2454906.82	13.85	3.45	0.194	0.020
90	2454906.82	6.71	3.31	0.181	0.018
91	2454906.82	10.56	4.48	0.187	0.020
92	2454907.83	4.29	2.99	0.183	0.020
93	2454907.83	14.74	3.49	0.186	0.020
94	2454907.83	16.51	4.45	0.190	0.021

Table 3.11 (cont'd)

	JD	RV ($\mathrm{m\,s^{-1}}$)	RV Uncertainty ($\mathrm{m\,s^{-1}}$)	S_{HK}	S_{HK} Uncertainty
95	2454908.82	15.28	2.67	0.184	0.019
96	2454908.82	14.99	4.90	0.190	0.021
97	2454908.82	9.97	4.26	0.190	0.021
98	2454964.80	0.72	3.98	0.172	0.018
99	2454964.80	4.21	1.04	0.173	0.016
100	2454964.80	1.37	3.89	0.172	0.017
101	2454965.80	12.03	8.19	0.178	0.018
102	2454965.80	-9.28	3.76	0.177	0.019
103	2454965.80	0.32	8.73	0.176	0.018
104	2454986.66	8.46	3.16	0.176	0.016
105	2454986.66	12.56	3.52	0.176	0.016
106	2454986.66	10.29	2.85	0.178	0.017
107	2454987.71	12.71	1.77	0.179	0.017
108	2454987.71	9.92	2.80	0.177	0.016
109	2454987.72	9.25	5.16	0.177	0.016
110	2454989.69	14.39	2.26	0.174	0.015
111	2454989.70	11.57	4.05	0.175	0.015
112	2454989.70	8.90	6.29	0.174	0.016
113	2454990.66	24.40	3.03	0.178	0.015
114	2454990.66	17.59	3.94	0.180	0.017
115	2454990.66	22.21	4.10	0.179	0.016
116	2455172.01	16.32	2.30	0.158	0.023
117	2455172.01	16.16	3.08	0.160	0.024
118	2455172.02	7.58	4.51	0.157	0.024
119	2455173.03	-14.97	12.40	0.171	0.023
120	2455173.03	2.76	17.37	0.173	0.023
121	2455173.03	0.91	13.10	0.169	0.023
122	2455201.03	28.76	6.50	0.176	0.025
123	2455201.03	7.12	8.25	0.183	0.027
124	2455226.96	-0.04	5.79	0.164	0.022
125	2455226.96	2.89	2.68	0.164	0.023
126	2455226.97	1.65	5.24	0.165	0.022
127	2455227.97	6.26	2.34	0.169	0.020
128	2455227.98	21.70	2.37	0.171	0.021
129	2455227.98	23.00	3.60	0.170	0.021
130	2455280.79	3.79	1.14	0.167	0.021
131	2455280.80	2.00	2.21	0.166	0.021
132	2455280.80	7.77	1.64	0.163	0.021
133	2455287.73	15.69	2.56	0.173	0.020
134	2455287.73	11.78	4.75	0.172	0.019
135	2455287.73	15.56	4.75	0.174	0.020
136	2455315.72	-3.78	3.39	0.180	0.020
137	2455315.72	-0.80	5.75	0.180	0.020
138	2455315.72	-4.35	2.91	0.176	0.021
139	2455583.98	-13.73	4.18	0.157	0.025
140	2455583.98	-7.12	2.57	0.152	0.025
141	2455583.98	-5.60	3.76	0.148	0.025

Table 3.11 (cont'd)

	JD	RV ($\mathrm{m\,s^{-1}}$)	RV Uncertainty ($\mathrm{m\,s^{-1}}$)	S_{HK}	S_{HK} Uncertainty
142	2455583.98	-12.35	2.72	0.158	0.026
143	2455583.98	-11.66	3.08	0.152	0.023
144	2455616.93	-8.91	5.95	0.141	0.021
145	2455616.93	-3.56	5.78	0.144	0.020
146	2455616.93	-4.38	4.01	0.148	0.020
147	2455632.80	-23.22	1.45	0.149	0.017
148	2455632.80	-11.23	3.53	0.144	0.018
149	2455632.81	-13.29	3.20	0.149	0.018
150	2455647.66	-4.12	1.12	0.161	0.020
151	2455647.66	-6.87	2.42	0.156	0.020
152	2455647.66	-7.68	4.14	0.156	0.019
153	2455648.75	-2.73	1.54	0.155	0.019
154	2455648.75	-0.38	1.99	0.151	0.019
155	2455648.75	-5.22	3.47	0.156	0.020
156	2455665.78	-13.43	3.90	0.155	0.019
157	2455665.78	-12.85	4.30	0.150	0.017
158	2455665.78	-10.03	2.95	0.153	0.017
159	2455670.65	-11.89	2.43	0.162	0.020
160	2455670.65	-14.27	2.47	0.160	0.019
161	2455670.66	-14.15	3.25	0.156	0.022
162	2455700.68	-8.00	5.41	0.154	0.017
163	2455700.68	-11.72	4.90	0.153	0.019
164	2455700.68	-7.24	2.32	0.150	0.019
165	2455703.70	-0.10	1.58	0.161	0.019
166	2455703.70	-2.22	2.73	0.161	0.020
167	2455703.70	-9.39	4.04	0.163	0.019
168	2455723.71	-10.52	2.24	0.160	0.018
169	2455723.71	-10.72	2.91	0.154	0.016
170	2455723.71	-12.69	2.21	0.153	0.016
171	2455726.67	-2.03	4.42	0.165	0.020
172	2455726.67	-4.24	3.45	0.162	0.017
173	2455726.67	-2.06	2.74	0.146	0.019
174	2455964.89	-14.22	2.23	0.158	0.024
175	2455964.89	-15.36	2.93	0.162	0.024
176	2455964.89	-11.67	3.14	0.162	0.021
177	2455964.99	-7.53	2.04	0.175	0.024
178	2455964.99	-12.21	1.39	0.176	0.023
179	2455964.99	-10.79	3.53	0.173	0.023
180	2455968.90	-10.04	5.12	0.142	0.021
181	2455968.90	-5.10	3.13	0.149	0.023
182	2455968.91	-20.49	5.74	0.140	0.020
183	2455987.88	0.06	4.91	0.163	0.023
184	2455987.88	-0.82	4.42	0.159	0.022
185	2455987.88	-9.06	5.24	0.155	0.020
186	2455988.85	-11.87	4.44	0.159	0.020
187	2455988.86	-6.63	4.34	0.162	0.023
188	2455988.86	-9.99	6.16	0.165	0.023

Table 3.11 (cont'd)

	JD	RV ($\mathrm{m\,s^{-1}}$)	RV Uncertainty ($\mathrm{m\,s^{-1}}$)	S_{HK}	S_{HK} Uncertainty
189	2455989.88	-3.08	2.32	0.168	0.019
190	2455989.89	-2.38	3.39	0.182	0.020
191	2456015.75	-9.20	4.30	0.172	0.022
192	2456015.75	-9.99	2.00	0.169	0.021
193	2456015.76	-9.63	3.97	0.168	0.022
194	2456015.76	-7.39	4.56	0.170	0.023
195	2456015.76	-9.30	2.14	0.172	0.022
196	2456021.78	-4.88	3.16	0.165	0.022
197	2456021.78	-6.21	6.62	0.167	0.021
198	2456021.78	-2.90	2.36	0.170	0.022
199	2456022.73	-5.92	2.92	0.154	0.021
200	2456022.73	-6.18	3.15	0.153	0.021
201	2456022.73	-7.61	3.01	0.154	0.025
202	2456023.68	-4.50	2.29	0.176	0.022
203	2456023.70	-1.99	2.30	0.178	0.022
204	2456023.70	-6.72	2.21	0.178	0.024
205	2456024.69	-1.06	5.10	0.143	0.018
206	2456024.70	-0.37	3.84	0.144	0.019
207	2456024.70	-2.71	2.38	0.142	0.017
208	2456049.73	-13.50	2.24	0.169	0.020
209	2456049.74	-11.41	2.05	0.162	0.020
210	2456049.74	-9.97	4.57	0.169	0.020
211	2456051.73	-9.05	2.53	0.171	0.022
212	2456051.73	-7.15	3.86	0.163	0.020
213	2456051.73	-5.06	5.11	0.167	0.020
214	2456053.71	-11.02	5.07	0.167	0.020
215	2456053.72	-11.20	5.30	0.164	0.019
216	2456054.67	-10.89	3.93	0.163	0.021
217	2456054.68	-8.69	2.55	0.158	0.019
218	2456110.62	-6.64	2.93	0.172	0.021
219	2456267.99	-8.90	2.92	0.167	0.025
220	2456267.99	-7.98	1.52	0.164	0.024
221	2456267.99	-3.26	3.85	0.164	0.024
222	2456315.95	1.08	5.81	0.177	0.025
223	2456315.95	-4.37	5.26	0.174	0.024
224	2456315.95	4.10	8.54	0.177	0.024
225	2456316.96	4.77	2.61	0.165	0.022
226	2456316.96	4.68	2.71	0.166	0.023
227	2456316.96	3.76	3.96	0.164	0.022
228	2456318.94	7.13	2.72	0.167	0.022
229	2456318.94	0.66	4.02	0.167	0.022
230	2456318.94	8.63	2.82	0.166	0.022
231	2456319.93	-4.31	4.22	0.172	0.024
232	2456319.93	-1.52	4.11	0.165	0.022
233	2456319.94	-2.43	2.50	0.167	0.022
234	2456320.94	-12.14	4.99	0.174	0.024
235	2456320.94	-6.47	5.14	0.173	0.022

Table 3.11 (cont'd)

	JD	RV ($\mathrm{m\,s^{-1}}$)	RV Uncertainty ($\mathrm{m\,s^{-1}}$)	S_{HK}	S_{HK} Uncertainty
236	2456320.94	1.86	5.37	0.174	0.023
237	2456350.88	-0.58	2.84	0.166	0.020
238	2456350.89	-1.07	2.45	0.170	0.021
239	2456350.89	-0.53	3.87	0.167	0.019
240	2456351.92	0.78	4.37	0.179	0.021
241	2456351.93	2.69	6.30	0.176	0.020
242	2456351.93	0.59	3.14	0.175	0.020
243	2456352.99	-8.20	3.19	0.164	0.019
244	2456352.99	-8.29	3.14	0.162	0.019
245	2456352.99	-2.37	5.33	0.162	0.019
246	2456353.94	-10.39	5.78	0.172	0.020
247	2456353.94	-8.06	6.44	0.174	0.020
248	2456353.94	-4.62	6.59	0.173	0.020
249	2456354.92	-13.52	2.59	0.174	0.020
250	2456354.92	-6.13	3.88	0.168	0.020
251	2456354.92	9.29	3.06	0.169	0.021
252	2456371.86	0.47	4.22	0.164	0.020
253	2456371.86	-5.54	1.40	0.166	0.020
254	2456371.87	-3.36	2.34	0.165	0.020
255	2456372.82	-7.93	2.42	0.169	0.021
256	2456372.82	-7.45	2.55	0.166	0.021
257	2456372.82	-4.20	4.39	0.168	0.020
258	2456378.81	-1.25	2.29	0.167	0.020
259	2456378.81	-2.99	1.18	0.164	0.019
260	2456378.81	-1.59	1.21	0.168	0.021
261	2456401.75	-9.87	3.33	0.167	0.020
262	2456401.75	-6.68	3.09	0.166	0.019
263	2456401.75	-3.47	1.56	0.167	0.019
264	2456405.75	-1.25	3.46	0.171	0.019
265	2456405.75	-4.09	5.40	0.175	0.020
266	2456405.75	-1.67	4.66	0.171	0.019
267	2456406.76	-10.96	3.29	0.172	0.019
268	2456406.76	-9.62	2.11	0.169	0.019
269	2456406.77	-6.43	1.79	0.171	0.020
270	2456432.71	0.83	3.29	0.168	0.018
271	2456432.71	2.09	3.99	0.170	0.018
272	2456432.71	-5.50	3.09	0.169	0.018
273	2456434.71	-2.94	3.95	0.161	0.018
274	2456434.72	-7.25	4.00	0.145	0.018
275	2456434.72	0.03	3.63	0.157	0.019
276	2456435.70	2.05	4.58	0.154	0.017
277	2456435.70	-0.40	3.95	0.142	0.017
278	2456435.70	-1.51	3.17	0.143	0.017
279	2456437.69	-3.66	3.33	0.146	0.015
280	2456437.69	1.16	1.86	0.143	0.015
281	2456437.69	4.18	2.09	0.145	0.016
282	2456466.62	-9.84	2.66	0.173	0.017

Table 3.11 (cont'd)

	JD	RV ($\mathrm{m\,s^{-1}}$)	RV Uncertainty ($\mathrm{m\,s^{-1}}$)	S_{HK}	S_{HK} Uncertainty
283	2456466.62	-4.77	4.28	0.172	0.018
284	2456466.62	1.20	3.36	0.173	0.018
285	2456467.64	4.04	5.15	0.162	0.018
286	2456467.64	4.54	3.37	0.166	0.017
287	2456467.64	0.70	2.60	0.167	0.018
288	2456625.03	-6.79	2.00	0.164	0.024
289	2456625.03	-2.66	2.03	0.166	0.024
290	2456625.03	-7.58	2.82	0.165	0.024
291	2456641.04	-0.15	5.10	0.146	0.024
292	2456641.04	3.85	3.34	0.155	0.024
293	2456641.04	7.40	1.70	0.157	0.023
294	2456642.05	3.41	1.60	0.162	0.024
295	2456642.05	-2.75	3.11	0.158	0.023
296	2456642.05	4.41	5.41	0.157	0.024
297	2456643.04	5.37	3.86	0.152	0.022
298	2456643.04	-0.34	3.29	0.162	0.024
299	2456643.04	2.36	2.89	0.135	0.023
300	2456644.04	3.04	5.01	0.177	0.024
301	2456644.04	0.18	6.83	0.176	0.024
302	2456644.04	-10.23	2.98	0.175	0.024
303	2456672.97	5.85	4.10	0.160	0.021
304	2456672.98	-0.70	2.36	0.161	0.021
305	2456672.98	1.87	1.42	0.157	0.023
306	2456673.98	6.99	5.27	0.158	0.022
307	2456673.98	6.22	3.95	0.158	0.023
308	2456673.99	0.75	2.49	0.160	0.022
309	2456696.87	0.10	2.86	0.164	0.021
310	2456696.88	-0.58	2.48	0.163	0.021
311	2456696.89	-0.08	5.38	0.163	0.021

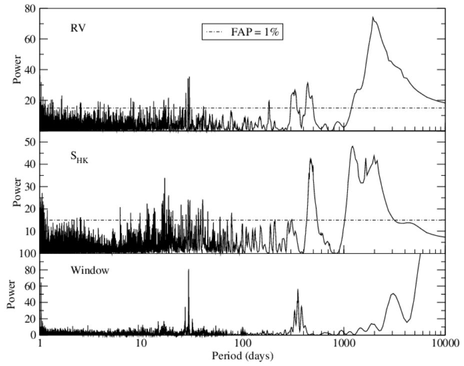

Figure 3.21 Generalized Lomb-Scargle periodograms of RV and S_{HK} for β Virginis. The threshold for a false alarm probability (FAP) of 1% is shown as a dash-dotted line.

If the RV modulation is indeed produced by an exoplanet, this Keplerian model corresponds to a gas giant orbiting at $a = 3.5$ AU with minimum mass $M \sin i = 0.65 M_{\text{Jup}}$. As with HD 10086, though, the Ca H&K emission of β Vir suggests the observed signal is not associated with a planet. We include the periodogram of S_{HK} in Figure 3.21, which also includes a very broad peak between 1000 and 2500 days. RV as a function of S_{HK} (Figure 3.23) again shows a highly significant correlation; we compute a Pearson correlation coefficient $r = 0.39$ and a probability $P(r) < 2 \times 10^{-12}$ of no correlation. We therefore suspect the periodicity observed for β Vir is also a stellar activity cycle which mimics a Doppler shift such as would be expected for a Jupiter analog planet.

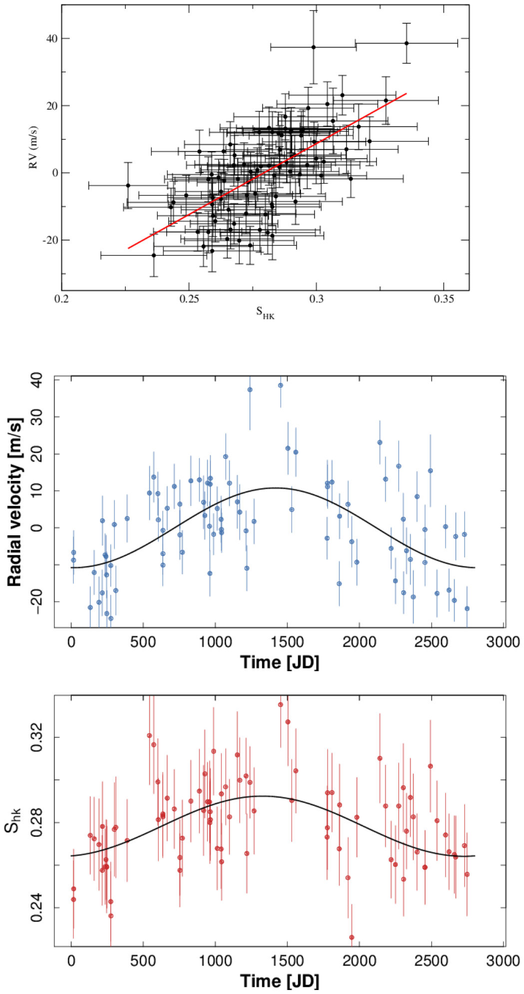

Figure 3.22 *Top Panel*: RV for HD 10086 as a function of S_{HK} at the time of each observation. The linear least-squares fit to the relation is given as a solid red line. *Middle and Bottom Panels*: RV and S_{HK}, respectively, folded to the 2800-day period of the stellar activity cycle. Sinusoidal models to each data set are shown as solid black curves.

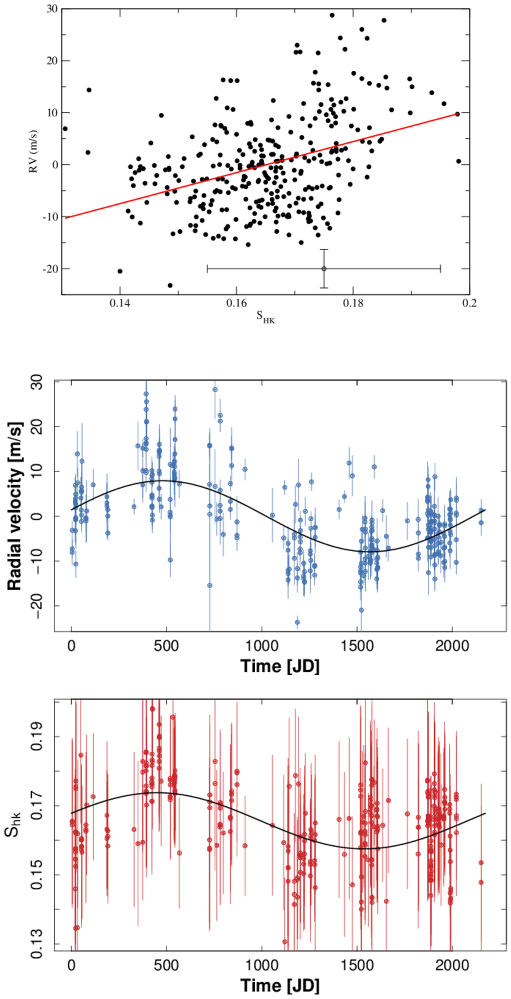

Figure 3.23 *Top Panel*: RV as a function of S_{HK} for β Virginis. The linear least squares fit to the data is shown as a solid red line. For the sake of visibility we do not show error bars on the individual points, but indicate the mean 1σ uncertainty on each variable. *Middle and Bottom Panels*: RV and S_{HK}, respectively, folded to the 2200-day period of the stellar activity cycle. Sinusoidal models to each data set are shown as solid black curves.

A number of features of our data set for β Vir prevent the application of a simple stellar activity correction analogous to the one we performed for HD 10086. First, the weaker calcium emission (mean $S_{HK} = 0.17$, versus 0.28 for HD 10086) leads to lower signal to noise in the Ca H&K measurements. Furthermore, our RVs show significant short-term scatter (5.1 $\mathrm{m\,s^{-1}}$ over the 2013 observing season) and possibly a long-term linear acceleration in addition to the activity-induced periodicity. Finally, the "eccentricity" of the RV signal created by the activity cycle suggests the activity signal may be non-sinusoidal, and the RV-activity relationship may therefore not be linear. These factors make it especially difficult to fit and subtract a simple activity-RV dependence, and therefore do not attempt a stellar activity correction for β Vir. The matching periodicities in RV and Ca H&K and the correlation between RV and S_{HK} lead us to conclude the observed signal is due to a stellar activity cycle, but the evaluation of any additional (possibly planetary) signals in the velocities must be postponed pending a more sophisticated stellar activity analysis, which is beyond the scope of this paper.

3.6 Conclusion

This work has been made possible through the National Science Foundation (Astrophysics grant AST-1313075) and various NASA grants over the years. We are grateful for their generous support.

This research has made use of the SIMBAD database, operated at CDS, Strasbourg, France.

We would like to thank all the people who have helped gather data over the years for the 2.7m radial velocity search program at McDonald Observatory, including Diane Paulson and Stuart Barnes.

Chapter 4

Detailed Chemical Abundances of Giant-Planet-Host Stars: I - Methods and Tools

4.1 Introduction

There is persuasive evidence that the stellar hosts of known ∽Jovian-mass giant planets are enhanced in overall metallicity, when compared to the average local field (Gonzalez 1997; Santos et al. 2005; Fischer & Valenti 2005; Sousa et al. 2011) (among others). This "planet-metallicity correlation" lends strong support to the core-accretion theory of planet formation, in which the cores of giant planets are thought to grow through accretion of solid, metal-rich material beyond the "ice line" (i.e. where water is expected to exist primarily in solid form) in the disks surrounding newly formed stars (Safronov 1969). Upon reaching a critical mass of 10-20 M$\oplus$, the core is then able to rapidly accrete hydrogen and helium from its surroundings, provided the gaseous disk has not yet been dissipated by stellar winds (Pollack et al. 1996).

Recent evidence suggests that this correlation may be weaker for stars hosting ∽Neptunian-mass planets (Ghezzi et al. 2010; Sousa et al. 2008); and as demonstrated by Buchhave et al. (2012), there may be no such correlation for $\backsim$terrestrial-sized planets. Together with the earlier studies of gas giant host stars, these more recent results provide further evidence that the majority of known short-period giant planets formed via core-accretion. The implication is that at higher overall metallicities, core growth proceeds more rapidly/efficiently, allowing the core to achieve critical mass before the disk dissipates. This is especially important, given relatively short disk dissipation timescales that are thought to be on the order of a few million years (Haisch, Lada & Lada 2001). Smaller planets on the other hand, need not form within this short window of time, since they are composed primarily of refractory material, and so are able to form around stars with a wider range of overall metallicity.

The role of individual elements in this picture is much less clear, however. It is important to note that when used in the context of stellar spectroscopy, the term "overall metallicity" almost always refers to the iron abundance of the star (for pragmatic and historical reasons). It may be convenient from a spectroscopic standpoint, but iron is likely not a good proxy for measuring the abundances of the various materials that are thought to play key roles in planet formation.

Within the context of the core accretion model of giant planet formation, planetesimal precursors form through coalescence of small (micron-sized, initially) solid grains. These grains are thought to be composed primarily of refractory silicates, and beyond the ice line of the disk thick mantles of frozen water, methane, ammonia, etc. may condense onto these grains (Hayashi 1981; Weidenschilling 1977). Thus, the dominant mass contributor to these grains, and therefore to the cores of giant planets, is thought to be oxygen. Carbon is also important, and perhaps a special case in that it may contribute significant mass both to the original grain (Henning & Salama 1998), and to the subsequent mantle via heavy organic compounds (Lodders 2004) and methane ice (Dodson-Robinson & Bodenheimer 2010). Oxygen and carbon are followed in importance by the highly refractory elements iron, silicon and magnesium; with sulfur and nitrogen rounding out the list of the most important mass contributors (Dodson-Robinson 2011).

We began our spectroscopic studies with the guiding hypothesis that if core accretion is responsible for the majority of known giant planets, then their stellar hosts should be enhanced in the key elements discussed in the previous paragraph. The case for iron was already well established, so we chose to focus first on oxygen and silicon, since these are thought to be the single most important and abundant volatile and refractory (after iron, perhaps), respectively, elements from a planet-forming perspective. In Brugamyer et al. (2011) we indeed reported a significant (99% probability) enhancement in Si abundances for a sample of 76 giant-planet-host stars, when compared to a control sample of 80 stars that had not demonstrated any RV trends indicative of unseen companions over the ∽10-year monitoring baseline of the McDonald Observatory Planet Search program (MOPS). Critically, this enhancement was seen even when controlling for the known, underlying overall planet-metallicity (i.e. Fe) correlation. That is, when comparing similar [Fe/H] distributions of stars with and without known planets, the planet-hosting stars in our sample demonstrated a small, but very statistically significant, enhancement in Si relative to Fe. Surprisingly, we found no such correlation for oxygen.

We hypothesized that this result could nevertheless be explained in the context of core accretion, by positing that as the initial "seeds" onto which water vapor condenses, silicates are the bottleneck in the process of grain (1) growth, (2) settling in the disk, and (3) agglomeration into the planetesimal "rubble piles" that ultimately form planet cores via collisions. It may be that without these initial seeds, the process of planet formation is more-or-less independent of the amount of volatile species present in the disk, despite their much higher relative cosmic abundances – from a factor of 2 for N, to more than 10 for O (Asplund et al. 2006). We compare our proposed mechanism to cloud formation on the Earth: without nucleation sites – such as dust or bacteria – no clouds can form, even with an atmosphere that is virtually super-saturated with water vapor.

This view has been supported by prior and subsequent work of various other groups. Haywood (2008) reported that at sub-solar metallicities, planet-hosts seem to preferentially belong to the galactic thick disk. We can readily explain this phenomenon by considering that many studies have found that among thick disk stars, ratios of [X/Fe] > 0[1] are very common

---

[1] Here we use the usual notation: $[X/Fe] = [X/H] - [Fe/H]$, where $[X/H] = \log(\frac{N(X)}{N(H)})_{\star} - \log(\frac{N(X)}{N(H)})_{\odot}$, and where $N(X)$ is the number density.

for alpha-elements, particularly for O, Mg, Si, Ca, and Ti (Reddy et al. 2006; Neves et al. 2009) (among others). Indeed, Robinson et al. (2006) reported relative Si and Ni enhancement in their sample of planet hosts. More recently, Adibekyan et al. (2012) reported significant Mg enhancement among the HARPS planet hosts.

Based on our and others results, we predicted that giant-planet-hosts should demonstrate statistical enhancements in the most abundant refractory elements (Si, Mg, and S) responsible for initial grain formation; while no such correlations should exist for the most abundant volatile elements (O, N, and possibly C) responsible for icy mantle growth. If our view is correct, perhaps even the less abundant refractory elements Al, Na, Ca, Ni, etc. will be shown to demonstrate positive correlations with planet detection. Again, we must stress that this prediction must hold true at a given overall [Fe/H] in order that our hypothesis is supported.

Exploring these trends in precise detail – and doing so using true, robust differential measurements (with respect to the Sun) – requires line-by-line individual abundance determinations using uniform, high-resolution and high signal-to-noise data. And this is best accomplished using traditional, tried-and-true equivalent width (EW) curve of growth (COG) analysis methods, such as that employed by the popular line analysis program MOOG (Sneden 1973). Unfortunately, comprehensive analysis of the planetary community's ever-growing stellar data-sets is not practical using the traditional, widely available (manual) EW measurement and COG analysis tools. Recognizing this, much of the community has turned to automated spectral synthesis and/or spectral matching techniques. Such approaches present their own unique problems, however, some of which could have serious consequences when attempting to determine precise stellar parameters and relative abundances. The goal of the present project was development of an integrated, flexible, convenient tool for the (semi-)automated spectroscopic analysis of high-quality data-sets using established, well-researched COG methods, as a possible alternative to the increasing number of spectral synthesis and spectral matching tools.

We discuss here a processing and analysis pipeline that enables us, using a minimal number (5) of short keystrokes, to take a spectrum from the raw, 2-D echelle image stage to a final entry for that particular star in a master catalog containing all relevant stellar parameters and photospheric abundances (as well as error estimates on these) in a short amount of time (essentially all of which is CPU time). For this, weve utilized a combination of "borrowed" and "from scratch" IRAF, IDL, and Fortran routines. These efforts have been critical in our quest to uniformly analyze – using a traditional EW COG approach – our large data-set ($\backsim$1000 individual spectra × $\backsim$400 lines each = 400,000 individual measurements). We are now enabled to thoroughly and uniformly explore individual elemental abundance trends for every element thought to be important for purposes of giant planet core formation, excepting nitrogen. (Unfortunately, there are essentially no known visual-wavelength transitions of elemental N.)

4.2 Data

4.2.1 Sample Selection

We selected our target sample of stellar hosts from the literature, with the aid of the online Extrasolar Planets Encyclopaedia[2]. We selected only targets with at least one *confirmed* (i.e. using radial velocity measurements) planetary-mass (i.e. less than 13 Jupiter-masses) orbiting companion. We included essentially all known mid-F to early-K dwarf (V) and sub-giant (IV) planet hosts that are observable from McDonald Observatory ($30.68°$ North latitude; $104.03°$ West longitude) and bright enough to allow for a signal-to-noise ratio S/N $\gtrsim$ 100 in a "reasonable" exposure time (e.g. $\leq$ 60 min.; although most exposures were $\leq$ 20 min.) using either the 2.7-meter Harlan J. Smith Telescope (HJST) or 9.2-meter Hobby-Eberly Telescope (HET). Since almost all of these planetary companions were discovered via the radial-velocity technique, which is heavily biased towards large planets in small orbits, the vast majority of them are close-in giant planets (i.e. ∽Jupiter mass or larger; in an orbit with a semi-major axis less than 0.1 AU). Our final list of observed (see section 4.2.2) planet-hosts numbers ∽220 stars, and will be presented and discussed in Paper II.

We selected our target sample of stellar non-hosts from the High Accuracy Radial Velocity Planet Searcher (HARPS)[3], California Planet Search[4],

---

[2] http://exoplanets.eu/

[3] This spectrograph is installed on the European Southern Observatory's 3.6-meter Telescope at La Silla Observatory in Chile.

[4] This refers to a radial velocity survey conducted using two instruments: the High Res-

and McDonald Observatory Planet Search (MOPS)[5] radial-velocity survey programs. These are stars that have been monitored for many years, and that have (as yet) no known confirmed planetary-mass companions. We save a detailed discussion of these programs – their RV precision, time baselines, constraints on companion absence (or presence) – for Paper II. [for California Planet Search: Isaacson & Fischer 2010, Wright 2005, and Valenti & Fischer 2005. for HARPS: several to choose from. for MOPS: Wittenmyer et al. 2006, and/but might one of Paul Robertson's papers also work?] As with the planet host list, we targeted essentially all mid-F to early-K dwarf (V) and sub-giant (IV) stars from these sources that are observable from McDonald Observatory and bright enough to allow for a signal-to-noise ratio S/N $\gtrsim$ 100 in a "reasonable" exposure time (e.g. $\leq$ 60 min.; although most exposures were $\leq$ 20 min.) using either the 2.7-meter Harlan J. Smith Telescope (HJST) or 9.2-meter Hobby-Eberly Telescope (HET). Our final list of observed (see section 4.2.2) non-hosts numbers $\backsim$430 stars, and will be presented and discussed in Paper II.

4.2.2 Data Acquisition

All of our stellar spectra were independently acquired by us at McDonald Observatory, using only two instruments, and with a single instru-

---

olution Echelle Spectrometer – or HIRES – on the Keck I telescope, and the Hamilton Spectrometer on the Shane Telescope at Lick Observatory.

[5] This radial velocity survey program is conducted using the Tull Spectrograph on the HJST.

mental configuration for each. Thus, our data are highly uniform, which decreases internal uncertainties. We obtained the significant majority of our spectra between 2009 and 2013, excepting ∽100 MOPS program template spectra (e.g. without the RV-reference iodine cell in the light path) that were obtained as early as 1998. We generally chose to observe our brighter targets ($\lesssim 9^{th}$ magnitude) on the smaller HJST, and our fainter targets ($\gtrsim 8^{th}$ magnitude) on the larger, queue-scheduled HET.

For the HJST, we utilized the cross-dispersed echelle Tull Spectrograph (formerly the Tull Coudé Spectrometer) (Tull et al. 1994). For our configuration we used the "E2" grating (with 52.67 groove mm^{-1}) and the "TK3" CCD (a 2048×2048-pixel Tektronix CCD with 24 μm pixels). With a 1.2 arcsec slit, this configuration yields a resolving power (=$\lambda/\Delta\lambda$) of R=60,000, with wavelength coverage from 3750 Å to 10,200 Å. This coverage is complete from the short wavelength end to 5691 Å – with increasingly large inter-order gaps from there to the long wavelength end.

For the HET telescope, we utilized the fiber-fed cross-dispersed echelle High Resolution Spectrograph (Tull 1998). This instrument uses a mosaic of two 2048×4102-pixel Marconi Applied Technologies (now E2V Technologies) CCDs with 15 μm pixels. For our configuration we used a grating with 316 groove mm^{-1} and a 2.0 arcsec fiber, which yields a resolving power of R=60,000. The wavelength coverage extends from 4090 Å to 7875 Å and is complete except for the range 5930 Å to 6012 Å, corresponding to the physical gap between the two CCDs.

Our exposure times were generally calculated with a desired target S/N ratio of 300, wherever possible. Of course, trade-offs between S/N and exposure times were necessary for our faintest targets, and/or in cases of poor observing conditions. We note, however, that no spectra with S/N $<$ 100 were included in our final analysis. So, the S/N ratio of our data range from 100∽500, with the majority between 200∽300 – a level we have found allows for robust, precise, and reasonably "accurate" (e.g. when compared to other methods/tools) stellar parameter and abundance determinations.

We stress, then, that our raw data were acquired in a highly uniform manner – using consistent configurations on only two instruments. In our opinion, this uniformity in our data-set is a key part of our goal to derive relative abundances at the ∽0.05 dex precision level, wherever possible.

4.2.3 Data Reduction

All data were reduced in a uniform manner using pipelines (one each for the HJST and HET instruments) originally developed by W. D. Cochran for the MOPS program [ask Bill about a possible reference here]. These pipelines utilize standard routines contained in the *echelle* and *onedspec* packages of the Image Reduction and Analysis Facility (IRAF), and include the following steps:

- Overscan, trim, and bad pixel processing

- Bias frame subtraction (using co-added master)
- Flat field frame preparation (co-added master)
- Scattered light fitting and removal
- Flat field division
- Order extraction and cosmic ray removal[6]
- Blaze spectrum preparation (co-added master)
- Thorium-Argon comparison lamp spectrum extraction
- Wavelength solution and application

The preliminary data product from these pipelines are multi-order (echelle), wavelength-calibrated 1-D spectra. For the present work, we have developed an automated IRAF routine to handle the following additional reduction steps:

- Removal (division) of the blaze function in batch mode, using the *imarith* task
- Continuum normalization, using the *continuum* task

---

[6] Most cosmic rays are removed successfully in the *apall* task using the extraction parameter *pfit*, a profile fitting algorithm. Occasionally, however, it's necessary to remove particularly troublesome cosmic ray hits manually (with the aid of the SAOImage DS9 image application) using the *imedit c*, *f* and/or *l* replacement algorithms.

- Combining of the orders, using the *scombine* task

The final data products from our reduction pipelines are single (one for each spectrum) ASCII text spectra, containing a two-column list of wavelengths and normalized flux values, ready for use with our equivalent width measurement routines (as described in section 4.4).

4.3 Species and Line Selection

We have carefully developed our own extensive line-lists[7] for our targeted species, including the potentially important (from a planet formation perspective, that is) elements C, O, Na, Mg, Al, Si, S, Ca, Fe, and Ni; along with various less abundant species at $Z < 31$. We've also included in our analysis two "control" elements Sc and V that should not be significant planet-mass contributors (they are 3-4 orders-of-magnitude less abundant than Fe and Si, for example), nor should they trace elements that might be significant (since they are not alpha-elements). In total, our final line-lists comprise 400 individual vetted absorption lines that were carefully examined in a very high-quality solar spectrum, and thoroughly tested for internal consistency.

---

[7] The term "line-list" herein means a selection of suitable absorption lines of a given elemental species amenable to accurate/precise equivalent width measurement, containing the transition wavelength, species identification, excitation potential, and log(gf) value (the log of the oscillator strength times the statistical weight of the lower level, where the oscillator strength represents the probability of photon absorption and the statistical weight is the number of possible states).

Ideally we wish to find isolated, clean, weak lines. Isolated, so that the wings of the lines can be properly fit. Clean, so that no blends contribute to the measured EW. Weak, so that the lines fall on the linear portion of the curve-of-growth.

The process of building these lists was as follows:

1. We queried the National Institute of Standards and Technology (NIST) Atomic Spectra Database[8], as well as Charlotte Moore's solar atlas (Moore 1966).
   - We searched for all lines with measured excitation potentials and oscillator strengths in the range 4100-7800 Å, corresponding to the wavelength coverage of our HET HRS configuration (note that the HJST Tull Spectrograph in our configuration covers more than this).
   - We rejected all lines in the following ranges of significant telluric contamination: 5860-6020 Å, 6275-6345 Å, 6425-6640 Å, 6860-7460 Å, and 7590-7750 Å.
2. We visually examined each line in a high-quality ($S/N > 500$) day-sky spectrum, taken through the solar port of the HJST (and in the same configuration as our program spectra).

---

[8] http://www.nist.gov/pml/data/asd.cfm

    - We rejected lines that were obviously masked, blended and/or crowded.

3. We manually measured EWs of the remaining lines in our solar port spectrum, and fed these through the *abfind* driver of MOOG to determine individual line abundances.

    - If a particular line gave a result significantly different than that expected for the Sun, [we attempted to identify possible reasons: such as too strong; checked the C. Moore solar atlas for possible identified masks and/or blends; very poor-quality log (gf) values] it was rejected.

4. We rejected lines for which the listed NIST laboratory-measured log(gf) values gave abundances that were more than 0.4 dex off from accepted solar values.

    - NOTE: C. Moore solar atlas does not list log gfs. A relatively small number of kept lines from C. Moore solar atlas were not listed in NIST (around twenty). For these, log gfs are purely "solar values" – they were selected/adjusted to match expected solar abundance values.

5. Where necessary (20-30% of lines, in the end), adjust log (gf)s to give solar atmospheric parameters and abundances, but only for lines with

a NIST accuracy grade of "B" or worse[9].

6. Finally, measure EWs of remaining lines in ten test stars (spanning a range of Teff and log g) and run results through MOOG
   - Reject lines that do not give internally consistent abundance values (i.e. reject if abundance value derived from that line differs from the average for that species by $\gtrsim$ 2-sigma)

For reasons explained later, we used Lawler et al. (2013) Ti values. These are purely lab E.P. and log gf values. For these, the process was slightly different. We first selected lines in the wavelength range 4100-7800 Angstroms, and examined each line in our solar spectrum, rejecting obvious masked, blended and/or crowded lines. We then meaured EWs in our solar spectrum for all kept lines and run these through MOOG, rejecting lines that don't give "solar" values.

Our Final lists contain ∽400 lines total. The following tables list our Fe I, Fe II, Ti I, and Ti II linelists. We included them here since they are used for determining fundamental stellar parameters (discussed later).

---

[9] The oscillator strengths for the oxygen triplet at 7774 Å, for example, are well-known and the listed NIST values are given an "A" for accuracy. For cases such as these, we made no changes to the listed log (gf) values whatsoever.

Table 4.1. List of Fe I lines

Wavelength (Angstroms)	Excitation Potential (eV)	Oscillator Strength (log *gf*)	Solar Equivalent Width (mÅ)
4489.74	0.12	-3.90	104.7
4523.40	3.65	-1.96	47.8
4537.67	3.27	-2.90	18.0
4547.85	3.55	-1.01	95.3
4551.65	3.94	-2.00	30.5
4554.45	2.87	-2.75	42.6
4556.93	3.25	-2.66	29.1
4566.51	3.30	-2.10	55.2
4574.22	3.21	-2.45	43.3
4593.53	3.94	-2.03	27.9
4596.42	3.65	-2.15	33.7
4602.00	1.61	-3.20	76.0
4602.94	1.49	-2.15	139.3
4741.53	2.83	-1.95	81.0
4749.95	4.56	-1.25	37.0
4779.44	3.42	-2.10	43.6
4787.83	3.00	-2.60	47.8
4788.76	3.24	-1.76	69.7
4793.96	3.05	-3.47	9.3
4799.41	3.64	-2.10	38.9
4802.88	3.64	-1.60	62.8
4808.15	3.25	-2.65	31.6
4809.94	3.57	-2.60	22.7
4961.91	3.63	-2.35	27.8
4962.57	4.18	-1.20	57.5
4994.13	0.92	-3.30	109.2
5044.21	2.85	-2.20	80.3
5083.34	0.96	-3.20	112.8
5127.36	0.92	-3.45	100.5
5141.74	2.42	-2.15	95.1
5151.91	1.01	-3.30	115.1
5194.94	1.56	-2.30	143.3
5197.94	4.30	-1.45	40.4
5198.71	2.22	-2.20	103.3
5225.53	0.11	-4.79	78.4
5242.49	3.63	-1.10	91.2
5243.78	4.26	-1.10	66.9
5247.05	0.09	-4.95	73.9
5250.21	0.12	-4.85	79.5
5253.46	3.28	-1.60	88.3
5288.52	3.70	-1.51	65.7
5293.96	4.14	-1.75	34.9
5294.55	3.64	-2.65	17.3
5295.31	4.42	-1.60	30.5
5321.11	4.44	-1.30	46.9
5322.04	2.28	-3.00	63.3
5373.71	4.47	-0.84	67.8

Table 4.1 (cont'd)

Wavelength (Angstroms)	Excitation Potential (eV)	Oscillator Strength (log gf)	Solar Equivalent Width (mÅ)
5376.83	4.29	-2.05	20.3
5379.57	3.70	-1.55	65.1
5386.33	4.15	-1.80	33.0
5395.22	4.45	-1.80	21.7
5398.28	4.45	-0.71	78.6
5401.27	4.32	-1.75	27.5
5409.13	4.37	-1.05	62.3
5417.03	4.42	-1.40	40.3
5432.95	4.45	-0.75	79.1
5436.30	4.39	-1.35	42.5
5441.34	4.31	-1.55	36.4
5461.55	4.45	-1.60	28.5
5464.28	4.14	-1.60	40.4
5466.99	3.57	-2.20	37.7
5472.71	4.21	-1.50	47.7
5473.16	4.19	-2.00	24.1
5491.83	4.19	-2.25	13.9
5497.52	1.01	-2.90	138.2
5501.47	0.96	-3.10	129.2
5522.45	4.21	-1.45	48.5
5539.28	3.64	-2.55	21.6
5543.94	4.22	-1.00	68.1
5546.51	4.37	-1.10	57.6
5549.95	3.70	-2.86	12.4
5552.69	4.96	-1.80	8.1
5560.21	4.44	-1.15	54.3
5618.63	4.21	-1.28	53.6
5619.60	4.39	-1.45	39.0
5633.95	4.99	-0.20	77.2
5635.82	4.26	-1.60	37.6
5636.70	3.64	-2.56	21.9
5638.26	4.22	-0.80	83.6
5641.43	4.26	-1.00	72.3
5652.32	4.26	-1.75	30.7
5653.87	4.39	-1.35	45.3
5667.52	4.18	-1.30	59.8
5679.02	4.65	-0.80	61.3
5680.24	4.19	-2.40	11.9
5705.46	4.30	-1.45	41.7
5731.76	4.26	-1.10	62.8
5741.85	4.26	-1.67	34.5
5775.08	4.22	-1.10	62.3
5778.45	2.59	-3.55	22.4
5793.91	4.22	-1.66	38.7
5806.73	4.61	-0.90	58.4
5809.22	3.88	-1.65	54.7
5814.81	4.28	-1.85	24.8

Table 4.1 (cont'd)

Wavelength (Angstroms)	Excitation Potential (eV)	Oscillator Strength (log gf)	Solar Equivalent Width (mÅ)
5852.22	4.55	-1.20	43.9
5855.08	4.61	-1.55	24.8
5856.09	4.29	-1.60	36.2
6027.05	4.08	-1.20	67.3
6065.48	2.61	-1.65	130.5
6079.01	4.65	-1.00	51.1
6082.71	2.22	-3.57	37.9
6085.26	2.76	-2.90	44.8
6120.25	0.92	-5.90	6.1
6127.91	4.14	-1.40	53.9
6151.62	2.18	-3.35	52.6
6157.73	4.08	-1.22	69.3
6165.36	4.14	-1.47	48.4
6173.34	2.22	-2.88	75.3
6180.20	2.73	-2.55	67.7
6187.99	3.94	-1.67	51.3
6213.43	2.22	-2.65	87.7
6219.28	2.20	-2.50	98.7
6229.23	2.85	-2.90	42.3
6232.64	3.65	-1.15	93.5
6240.65	2.22	-3.30	52.1
6252.56	2.40	-1.80	129.6
6265.13	2.18	-2.60	92.4
6270.23	2.86	-2.61	57.8
6380.74	4.19	-1.30	56.8
6667.71	4.58	-2.00	10.5
6699.14	4.59	-2.10	9.2
6703.57	2.76	-3.06	39.6
6739.52	1.56	-4.95	12.7
6750.15	2.42	-2.65	78.4
6752.71	4.64	-1.25	40.0
6786.86	4.19	-1.90	29.5
6793.26	4.08	-2.40	15.8
6837.01	4.59	-1.75	19.4
6839.83	2.56	-3.35	34.3
6842.69	4.64	-1.20	45.3
6843.66	4.55	-0.89	66.1
6858.15	4.61	-1.00	54.5

Table 4.2. List of Fe II lines

Wavelength (Angstroms)	Excitation Potential (eV)	Oscillator Strength (log *gf*)	Solar Equivalent Width (mÅ)
4508.29	2.86	-2.55	97.8
4576.34	2.84	-3.10	64.2
4582.84	2.84	-3.06	64.2
4993.36	2.81	-3.75	39.5
5197.58	3.23	-2.30	88.3
5234.63	3.22	-2.25	91.6
5264.81	3.23	-3.15	49.8
5414.07	3.22	-3.50	33.7
5425.26	3.20	-3.30	44.6
5534.85	3.25	-2.86	62.4
5725.96	3.42	-4.70	2.9
6084.11	3.20	-3.80	21.5
6113.32	3.22	-4.15	13.1
6149.24	3.89	-2.75	39.2
6247.56	3.89	-2.35	58.4
6416.91	3.89	-2.70	42.6
7479.69	3.89	-3.70	10.8
7515.83	3.90	-3.45	14.7

Table 4.3. List of Ti I lines

Wavelength (Angstroms)	Excitation Potential (eV)	Oscillator Strength (log gf)	Solar Equivalent Width (mÅ)
4512.73	0.84	-0.40	81.0
4518.02	0.83	-0.25	80.6
4534.78	0.84	0.35	106.1
4548.76	0.83	-0.28	81.9
4555.48	0.85	-0.40	71.1
4617.27	1.75	0.44	69.2
4778.26	2.24	-0.35	16.2
4820.41	1.50	-0.38	44.1
4913.61	1.87	0.22	54.9
4915.23	1.89	-0.91	8.6
4926.15	0.82	-2.09	7.5
4981.73	0.85	0.57	126.0
4999.50	0.83	0.32	114.5
5016.16	0.85	-0.48	71.8
5022.87	0.83	-0.33	80.0
5024.84	0.82	-0.53	76.6
5039.96	0.02	-1.08	90.0
5043.58	0.84	-1.59	21.8
5062.10	2.16	-0.39	18.9
5113.44	1.44	-0.70	28.8
5145.46	1.46	-0.54	41.0
5147.48	0.00	-1.94	47.7
5189.58	2.24	-1.19	2.6
5192.97	0.02	-0.95	88.5
5210.38	0.05	-0.82	99.0
5219.70	0.02	-2.22	28.8
5230.97	2.24	-1.19	2.5
5295.78	1.07	-1.59	13.4
5449.15	1.44	-1.87	3.4
5453.64	1.44	-1.60	5.7
5471.19	1.44	-1.42	8.4
5490.15	1.46	-0.84	23.7
5823.69	2.27	-1.01	5.0
5866.45	1.07	-0.79	51.8
5922.11	1.05	-1.38	24.1
5937.81	1.07	-1.94	9.4
5999.66	2.24	-0.72	11.4
6146.21	1.87	-1.48	3.4
6258.10	1.44	-0.39	53.5
6261.10	1.43	-0.53	54.4
6303.76	1.44	-1.58	8.4
6336.10	1.44	-1.69	8.2
6745.54	2.24	-1.23	3.3
7138.91	1.44	-1.61	6.9
7357.73	1.44	-1.02	27.3
7496.10	2.24	-1.06	5.2

Table 4.4. List of Ti II lines

Wavelength (Angstroms)	Excitation Potential (eV)	Oscillator Strength (log *gf*)	Solar Equivalent Width (mÅ)
4443.80	1.08	-0.71	153.2
4583.41	1.17	-2.84	33.8
4609.27	1.18	-3.32	14.4
4874.01	3.10	-0.86	44.3
5005.17	1.57	-2.73	27.6
5336.79	1.58	-1.60	76.1
5396.25	1.58	-3.18	13.2
5418.77	1.58	-2.13	51.0

4.4 Equivalent Widths

Historically, equivalent width ("EW") measurements of individual absorption lines using widely available and traditionally used tools such as IRAF's *splot* task involve a great deal of manual effort and user judgment. The two primary issues affecting the accuracy and precision of EW measurements are continuum placement and line crowding/blending – the latter of which can impact the line wing fitting. Dealing with these when performing manual (e.g. "by eye") indiviudal line measurements introduces a certain amount of subjectiveness into the process – a possible problem that Waters & Hollek (2013) refer to as the "personal fitting equation". Ignoring this potential problem, however, the astronomical community is faced with a much simpler, ever-growing problem: our data-sets are growing to sizes unmanageable by traditional methods! The need for automated EW measurement tools has become urgent, indeed. In our experience, it is deceptively difficult to "tell" a computer how to accurately and precisely do what the human eye seems able to do with ease.

Our equivalent width measurements are performed using a new semi-automated Interactive Data Language (IDL) routine written exclusively for this purpose. We developed this using code originally written by I. Roederer (cf. Roederer et al. 2010, Brugamyer et al. 2011). That code offers a flexible GUI-based tool that steps through each line of an input line-list, displaying a user-specified region of an input spectrum around each absorption line of interest, and allows for easy adjustment of the window region, continuum placement, fitting function (Gaussian or Voigt), the number of pixels to include in the line fit, etc. The program output is a list of equivalent widths, along with the original input line data, ready for use with MOOG.

Our modifications and enhancements to this original code were motivated by a desire to automate – wherever possible – steps in the process described in Brugamyer et al. (2011) that were previously done “by hand”. For example, we now calculate, and correct for, any spectrum red/blue radial velocity shift automatically, by cross-correlating with a solar reference spectrum. We also now calculate line full-width-half-maximum (FWHM) in velocity (velocity) automatically, by utilizing a technique of auto-correlation with the target spectrum itself. The result/consequence is that we need feed nothing to the program, aside from a line-list and fully reduced, continuum-normalized spectrum.

4.4.1 Semi-Automation of EW Measurements

The most important, major modifications to our routine were based on a desire to automate, as much as possible, our EW measurements. We view this as necessary for two main pragmatic reasons. First, with the inclusion of what we call our “error standards” – stars for which we have multiple observations on both instruments used in our analysis (see Section 4.7) – we must analyze ∽1000 individual spectra. With ∽400 targeted absorption lines per spectrum, we must therefore make ∽400,000 individual EW measurements! Tackling such a task using traditional, manual “by eye” methods is simply unreasonable. Second, we’re aiming for a very high degree of internal precision – at the 0.05 dex level for our abundance determinations – and we therefore wish to eliminate as much of the subjective “human element” from the process as possible. By automating the process, we can more comfortably claim that all our stars were analyzed in a uniform manner.

After exploring and/or testing various existing routines for automated EW measurements, we settled on our own, unique method for performing these measurements. The primary problem we face is that our samples are comprised of relatively cool, high-pressure, metal-rich stars with correspondingly complicated, crowded spectra. So, we have developed a semi-automated procedure for our EW measurements. The key to our unique, particular method is the uniformity of our dataset – all spectra were acquired with only two instruments, and in only one setup on each of those instruments. This uniformity extends even to the position of the 2-D spectrum on the CCD – a given wavelength of light falls on the same position on each CCD, to within a few pixels (at worst). So, our solar type stellar spectra all “look” very similar.

Our approach involves a simple type of machine learning in which we first determine how we wish to fit each line in a given stellar type, and then have the program apply that fit “blindly” to similar stars. We manually measure the EW of each line in our lists in a given star, with the program keeping track of the number of pixels we chose to include in our fit (by eye), as well as the continuum placement (relative to the already IRAF-normalized level of 1). [See Figure 4.1] (Note that our manual adjustments to continuum level are generally less than few percent.) Thus, we develop what we call an “EW template” file, containing all the relevant line atomic data plus these two key fitting parameters. Using a slightly different version of the code, we then apply these manually derived templates automatically (i.e. without user input) to other stars with similar atmospheric parameters. If the derived parameters (explained later) wind up being sufficiently different, then we simply choose a more suitable template and repeat/re-do the automated measurements.

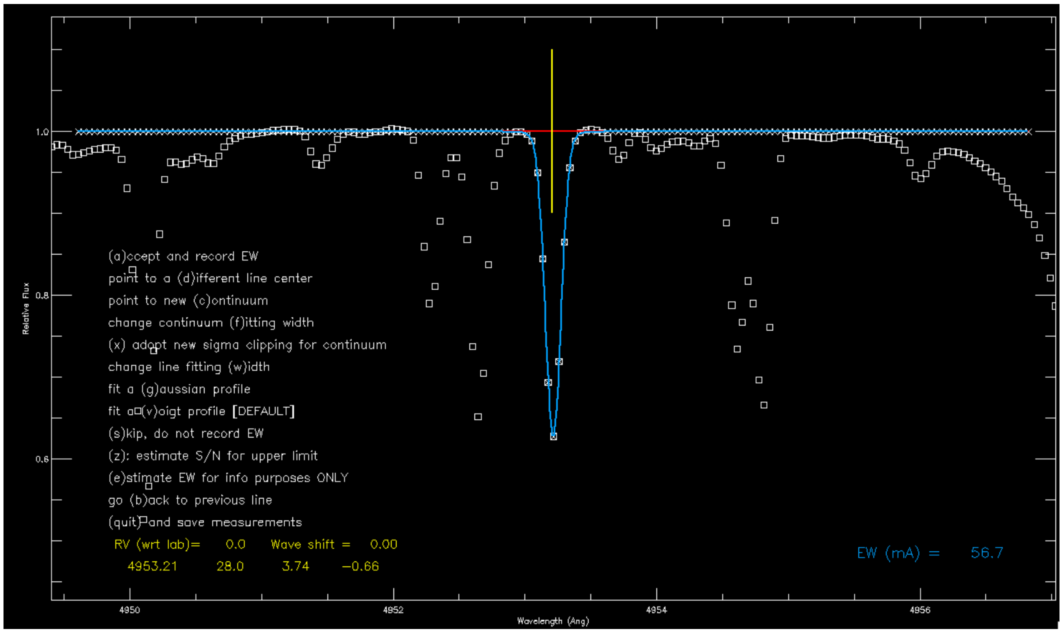

Figure 4.1 An example of our EW line fitting routine in action. The square boxes represent the actual data. The red horizontal line indicates our chosen continuum level, and the modelled line fit is evident in the blue fitted line.

The end result is a "semi-automated" measure of EWs in these stars. The final product from this step of our pipeline is a list of lines with relevant atomic data plus measured EW. It also includes automatically-written header information giving initial stellar parameter "guesses", ready to be fed to "automoog".

4.5 Stellar Parameters

We determine all stellar parameters and atomic abundances using a new Fortran routine "automoog" developed for this project. The program is based on codes originally written by C. Sneden for the analysis pipeline of the Chemical Abundances of Stars in the Halo (CASH) project (Hollek 2011, Roederer 2008), and utilizes the *abfind* driver via a "silent" mode call of the local thermodynamic equilibrium (LTE) line analysis and spectrum synthesis code MOOG[10] (Sneden 1973).

4.5.1 Model Atmospheres

Our model stellar atmospheres are constructed by interpolating within a grid of Kurucz (1993a) ATLAS9 models. We chose the ODFNEW (with new-and-improved opacity distribution functions, and no convective overshooting as described in Castelli, Grattton, and Kurucz 1997) set of models.

---

[10] available for download at http://www.as.utexas.edu/∽chris/moog.html

4.5.2 Parameter Constrainment

We feed the program a set of initial parameter "guesses"; although in our experience, from testing, the program's final output is fairly insensitive to initial starting point. Our initial effective temperatures are calculated from V-K colors (or B-V, in cases where V and K information is not available), following the calibrations of Ramirez & Melendez (2005). Our initial surface gravities are calculated from parallaxes (where available, which was almost all) following prescription of Afsar et al. (2012). (For example, although the method is well-known and discussed in the literature.) The necessary bolometric corrections were calculated frollowing the methods outlines in Masana, Jordi, and Ribas (2006). Our initial metallicities and microturbulent velocity guesses are defaulted to "solar" values.

We employ a traditional, curve of growth (COG) method (as described in Section **??**) in which:

- Effective temperature is constrained by enforcing excitation equilibrium (i.e. by eliminating any trend of derived abundance with line excitation potential).
- Surface gravity is constrained by enforcing ionization equilibriun (i.e. by forcing the abundances derived from neutral and ionic species to match).
- Microturbulent velocity is constrained by eliminating any trend in abundances with reduced equivalent width.

- Once these conditions are met, the final overall metallicity (e.g. average log epsilon for Fe) is calculated.

For these processes, we use a weighted average of Fe (2x) and Ti (1x) lines, which corresponds (roughly) to the relative number of lines in our chosen lists. The primary motivation for the inclusion of Ti lines in this constrainment process was to expand the number of low EP, small EW, and ionized lines used in the analysis, in order to more uniformly cover these parameter spaces. Doing so increases the precision of our derived parameters, by beating down the sigmas of the least-squares fits to the trends. We note that all Ti line data is laboratory-based (Lawler et al. 2013 for Ti I ; and Wood et al. 2013 for Ti II). (Recall that Fe line data is a hybrid mix of lab data, for which oscillator strengths were occasionally adjusted by "small" amounts to give"solar" abundances.) We argue that this grounding in pure lab values for Ti helps alleviate some of the problems associated with solar log gfs when these values are used to analyze stars with sufficiently different atmospheric parameters.

The process is fully automated - no user interaction is needed. Beginning with the initial parameter guesses, the code iteratively calls new model atmospheres, computes abundances and slopes of trends (or offsets between ion and neutral abundances), and determines which way to nudge the parameters until the conditions explained above are met.

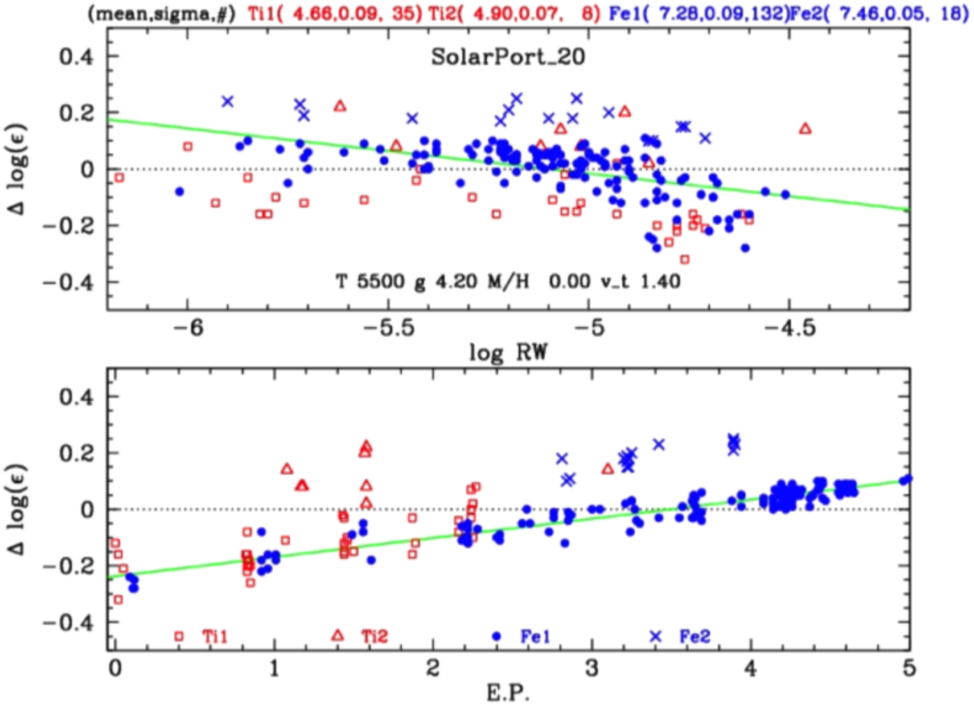

Figure 4.2 An example of our "Automoog" model atmosphere constrainment in action. This example shows what we don't want – trends in derived abundances with effective temperature and reduced equivalent width. Also, the abundances derived using neutrals and ions do not match. In this case, the temperature needs to be raised; the microturbulent velocity lowered; and the gravity raised.

4.6 Abundances

With the final model atmosphere in hand, MOOG calculates final atomic abundances. The final step in our pipeline is to calculate – on a line-by-line basis – differences between stellar and solar abundances. The final products are: (1) For each individual star, files containing:

- The average ″absolute″ (log epsilon) abundances, plus sigma, plus number of lines for a given species that went into calculation
- A list of Fe and Ti lines rejected/excluded (during sigma-clipping) from the final atmospheric parameter determinations

and (2) An entry for that particular star in a master ″database″ file that contains all stellar parameters and differential abundances (plus sigmas).

4.7 Tests

In this section, we describe some of the various tests of our pipeline that we've performed. As a first step, we wished to characterize the robustness of our stellar parameter determinations. Towards this end, we ran "automoog" with a grid of initial stellar parameter "guesses" on our solar spectrum. This grid was composed of "extreme" values, corresponding (roughly) to range of parameters in my samples: Teff: 4800 6400 K; log g: 3.5 4.7 dex; [Fe/H]: -0.50 to +0.50 dex; and ξ: 0.60 1.70 km/s. We thus permuted 16 combination of initial "guesses". With these, we allowed automoog to run to convergence. Results were as follows: Teff = 5805 +/-

22 K (absolute range = 63 K); log g = 4.49 +/- 0.05 dex (absolute range = 0.16 dex); [Fe/H] = 0.02 +/- 0.01 dex (absolute range = 0.03 dex); ξ = 1.19 +/- 0.01 km/s (absolute range = 0.03 km/s). These values are in good agreement with generally accepted canonical values. We therefore conclude from this test that our stellar parameter determinations are quite robust. That is, there seems to be very little sensitivity to initial "guesses".

In order to determine the "accuracy" of our automatically measured equivalent widths, we manually measured EWs of our full line-lists in our solar spectrum, producing a "template". Then, we automatically (blindly) applied this template to 20 different solar spectra, in order to characterize the scatter in our resulting EW values. Figure 4.3 summarizes these results. We note a tight scatter with a standard deviation of less than 2 milliAngstroms.

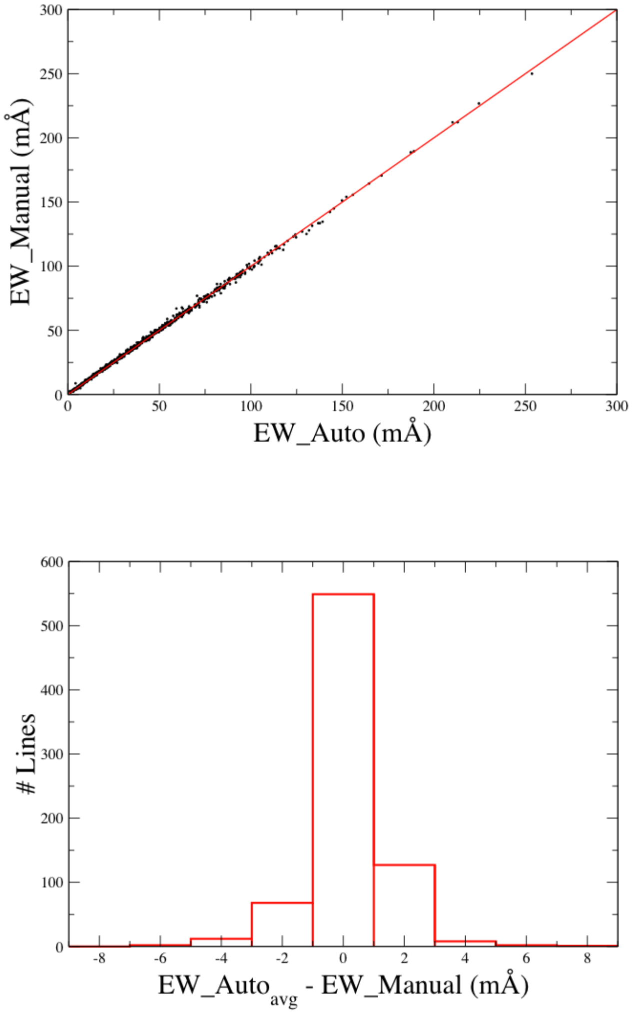

Figure 4.3 Plots demonstrating the accuracy of our automated measured equivalent widths. These are based on two manual EW templates applied blindly to 42 separate observations of those two stars. The top panel shows a scatter plot of our manually measured EWs, as a function of the automated measured EWs. Note the excellent agreement. The bottom panel shows a histogram of the difference. Note the very small average difference – the automated measurements are almost always within 3 milliangstroms of our manually measured values.

As a check on the internal precision of our methods, as well as a check on any possible offsets in derived atmospheric parameters or abundances between the two instruments used in our analysis, we obtained multiple exposures of four stars spanning a range of parameters on both instruments ($\backsim$20 spectra each 2 instruments). See Figures 4.4, 4.5 and 4.6

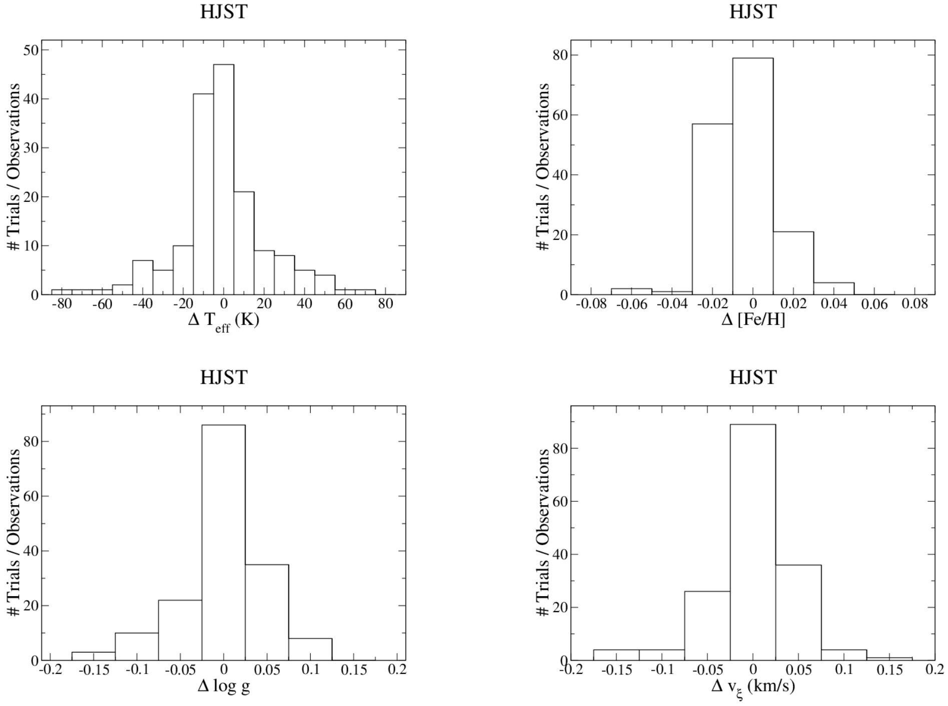

Figure 4.4 Histograms demonstrating the scatter in derived atmospheric parameters for the 2.7m Harlan J. Smith Telescope. These are based on 163 observations of eight stars; folded into single plots.

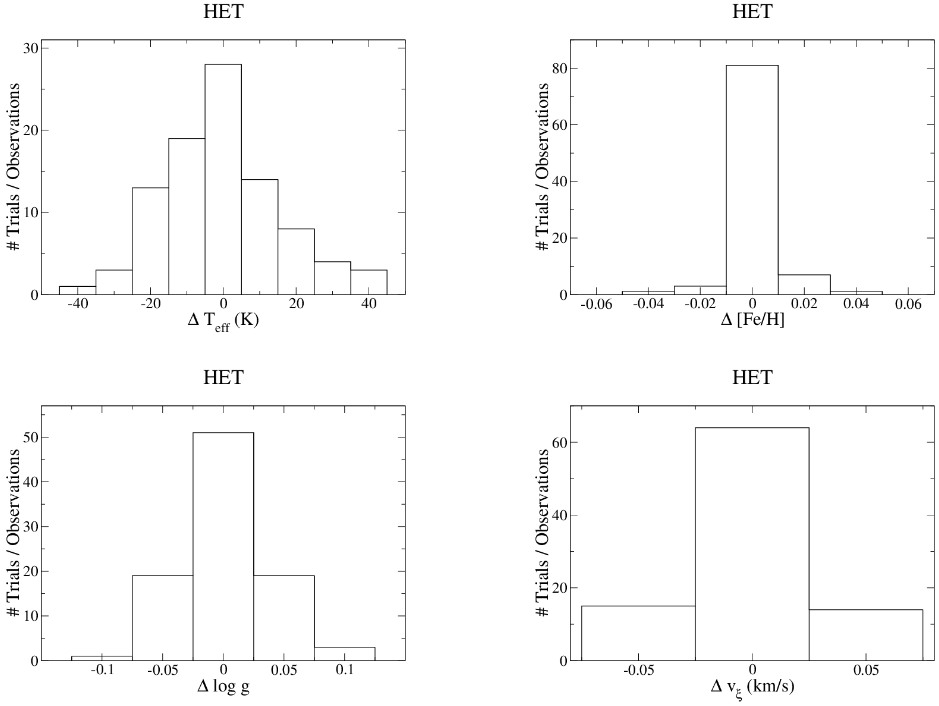

Figure 4.5 Histograms demonstrating the scatter in derived atmospheric parameters for the Hobby-Eberly Telescope. These are based on 94 observations of four stars; folded into single plots.

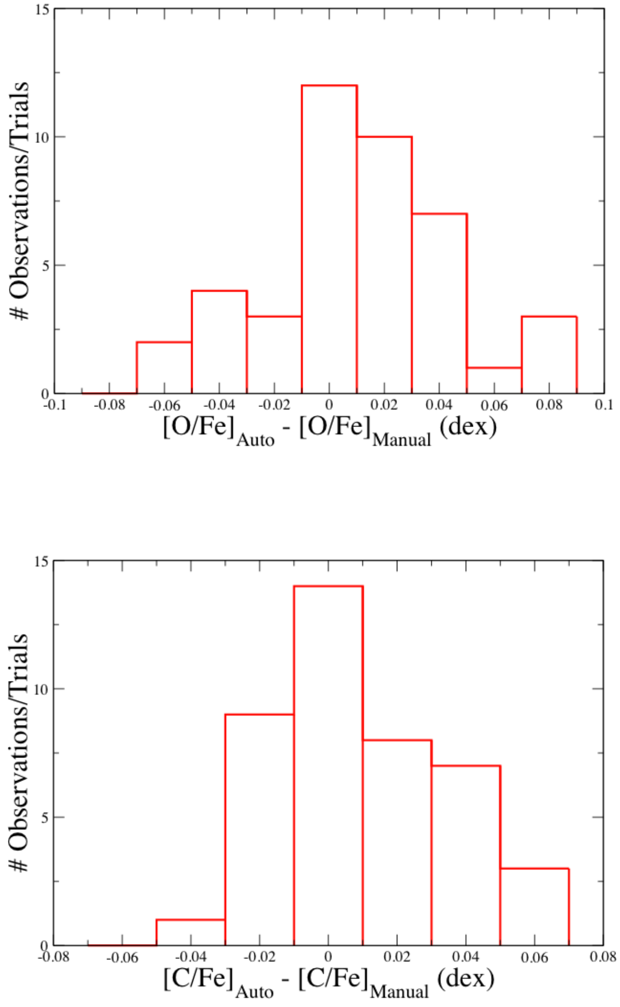

Figure 4.6 Histograms showing the difference between our manually measured oxygen (top panel) and carbon (bottom panel) abundances. These are based on 42 separate observations of two stars.

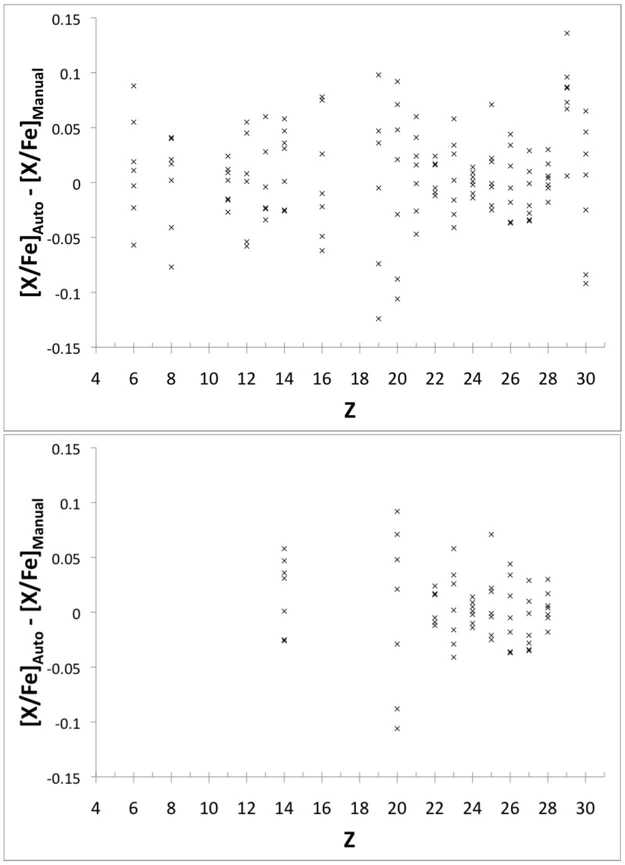

Figure 4.7 Plots showing the scatter in derived abundances for all measured species (top panel) and only those species with more than six measured lines (bottom panel). These are based on seven cases of EW templates applied blindly to other stars of similar type.

Chapter 5

Conclusion

Before the 2009 launch of the Kepler space telescope, the vast majority of the 350 then-known exoplanets had been discovered via radial velocity (RV) searches, meaning almost all were short-period, gas-giant planets. But over the past few years, Kepler has delivered more than 4,500 likely planet candidates to the astronomical community. More than 3,000 of these are thought to have a radius of less than 4 $R_\oplus$, and almost 1,700 of them have estimated radii of less than 2 $R_\oplus$! While valiant efforts have been made to determine the overall general stellar properties of these candidates (Batalha et al. 2013; Buchhave et al. 2012), little is known about their detailed chemical abundances. The time is ripe for exploration of individual elemental stellar abundance trends as a function of companion planet size.

A major issue encountered when modeling the physical processes responsible for giant planet formation is the relatively short disk lifetimes (no more than 10Myr) observed in nearby star-forming regions (Haisch et al. 2006) observations that are also supported by modeling (Alexander et al. 2006). The need for significant amounts of volatile ices, as well as the need for large accretion "feeding zones", dictates that the formation regions be at least several AU distant from the central star, where the disk midplane is cold; and where the gravitational spheres of influence ("Hill radii") of the forming planets are relatively large. On the other hand, the regions cannot be too far from the central star; else the lower solid surface densities (Pollack et al. 1996) and correspondingly longer dynamical timescales prevent sufficient accretion before the disk dissipates (Pollack et al. 1996; Dodson-Robinson & Bodenheimer 2010). So, the problem is really one of competing timescales, and we posit that it is this critical need for efficiency that underlies the Si trend we found in Brugamyer et al. (2011) (as discussed earlier in this work). In the race to reach the mass required to begin accreting hydrogen and helium, giant-planet formation may depend sensitively on the amount of refractory material available, inasmuch as this material provides sites for volatile condensation.

Smaller planets, on the other hand especially the terrestrial variety need not compete during their formation against short (gaseous) disk lifetimes. We therefore predict that host-star refractory abundances (for a given overall [Fe/H]) will demonstrate a positive correlation with companion planet size. In other words, we predict that no such correlations should exist for the smallest known planet candidates. (Unless "self-pollution" – accretion of rocky material after the stellar convection zone has more or less reached its final size – is in play, which would preferentially enrich the stellar photosphere in refractory material. This has been argued against by several authors, but only in regards to giant planets. Our existing line-lists, methods, and tools will enable determination of stellar photospheric abundance information for every element considered by Javoy et al. (2010) in their revised models of the bulk Earth composition (encompassing an estimated 99.8% of the Earths bulk mass). Thus, if chemical tracers of terrestrial planet formation are indeed to be found in host-star atmospheres, we are primed to find them.

The 3,500 Kepler Objects of Interest (KOIs) offer the only current target list for testing this prediction. Of the 530 planets discovered or confirmed via RV methods, none are less than 1 $M_{\oplus}$ (exoplanet.eu). Only 20 are less than 5 $M_{\oplus}$, which is the likely cutoff for terrestrial planets – once a planet reaches this mass, it is likely able to begin accreting gas from its surroundings (Dodson-Robinson & Bodenheimer 2010). And fewer than 50 are less than 10 $M_{\oplus}$ (the popular cutoff for so-called "Super Earth" classification). The KOI list, however, contains a wide range of densely sampled planet candidate sizes, down to 0.33 $M_{\oplus}$ (or roughly Mercury-size).

Unfortunately, these stars are also quite faint, with distances generally between 200-1000 pc, hindering the acquisition of the high resolution, high signal-to-noise (S/N) spectra necessary for accurate and precise analyses. The upgraded Hobby-Eberly Telescope (HET) – in combination with its new High Resolution Spectrograph (HRS) – will offer the perfect aperture plus instrument combination for this challenging task.

Appendix

Appendix 1

Contributing Author Publications

Following is a listing of publications to which I contributed. Included here are the titles, author list and abstracts of these various projects that I was a part of.

1.1 The architecture of the hierarchical triple star KOI 928 from eclipse timing variations seen in Kepler photometry

1.1.1 Author List

Steffen, J. H.; Quinn, S. N.; Borucki, W. J.; Brugamyer, E.; Bryson, S. T.; Buchhave, L. A.; Cochran, W. D.; Endl, M.; Fabrycky, D. C.; Ford, E. B.; Holman, M. J.; Jenkins, J.; Koch, D.; Latham, D. W.; MacQueen, P.; Mullally, F.; Prsa, A.; Ragozzine, D.; Rowe, J. F.; Sanderfer, D. T.; Seader, S. E.; Short, D.; Shporer, A.; Thompson, S. E.; Torres, G.; Twicken, J. D.; Welsh, W. F.; Windmiller, G.

1.1.2 Abstract

We present a hierarchical triple star system (KIC 9140402) where a low-mass eclipsing binary orbits a more massive third star. The orbital

period of the binary (4.988 29 d) is determined by the eclipse times seen in photometry from NASA's Kepler spacecraft. The periodically changing tidal field, due to the eccentric orbit of the binary about the tertiary, causes a change in the orbital period of the binary. The resulting eclipse timing variations provide insight into the dynamics and architecture of this system and allow the inference of the total mass of the binary (0.424 ± 0.017 $M_\odot$) and the orbital parameters of the binary about the central star.

1.2 KOI-54: The Kepler Discovery of Tidally Excited Pulsations and Brightenings in a Highly Eccentric Binary

1.2.1 Author List

Welsh, William F.; Orosz, Jerome A.; Aerts, Conny; Brown, Timothy M.; Brugamyer, Erik; Cochran, William D.; Gilliland, Ronald L.; Guzik, Joyce Ann; Kurtz, D. W.; Latham, David W.; Marcy, Geoffrey W.; Quinn, Samuel N.; Zima, Wolfgang; Allen, Christopher; Batalha, Natalie M.; Bryson, Steve; Buchhave, Lars A.; Caldwell, Douglas A.; Gautier, Thomas N., III; Howell, Steve B.; Kinemuchi, K.; Ibrahim, Khadeejah A.; Isaacson, Howard; Jenkins, Jon M.; Prsa, Andrej; Still, Martin; Street, Rachel; Wohler, Bill; Koch, David G.; Borucki, William J.

1.2.2 Abstract

Kepler observations of the star HD 187091 (KIC 8112039, hereafter KOI-54) revealed a remarkable light curve exhibiting sharp periodic brightening events every 41.8 days with a superimposed set of oscillations forming a beating pattern in phase with the brightenings. Spectroscopic observations revealed that this is a binary star with a highly eccentric orbit, e = 0.83. We are able to match the Kepler light curve and radial velocities with a nearly face-on (i = 5.5 degree) binary star model in which the brightening events are caused by tidal distortion and irradiation of nearly identical A stars during their close periastron passage. The two dominant oscillations in the light curve, responsible for the beating pattern, have frequencies that are the 91st and 90th harmonic of the orbital frequency. The power spectrum of the light curve, after removing the binary star brightening component, reveals a large number of pulsations, 30 of which have a signal-to-noise ratio of approximately 7. Nearly all of these pulsations have frequencies that are either integer multiples of the orbital frequency or are tidally split multiples of the orbital frequency. This pattern of frequencies unambiguously establishes the pulsations as resonances between the dynamic tides at periastron and the free oscillation modes of one or both of the stars. KOI-54 is only the fourth star to show such a phenomenon and is by far the richest in terms of excited modes.

1.3 Kepler-18b, c, and d: A System of Three Planets Confirmed by Transit Timing Variations, Light Curve Validation, Warm-Spitzer Photometry, and Radial Velocity Measurements

1.3.1 Author List

Cochran, William D.; Fabrycky, Daniel C.; Torres, Guillermo; Fressin, Francois; Desert, Jean-Michel; Ragozzine, Darin; Sasselov, Dimitar; Fortney, Jonathan J.; Rowe, Jason F.; Brugamyer, Erik J.; Bryson, Stephen T.; Carter, Joshua A.; Ciardi, David R.; Howell, Steve B.; Steffen, Jason H.; Borucki, William. J.; Koch, David G.; Winn, Joshua N.; Welsh, William F.; Uddin, Kamal; Tenenbaum, Peter; Still, M.; Seager, Sara; Quinn, Samuel N.; Mullally, F.; Miller, Neil; Marcy, Geoffrey W.; MacQueen, Phillip J.; Lucas, Phillip; Lissauer, Jack J.; Latham, David W.; Knutson, Heather; Kinemuchi, K.; Johnson, John A.; Jenkins, Jon M.; Isaacson, Howard; Howard, Andrew; Horch, Elliott; Holman, Matthew J.; Henze, Christopher E.; Haas, Michael R.; Gilliland, Ronald L.; Gautier, Thomas N., III; Ford, Eric B.; Fischer, Debra A.; Everett, Mark; Endl, Michael; Demory, Brice-Oliver; Deming, Drake; Charbonneau, David; Caldwell, Douglas; Buchhave, Lars; Brown, Timothy M.; Batalha, Natalie

1.3.2 Abstract

We report the detection of three transiting planets around a Sun-like star, which we designate Kepler-18. The transit signals were detected in photometric data from the Kepler satellite, and were confirmed to arise

from planets using a combination of large transit-timing variations (TTVs), radial velocity variations, Warm-Spitzer observations, and statistical analysis of false-positive probabilities. The Kepler-18 star has a mass of 0.97 M sun, a radius of 1.1 R sun, an effective temperature of 5345 K, and an iron abundance of [Fe/H] = +0.19. The planets have orbital periods of approximately 3.5, 7.6, and 14.9 days. The innermost planet "b" is a "super-Earth" with a mass of 6.9 ± 3.4 M Earth, a radius of 2.00 ± 0.10 R Earth, and a mean density of 4.9 ± 2.4 g cm3. The two outer planets "c" and "d" are both low-density Neptune-mass planets. Kepler-18c has a mass of 17.3 ± 1.9 M Earth, a radius of 5.49 ± 0.26 R Earth, and a mean density of 0.59 ± 0.07 g cm3, while Kepler-18d has a mass of 16.4 ± 1.4 M Earth, a radius of 6.98 ± 0.33 R Earth and a mean density of 0.27 ± 0.03 g cm3. Kepler-18c and Kepler-18d have orbital periods near a 2:1 mean-motion resonance, leading to large and readily detected TTVs.

1.4 Kepler-15b: A Hot Jupiter Enriched in Heavy Elements and the First Kepler Mission Planet Confirmed with the Hobby-Eberly Telescope

1.4.1 Author List

Endl, Michael; MacQueen, Phillip J.; Cochran, William D.; Brugamyer, Erik J.; Buchhave, Lars A.; Rowe, Jason; Lucas, Phillip; Isaacson, Howard; Bryson, Steve; Howell, Steve B.; Fortney, Jonathan J.; Hansen, Terese; Borucki, William J.; Caldwell, Douglas; Christiansen, Jessie L.; Ciardi, David R.; De-

mory, Brice-Olivier; Everett, Mark; Ford, Eric B.; Haas, Michael R.; Holman, Matthew J.; Horch, Elliott; Jenkins, Jon M.; Koch, David J.; Lissauer, Jack J.; Machalek, Pavel; Still, Martin; Welsh, William F.; Sanderfer, Dwight T.; Seader, Shawn E.; Smith, Jeffrey C.; Thompson, Susan E.; Twicken, Joseph D.

1.4.2 Abstract

We report the discovery of Kepler-15b (KOI-128), a new transiting exoplanet detected by NASA's Kepler mission. The transit signal with a period of 4.94 days was detected in the quarter 1 (Q1) Kepler photometry. For the first time, we have used the High Resolution Spectrograph (HRS) at the Hobby-Eberly Telescope (HET) to determine the mass of a Kepler planet via precise radial velocity (RV) measurements. The 24 HET/HRS RVs and 6 additional measurements from the Fibre-fed chelle Spectrograph spectrograph at the Nordic Optical Telescope reveal a Doppler signal with the same period and phase as the transit ephemeris. We used one HET/HRS spectrum of Kepler-15 taken without the iodine cell to determine accurate stellar parameters. The host star is a metal-rich ([Fe/H] = 0.36 ± 0.07) G-type main-sequence star with Teff = 5515 ± 124 K. The semi-amplitude K of the RV orbit is 78.7 ± 9 m s-1, which yields a planet mass of 0.66 ± 0.1 M Jup. The planet has a radius of 0.96 ± 0.06 R Jup and a mean bulk density of 0.9 ± 0.2 g cm-3. The radius of Kepler-15b is smaller than the majority of transiting planets with similar mass and irradiation level. This suggests that

the planet is more enriched in heavy elements than most other transiting giant planets. For Kepler-15b we estimate a heavy element mass of 30-40 $M_\oplus$.

1.5 Transiting circumbinary planets Kepler-34 b and Kepler-35 b

1.5.1 Author List

Welsh, William F.; Orosz, Jerome A.; Carter, Joshua A.; Fabrycky, Daniel C.; Ford, Eric B.; Lissauer, Jack J.; Prsa, Andrej; Quinn, Samuel N.; Ragozzine, Darin; Short, Donald R.; Torres, Guillermo; Winn, Joshua N.; Doyle, Laurance R.; Barclay, Thomas; Batalha, Natalie; Bloemen, Steven; Brugamyer, Erik; Buchhave, Lars A.; Caldwell, Caroline; Caldwell, Douglas A.; Christiansen, Jessie L.; Ciardi, David R.; Cochran, William D.; Endl, Michael; Fortney, Jonathan J.; Gautier, Thomas N., III; Gilliland, Ronald L.; Haas, Michael R.; Hall, Jennifer R.; Holman, Matthew J.; Howard, Andrew W.; Howell, Steve B.; Isaacson, Howard; Jenkins, Jon M.; Klaus, Todd C.; Latham, David W.; Li, Jie; Marcy, Geoffrey W.; Mazeh, Tsevi; Quintana, Elisa V.; Robertson, Paul; Shporer, Avi; Steffen, Jason H.; Windmiller, Gur; Koch, David G.; Borucki, William J.

1.5.2 Abstract

Most Sun-like stars in the Galaxy reside in gravitationally bound pairs of stars (binaries). Although long anticipated, the existence of a “cir-

cumbinary planet" orbiting such a pair of normal stars was not definitively established until the discovery of the planet transiting (that is, passing in front of) Kepler-16. Questions remained, however, about the prevalence of circumbinary planets and their range of orbital and physical properties. Here we report two additional transiting circumbinary planets: Kepler-34 (AB)b and Kepler-35 (AB)b, referred to here as Kepler-34 b and Kepler-35 b, respectively. Each is a low-density gas-giant planet on an orbit closely aligned with that of its parent stars. Kepler-34 b orbits two Sun-like stars every 289 days, whereas Kepler-35 b orbits a pair of smaller stars (89% and 81% of the Sun's mass) every 131 days. The planets experience large multi-periodic variations in incident stellar radiation arising from the orbital motion of the stars. The observed rate of circumbinary planets in our sample implies that more than 1% of close binary stars have giant planets in nearly coplanar orbits, yielding a Galactic population of at least several million.

1.6 The McDonald Observatory Planet Search: New Long-period Giant Planets and Two Interacting Jupiters in the HD 155358 System

1.6.1 Author List

Robertson, Paul; Endl, Michael; Cochran, William D.; MacQueen, Phillip J.; Wittenmyer, Robert A.; Horner, J.; Brugamyer, Erik J.; Simon, Attila E.; Barnes, Stuart I.; Caldwell, Caroline

1.6.2 Abstract

We present high-precision radial velocity (RV) observations of four solar-type (F7-G5) stars – HD 79498, HD 155358, HD 197037, and HD 220773 – taken as part of the McDonald Observatory Planet Search Program. For each of these stars, we see evidence of Keplerian motion caused by the presence of one or more gas giant planets in long-period orbits. We derive orbital parameters for each system and note the properties (composition, activity, etc.) of the host stars. While we have previously announced the two-gas-giant HD 155358 system, we now report a shorter period for planet c. This new period is consistent with the planets being trapped in mutual 2:1 mean-motion resonance. We therefore perform an in-depth stability analysis, placing additional constraints on the orbital parameters of the planets. These results demonstrate the excellent long-term RV stability of the spectrometers on both the Harlan J. Smith 2.7 m telescope and the Hobby-Eberly telescope.

1.7 An abundance of small exoplanets around stars with a wide range of metallicities

1.7.1 Author List

Buchhave, Lars A.; Latham, David W.; Johansen, Anders; Bizzarro, Martin; Torres, Guillermo; Rowe, Jason F.; Batalha, Natalie M.; Borucki, William J.; Brugamyer, Erik; Caldwell, Caroline; Bryson, Stephen T.; Ciardi, David R.; Cochran, William D.; Endl, Michael; Esquerdo, Gilbert A.;

Ford, Eric B.; Geary, John C.; Gilliland, Ronald L.; Hansen, Terese; Isaacson, Howard; Laird, John B.; Lucas, Philip W.; Marcy, Geoffrey W.; Morse, Jon A.; Robertson, Paul; Shporer, Avi; Stefanik, Robert P.; Still, Martin; Quinn, Samuel N.

1.7.2 Abstract

The abundance of heavy elements (metallicity) in the photospheres of stars similar to the Sun provides a "fossil" record of the chemical composition of the initial protoplanetary disk. Metal-rich stars are much more likely to harbour gas giant planets, supporting the model that planets form by accumulation of dust and ice particles. Recent ground-based surveys suggest that this correlation is weakened for Neptunian-sized planets. However, how the relationship between size and metallicity extends into the regime of terrestrial-sized exoplanets is unknown. Here we report spectroscopic metallicities of the host stars of 226 small exoplanet candidates discovered by NASA's Kepler mission, including objects that are comparable in size to the terrestrial planets in the Solar System. We find that planets with radii less than four Earth radii form around host stars with a wide range of metallicities (but on average a metallicity close to that of the Sun), whereas large planets preferentially form around stars with higher metallicities. This observation suggests that terrestrial planets may be widespread in the disk of the Galaxy, with no special requirement of enhanced metallicity for their formation.

1.8 A Second Giant Planet in 3:2 Mean-motion Resonance in the HD 204313 System

1.8.1 Author List

Robertson, Paul; Horner, J.; Wittenmyer, Robert A.; Endl, Michael; Cochran, William D.; MacQueen, Phillip J.; Brugamyer, Erik J.; Simon, Attila E.; Barnes, Stuart I.; Caldwell, Caroline

1.8.2 Abstract

We present eight years of high-precision radial velocity (RV) data for HD 204313 from the 2.7 m Harlan J. Smith Telescope at McDonald Observatory. The star is known to have a giant planet (Msin i = 3.5 MJ) on a ∽1900 day orbit, and a Neptune-mass planet at 0.2 AU. Using our own data in combination with the published CORALIE RVs of Segransan et al., we discover an outer Jovian (Msin i = 1.6 MJ) planet with P ∽ 2800 days. Our orbital fit suggests that the planets are in a 3:2 mean motion resonance, which would potentially affect their stability. We perform a detailed stability analysis and verify that the planets must be in resonance.

1.9 The Neptune-sized Circumbinary Planet Kepler-38b

1.9.1 Author List

Orosz, Jerome A.; Welsh, William F.; Carter, Joshua A.; Brugamyer, Erik; Buchhave, Lars A.; Cochran, William D.; Endl, Michael; Ford, Eric B.; MacQueen, Phillip; Short, Donald R.; Torres, Guillermo; Windmiller, Gur;

Agol, Eric; Barclay, Thomas; Caldwell, Douglas A.; Clarke, Bruce D.; Doyle, Laurance R.; Fabrycky, Daniel C.; Geary, John C.; Haghighipour, Nader; Holman, Matthew J.; Ibrahim, Khadeejah A.; Jenkins, Jon M.; Kinemuchi, Karen; Li, Jie; Lissauer, Jack J.; Pra, Andrej; Ragozzine, Darin; Shporer, Avi; Still, Martin; Wade, Richard A.

1.9.2 Abstract

We discuss the discovery and characterization of the circumbinary planet Kepler-38b. The stellar binary is single-lined, with a period of 18.8 days, and consists of a moderately evolved main-sequence star (MA = 0.949 ± 0.059 $M_\odot$ and RA = 1.757 ± 0.034 $R_\odot$) paired with a low-mass star (MB = 0.249 ± 0.010 $M_\odot$ and RB = 0.2724 ± 0.0053 $R_\odot$) in a mildly eccentric (e = 0.103) orbit. A total of eight transits due to a circumbinary planet crossing the primary star were identified in the Kepler light curve (using Kepler Quarters 1-11), from which a planetary period of 105.595 ± 0.053 days can be established. A photometric dynamical model fit to the radial velocity curve and Kepler light curve yields a planetary radius of 4.35 ± 0.11 $R_\oplus$, or equivalently 1.12 ± 0.03 R Nep. Since the planet is not sufficiently massive to observably alter the orbit of the binary from Keplerian motion, we can only place an upper limit on the mass of the planet of 122 $M_\oplus$ (7.11 M Nep or equivalently 0.384 M Jup) at 95% confidence. This upper limit should decrease as more Kepler data become available.

1.10 Revisiting rho1 Cancri e: A New Mass Determination of the Transiting Super-Earth

1.10.1 Author List

Endl, Michael; Robertson, Paul; Cochran, William D.; MacQueen, Phillip J.; Brugamyer, Erik J.; Caldwell, Caroline; Wittenmyer, Robert A.; Barnes, Stuart I.; Gullikson, Kevin

1.10.2 Abstract

We present a mass determination for the transiting super-Earth rho1 Cancri e based on nearly 700 precise radial velocity (RV) measurements. This extensive RV data set consists of data collected by the McDonald Observatory planet search and published data from Lick and Keck observatories. We obtained 212 RV measurements with the Tull Coud Spectrograph at the Harlan J. Smith 2.7 m Telescope and combined them with a new Doppler reduction of the 131 spectra that we have taken in 2003-2004 with the High-Resolution Spectrograph (HRS) at the Hobby-Eberly Telescope for the original discovery of rho1 Cancri e. Using this large data set we obtain a five-planet Keplerian orbital solution for the system and measure an RV semi-amplitude of K = 6.29 0.21 m s-1 for rho1 Cnc e and determine a mass of 8.37 0.38 $M_{\oplus}$. The uncertainty in mass is thus less than 5%. This planet was previously found to transit its parent star, which allowed them to estimate its radius. Combined with the latest radius estimate from Gillon et al., we obtain a mean density of 4.50 0.20 g cm-3. The location of rho1 Cnc e in the

mass-radius diagram suggests that the planet contains a significant amount of volatiles, possibly a water-rich envelope surrounding a rocky core.

1.11 Kepler-62: A Five-Planet System with Planets of 1.4 and 1.6 Earth Radii in the Habitable Zone

1.11.1 Author List

Borucki, William J.; Agol, Eric; Fressin, Francois; Kaltenegger, Lisa; Rowe, Jason; Isaacson, Howard; Fischer, Debra; Batalha, Natalie; Lissauer, Jack J.; Marcy, Geoffrey W.; Fabrycky, Daniel; Dsert, Jean-Michel; Bryson, Stephen T.; Barclay, Thomas; Bastien, Fabienne; Boss, Alan; Brugamyer, Erik; Buchhave, Lars A.; Burke, Chris; Caldwell, Douglas A.; Carter, Josh; Charbonneau, David; Crepp, Justin R.; Christensen-Dalsgaard, Jrgen; Christiansen, Jessie L.; Ciardi, David; Cochran, William D.; DeVore, Edna; Doyle, Laurance; Dupree, Andrea K.; Endl, Michael; Everett, Mark E.; Ford, Eric B.; Fortney, Jonathan; Gautier, Thomas N.; Geary, John C.; Gould, Alan; Haas, Michael; Henze, Christopher; Howard, Andrew W.; Howell, Steve B.; Huber, Daniel; Jenkins, Jon M.; Kjeldsen, Hans; Kolbl, Rea; Kolodziejczak, Jeffery; Latham, David W.; Lee, Brian L.; Lopez, Eric; Mullally, Fergal; Orosz, Jerome A.; Prsa, Andrej; Quintana, Elisa V.; Sanchis-Ojeda, Roberto; Sasselov, Dimitar; Seader, Shawn; Shporer, Avi; Steffen, Jason H.; Still, Martin; Tenenbaum, Peter; Thompson, Susan E.; Torres, Guillermo; Twicken, Joseph D.; Welsh, William F.; Winn, Joshua N.

1.11.2 Abstract

We present the detection of five planets – Kepler-62b, c, d, e, and f – of size 1.31, 0.54, 1.95, 1.61 and 1.41 Earth radii ($R_\oplus$), orbiting a K2V star at periods of 5.7, 12.4, 18.2, 122.4, and 267.3 days, respectively. The outermost planets, Kepler-62e and -62f, are super-Earth-size (1.25 $R_\oplus$ ¡ planet radius 2.0 $R_\oplus$) planets in the habitable zone of their host star, respectively receiving 1.2 ± 0.2 times and 0.41 ± 0.05 times the solar flux at Earths orbit. Theoretical models of Kepler-62e and -62f for a stellar age of 7 billion years suggest that both planets could be solid, either with a rocky composition or composed of mostly solid water in their bulk.

1.12 Searching for solar-like oscillations in the delta Scuti star rho Puppis

1.12.1 Author List

Antoci, V.; Handler, G.; Grundahl, F.; Carrier, F.; Brugamyer, E. J.; Robertson, P.; Kjeldsen, H.; Kok, Y.; Ireland, M.; Matthews, J. M.

1.12.2 Abstract

Despite the shallow convective envelopes of delta Scuti pulsators, solar-like oscillations are theoretically predicted to be excited in those stars as well. To search for such stochastic oscillations, we organized a spectroscopic multisite campaign for the bright, metal-rich delta Scuti star rho Puppis. We obtained a total of 2763 high-resolution spectra using four tele-

scopes. We discuss the reduction and analysis with the iodine cell technique, developed for searching low-amplitude radial velocity variations, in the presence of high-amplitude variability. Furthermore, we have determined the angular diameter of rho Puppis to be 1.68 ± 0.03 mas, translating into a radius of 3.52 0.07 $R_\odot$. Using this value, the frequency of maximum power of possible solar-like oscillations is expected at 43 ± 2 c d-1 (498 ± 23 Hz). The dominant delta Scuti-type pulsation mode of rho Puppis is known to be the radial fundamental mode which allows us to determine the mean density of the star, and therefore an expected large frequency separation of 2.73 c d-1 (31.6 Hz). We conclude that (1) the radial velocity amplitudes of the delta Scuti pulsations are different for different spectral lines; (2) we can exclude solar-like oscillations to be present in rho Puppis with an amplitude per radial mode larger than 0.5 m s-1.

1.13 Masses, Radii, and Orbits of Small Kepler Planets: The Transition from Gaseous to Rocky Planets

1.13.1 Author List

Marcy, Geoffrey W.; Isaacson, Howard; Howard, Andrew W.; Rowe, Jason F.; Jenkins, Jon M.; Bryson, Stephen T.; Latham, David W.; Howell, Steve B.; Gautier, Thomas N., III; Batalha, Natalie M.; Rogers, Leslie; Ciardi, David; Fischer, Debra A.; Gilliland, Ronald L.; Kjeldsen, Hans; Christensen-Dalsgaard, Jrgen; Huber, Daniel; Chaplin, William J.; Basu, Sarbani; Buchhave, Lars A.; Quinn, Samuel N.; Borucki, William J.; Koch, David G.;

Hunter, Roger; Caldwell, Douglas A.; Van Cleve, Jeffrey; Kolbl, Rea; Weiss, Lauren M.; Petigura, Erik; Seager, Sara; Morton, Timothy; Johnson, John Asher; Ballard, Sarah; Burke, Chris; Cochran, William D.; Endl, Michael; MacQueen, Phillip; Everett, Mark E.; Lissauer, Jack J.; Ford, Eric B.; Torres, Guillermo; Fressin, Francois; Brown, Timothy M.; Steffen, Jason H.; Charbonneau, David; Basri, Gibor S.; Sasselov, Dimitar D.; Winn, Joshua; Sanchis-Ojeda, Roberto; Christiansen, Jessie; Adams, Elisabeth; Henze, Christopher; Dupree, Andrea; Fabrycky, Daniel C.; Fortney, Jonathan J.; Tarter, Jill; Holman, Matthew J.; Tenenbaum, Peter; Shporer, Avi; Lucas, Philip W.; Welsh, William F.; Orosz, Jerome A.; Bedding, T. R.; Campante, T. L.; Davies, G. R.; Elsworth, Y.; Handberg, R.; Hekker, S.; Karoff, C.; Kawaler, S. D.; Lund, M. N.; Lundkvist, M.; Metcalfe, T. S.; Miglio, A.; Silva Aguirre, V.; Stello, D.; White, T. R.; Boss, Alan; Devore, Edna; Gould, Alan; Prsa, Andrej; Agol, Eric; Barclay, Thomas; Coughlin, Jeff; Brugamyer, Erik; Mullally, Fergal; Quintana, Elisa V.; Still, Martin; Thompson, Susan E.; Morrison, David; Twicken, Joseph D.; Dsert, Jean-Michel; Carter, Josh; Crepp, Justin R.; Hbrard, Guillaume; Santerne, Alexandre; Moutou, Claire; Sobeck, Charlie; Hudgins, Douglas; Haas, Michael R.; Robertson, Paul; Lillo-Box, Jorge; Barrado, David

1.13.2 Abstract

We report on the masses, sizes, and orbits of the planets orbiting 22 Kepler stars. There are 49 planet candidates around these stars, including

42 detected through transits and 7 revealed by precise Doppler measurements of the host stars. Based on an analysis of the Kepler brightness measurements, along with high-resolution imaging and spectroscopy, Doppler spectroscopy, and (for 11 stars) asteroseismology, we establish low false-positive probabilities (FPPs) for all of the transiting planets (41 of 42 have an FPP under 1%), and we constrain their sizes and masses. Most of the transiting planets are smaller than three times the size of Earth. For 16 planets, the Doppler signal was securely detected, providing a direct measurement of the planet's mass. For the other 26 planets we provide either marginal mass measurements or upper limits to their masses and densities; in many cases we can rule out a rocky composition. We identify six planets with densities above 5 g cm-3, suggesting a mostly rocky interior for them. Indeed, the only planets that are compatible with a purely rocky composition are smaller than 2 $R_{\oplus}$. Larger planets evidently contain a larger fraction of low-density material (H, He, and H2O).

1.14 Kepler-424 b: A "Lonely" Hot Jupiter that Found a Companion

1.14.1 Author List

Endl, Michael; Caldwell, Douglas A.; Barclay, Thomas; Huber, Daniel; Isaacson, Howard; Buchhave, Lars A.; Brugamyer, Erik; Robertson, Paul; Cochran, William D.; MacQueen, Phillip J.; Havel, Mathieu; Lucas, Phillip; Howell, Steve B.; Fischer, Debra; Quintana, Elisa; Ciardi, David R.

1.14.2 Abstract

Hot Jupiter systems provide unique observational constraints for migration models in multiple systems and binaries. We report on the discovery of the Kepler-424 (KOI-214) two-planet system, which consists of a transiting hot Jupiter (Kepler-424b) in a 3.31 day orbit accompanied by a more massive outer companion in an eccentric (e = 0.3) 223 day orbit. The outer giant planet, Kepler-424c, is not detected transiting the host star. The masses of both planets and the orbital parameters for the second planet were determined using precise radial velocity (RV) measurements from the Hobby-Eberly Telescope (HET) and its High Resolution Spectrograph (HRS). In stark contrast to smaller planets, hot Jupiters are predominantly found to be lacking any nearby additional planets; they appear to be "lonely". This might be a consequence of these systems having a highly dynamical past. The Kepler-424 planetary system has a hot Jupiter in a multiple system, similar to upsilon Andromedae. We also present our results for Kepler-422 (KOI-22), Kepler-77 (KOI-127), Kepler-43 (KOI-135), and Kepler-423 (KOI-183). These results are based on spectroscopic data collected with the Nordic Optical Telescope (NOT), the Keck 1 telescope, and HET. For all systems, we rule out false positives based on various follow-up observations, confirming the planetary nature of these companions. We performed a comparison with planetary evolutionary models which indicate that these five hot Jupiters have heavy element contents between 20 and 120 $M_\oplus$.

Bibliography

[1] Asplund, M. 2005, ARA&A, 43, 481

[2] Asplund, M., Grevesse, N., Sauval, J., & Scott, P. 2009, ARA&A, 47, 481

[3] Bodaghee, A., Santos, N. C., Israelian, G. & Mayor, M. 2003, A&A, 404, 715

[Borucki et al. 2010] Borucki, W. J., Koch, D., Basri, G., et al. 2010, Science, 327, 977

[5] Casagrande, L., Ramírez, I., Meléndez, J., Bessell, M., & Asplund, M. 2010, A&A, 512, 54

[6] Chambers, J. E., Wetherill, G. W., & Boss, A. P. 1996, , 119, 261

[7] Chambers, J. E. 1999, MNRAS, 304, 793

[Cochran & Hatzes 1993] Cochran, W. D., & Hatzes, A. P. 1993, in ASP Conf. Ser. 36, Planets around Pulsars, ed. J. A. Phillips, J. E. Thorsett, & S. R. Kulkarni (San Fransisco, CA: ASP), 267

[9] Cochran, W. D., Hatzes, A. P., Butler, R. P., & Marcy, G. W. 1997, ApJ, 483, 457

[10] Dodson-Robinson, S. E. & Bodenheimer, P. 2010, Icarus, 207, 491

[11] Endl, M., Kürster, M., Els, S. 2000, A&A, 362, 585

[12] Fabbian, D., Asplund, M., Barklem, P. S., Carlsson, M., & Kiselman, D. 2009, A&A, 500, 1221

[13] Fabbian, D., Khomenko, E., Moreno-Insertis, F., & Nordlund, Å. 2010, ApJ, 724, 1536

[14] Fischer, D. A., & Valenti, J. 2005, ApJ, 622, 1102

[Fressin et al. 2013] Fressin, F., Torres, G., Charbonneau, D., et al. 2013, ApJ, 766, 81

[16] Fuhrmann, K., & Bernkopf, J. 2008, MNRAS, 384, 1563

[17] Grether, D., & Lineweaver, C. H. 2007, ApJ, 669, 1220

[18] Gonzalez, G. 1997, MNRAS, 285, 403

[19] Gonzalez, G. 1998, A&A, 334, 221

[20] Gonzalez, G. 1999, MNRAS, 308, 447

[21] González Hernández, J. I., Israelian, G., Santos, N. C., et al. 2010, ApJ, 720, 1592

[22] González Hernández, J. I., Delgado-Mena, E., Sousa, S. G., et al. 2013, A&A, 552, A6

[23] Hayashi, C. 1981, Supplement of the Progress of Theoretical Physics, No. 70, 35

[24] Henning, Th. & Salama, F. 1998, Science, 282, 2204

[25] Heiter, U., & Luck, R. E. 2003 AJ, 126, 2015

[26] Horner, J., & Jones, B. W. 2008, International Journal of Astrobiology, 7, 251

[27] Horner, J., & Jones, B. W. 2012, International Journal of Astrobiology, 11, 147

[28] Horner, J., Jones, B. W., & Chambers, J. 2010, International Journal of Astrobiology, 9, 1

[29] Horner, J., Wittenmyer, R. A., Hinse, T. C., & Tinney, C. G. 2012a, MNRAS, 425, 749

[30] Horner, J., Hinse, T. C., Wittenmyer, R. A., Marshall, J. P., & Tinney, C. G. 2012b, MNRAS, 427, 2812

[2010] Howard, A. W.; Johnson, J. A.; Marcy, G. W. et al. 2010, ApJ, 721, 1467

[Howard et al. 2012] Howard, A. W., Marcy, G. W., Bryson, S. T., et al. 2012, ApJS, 201, 15

[33] Kim, Y., Demarque, P., Yi, S. K., & Alexander, D. R. 2002, ApJS, 143, 499

[34] Kiselman, D. 1993, A&A, 275, 269

[35] Kiselman, D. 2001, New Astron. Rev., 45, 559

[36] Kurucz, R. 1993, ATLAS9 Stellar Atmosphere Programs and 2 km/s grid. Kurucz CD-ROM No. 13. (Cambridge: Smithsonian Astrophys. Obs.)

[37] Kurucz, R. 1993, Atomic data for opacity calculations. Kurucz CD-ROM No. 1. (Cambridge: Smithsonian Astrophys. Obs.)

[38] Lissauer, J. J. 1995, Icarus, 114, 217

[39] Lodders, K. 2003, ApJ, 591, 1220

[40] Lodders, K. 2004, ApJ, 611, 587

[41] Mayor, M., & Queloz, D. 1995, Nature, 378, 355

[Meschiari et al. 2009] Meschiari, S. Wolf, A. S., Rivera, E., Laughlin, G., Vogt, S., Butler, P. 2009, PASP, 121, 1016

[43] Meléndez, J., & Barbuy, B. 2009, A&A, 497, 611

[44] Meléndez, J., Asplund, M., Gustafsson, B., & Yong, D. 2009, ApJ, 704, L66

[45] Neves, V., Santos, N. C., Sousa, S. G., Correia, A. C. M., & Israelian, G. 2009, A&A, 497, 563

[46] O'Brian, T. R., Wickliffe, M. E., Lawler, J. E., Whaling, W., & Brault, J. W. 1991, J. Opt. Soc. Am., B8, 1185

[Petigura et al. 2013] Petigura, E. A., Howard, A. W., Marcy, G. W. 2013, PNAS, 110, 19273

[48] Pollack, J. B., Hubickyj, O., Bodenheimer, P., Lissauer, J. J., Podolak, M., & Greenzweig, Y. 1996, Icarus, 124, 62

[49] Reid, I. N. 2002, PASP, 114, 306

[50] Ramírez, I., Allende Prieto, C., & Lambert, D. L. 2007, A&A, 465, 271

[51] Ramírez, I., Meléndez, J., & Asplund, M. 2009, A&A, 508, L17

[52] Ramírez, I., Asplund, M., Baumann, P., Meléndez, J., & Bensby, T. 2010, A&A, 521, A33

[53] Ramírez, I., Meléndez, J., Cornejo, D., Roederer, I. U., & Fish, J. R. 2011, ApJ, 740, 76

[54] Ramírez, I., Allende Prieto, C., & Lambert, D. L. 2013, ApJ, 764, 78

[55] Ramírez, I., Meléndez, J., Bean, J., et al. 2014, in press

[Raymond 2006] Raymond, S. N. 2006, ApJ, 643, 131

[57] Robertson, P., Endl, M., Cochran, W. D., et al. 2012a, ApJ, 749, 39

[58] Robertson, P., Horner, J., Wittenmyer, R. A., et al. 2012b, ApJ, 754, 50

[59] Roederer, I. U., Sneden, C., Thompson, I. B., Preston, G. W., & Shectman, S. 2010, ApJ, 711, 573

[60] Robinson, S. E., Laughlin, G., Bodenheimer, P., & Fischer, D. 2006, ApJ, 643, 484

[61] Safronov, V. S. 1969, Evolution of the Protoplanetary Cloud and the Formation of the Earth and Planets. Nauka, Moscow. English translation: NASA TTF-667, 1972

[62] Santos, N. C., Israelian, G., Mayor, M., Bento, J. P., Almeida, P. C., Sousa, S. G., & Ecuvillon, A. 2005, A&A, 437, 1127

[63] Shi, J. R., Gehren, T., Butler, K., Mashonkina, L. I., & Zhao, G. 2008, A&A, 486, 303

[64] Schuler, S. C., Flateau, D., Cunha, K., et al. 2011, ApJ, 732, 55

[65] Sneden, C. A. 1973, Ph.D. thesis, Univ. of Texas at Austin

[66] Takeda, Y., & Honda, S. 2005, PASJ, 57, 65

[67] Timmes, F. X., Woosley, S. E., & Weaver, T. A. 1995, ApJS, 98, 617

[68] Tucci Maia, M., Meléndez, J., & Ramírez, I. 2014, ApJ, 790, L25

[69] Tull, R. G., MacQueen, P., Sneden, C., & Lambert, D. L. 1994, in ASP Conf. Ser. 55, Optical Astronomy from the Earth and Moon, ed. D. M. Pyper & R. J. Angione (San Fransisco: ASP), 148

[70] Tull, R. G. 1998, in Optical Astronomical Instrumentation, Proc. SPIE 3355, 387

[71] Wedemeyer, S. 2001, A&A, 373, 998

[72] Weidenschilling, S. J. 1977, Ap&SS, 51, 153

[73] Wittenmyer, R. A., Endl, M., Cochran, W. D., Hatzes, A. P., Walker, G. A. H., Yang, S. L. S., & Paulson, D. P. 2006, AJ, 132, 177

[74] Wittenmyer, R. A., Tinney, C. G., O'Toole, S. J., Jones, H. R. A., Butler, R. P., Carter, B. D., & Bailey, J. 2011a, ApJ, 727, 102

[Wittenmyer et al. 2011b] Wittenmyer, R. A., Tinney, C. G., Butler, R. P., et al. 2011b, ApJ, 738, 81

[76] Wittenmyer, R. A., Horner, J., Tuomi, M., et al. 2012a, ApJ, 753, 169

[77] Wittenmyer, R. A., Horner, J., & Tinney, C. G. 2012b, ApJ, 761, 165

[78] Wittenmyer, R. A., Horner, J., Tinney, C. G., et al. 2014a, ApJ, 783, 103

[79] Wittenmyer, R. A., Tan, X., Lee, M. H., et al. 2014b, ApJ, 780, 140

[80] Yi, S., Demarque, P., Kim, Y., et al. 2001, ApJS, 136, 417

[81] Zechmeister, M., Kürster, M., Endl, M., et al. 2013, A&A, 552, A78

[82] Zechmeister, M., Kürster, M. 2009, A&A, 496, 577

Vita

Erik Brugamyer was born in Sioux Falls, South Dakota and grew up in Amarillo, Texas. He received a B.S. degree in physics and a B.A. degree in astronomy from the University of Texas at Austin in 2000. As an undergraduate, he studied copper abundances in metal-poor stars with Chris Sneden. He received a Master in Professional Accounting degree in 2002, after which he spent two years working at a large public accounting firm. Erik joined the Astronomy Department at the University of Texas at Austin in 2008, and received a Master of Arts degree in astronomy in 2010.

When he's not staring at stellar spectra, Erik enjoys playing frisbee with his active Shetland sheepdog, playing disc golf at the many beautiful courses in and around Austin, playing pool, listening to music, and reading.

Permanent address: 4600 Monterey Oaks Blvd, Apt. 1116
Austin, TX 78749

This dissertation was typeset with LaTeX by the author.